SOFAR Signal Shaping; Influence of Topography and Relative Source Depth

By

Leon Krige

Submitted
towards the degree of
Doctor of Philosophy

UNIVERSITY OF CAPE TOWN
FEBRUARY 2000

Abstract

The shaping of SOFAR signals by topographic interference and the depth of the source relative to the axis of the sound channel is investigated. Eight shot signals from five different sites near Cape Town were received at three widely spaced hydrophones at Ascension over a number of 4.4 Megametre lines. These signals show the effects of (1) sources at different depths relative to the axis of the sound channel, (2) blocking and partial blocking of direct rays by seamounts and narrow undersea ridges and (3) a sound speed profile displaced downwards by a filament of warm surface water. Comparisons with ray trace and normal mode models show that some of the received signals consist of a combination of slower, refracted rays and faster rays reflected off Walvis ridge. The reflected energy starts earlier and has a greater amplitude than would be expected from ray trace modelling. This energy will act as noise and make ATOC (Acoustic Thermometry of Ocean Climate) determinations more difficult.

Acknowledgements

This thesis would not have been possible without the participation of various members of staff of IMT (Institute for Maritime Technology, Simon's Town), the Department of Oceanography, UCT (University of Cape Town), the South African Navy, and the USAF personnel at Ascension. In particular, Dr. Dave Palmer of NOAA (National Oceanic and Aeronautic Administration) first suggested the test, kept the idea alive in the face of difficulties, ensured that the reception and recording was done flawlessly and provided us with all the data he could.

I would like to thank my wife, Suzanne, for her patience and support and my supervisor, Prof. Geoff Brundrit, for his insight and help and for being one of the main participants in the experiment. Thanks also to Gary Bold in Auckland, Matt Dzieciuch in San Diego and Mark Grabb formerly at the University of Michigan for going out of their way to provide me with help and program code via e-mail.

Table of Contents

Page

List of Illustrations

Page

List of Tables

Page

Chapter 1. Introduction

1.1. Origins

In 1992, a group of scientists in South Africa, in collaboration with Dr. Dave Palmer of NOAA (National Oceanic and Aeronautic Administration) in the USA and with the assistance of the South African Navy, attempted to characterise the deep-water transmission paths between Cape Town and Ascension Island. Eight explosive sound sources were detonated near Cape Town. Each of these shots was recorded at five of the bottom-mounted U. S. Air Force Missile Impact Locating System hydrophones at Ascension.

This thesis has its origin at the time when a group of us first looked at the forty arrival waveforms recorded at Ascension Island. We were expecting to see forty nearly identical recordings or, at most, a simple pattern of "good" and "bad" shots where some shots or possibly even some hydrophones showed a reduction in amplitude due to blocking. Instead of a simple pattern, we saw complex and baffling changes in amplitude and shape (Figure 1-1). This thesis details the unravelling of the causes of those variations that at first appeared so strange.

1.2. Sound in the sea and SOFAR

Man has known of sound in the sea for centuries, but it is only in the twentieth century that sound in the sea has been intensively studied, quantified, and put to use. One of the more surprising discoveries was that of a deep sound channel that conducted low frequency sound over very long distances. Sound from small explosive sources detonated in the sound channel could be received thousands of kilometres away. An application of this novel phenomenon was found in the SOFAR (Sound Fixing And Ranging) system, where the crew of an aircraft forced down at sea, dropped a small explosive charge that detonated at approximately the optimum depth in the sound channel. The observed time of arrival of the sound of the charge at three or more receivers "fixed" the position of the explosion. The remarkably long propagation ranges in the sound channel is due to reduced spreading losses caused by repeated refraction of diverging sound rays back towards the centre of the channel.

1. Introduction

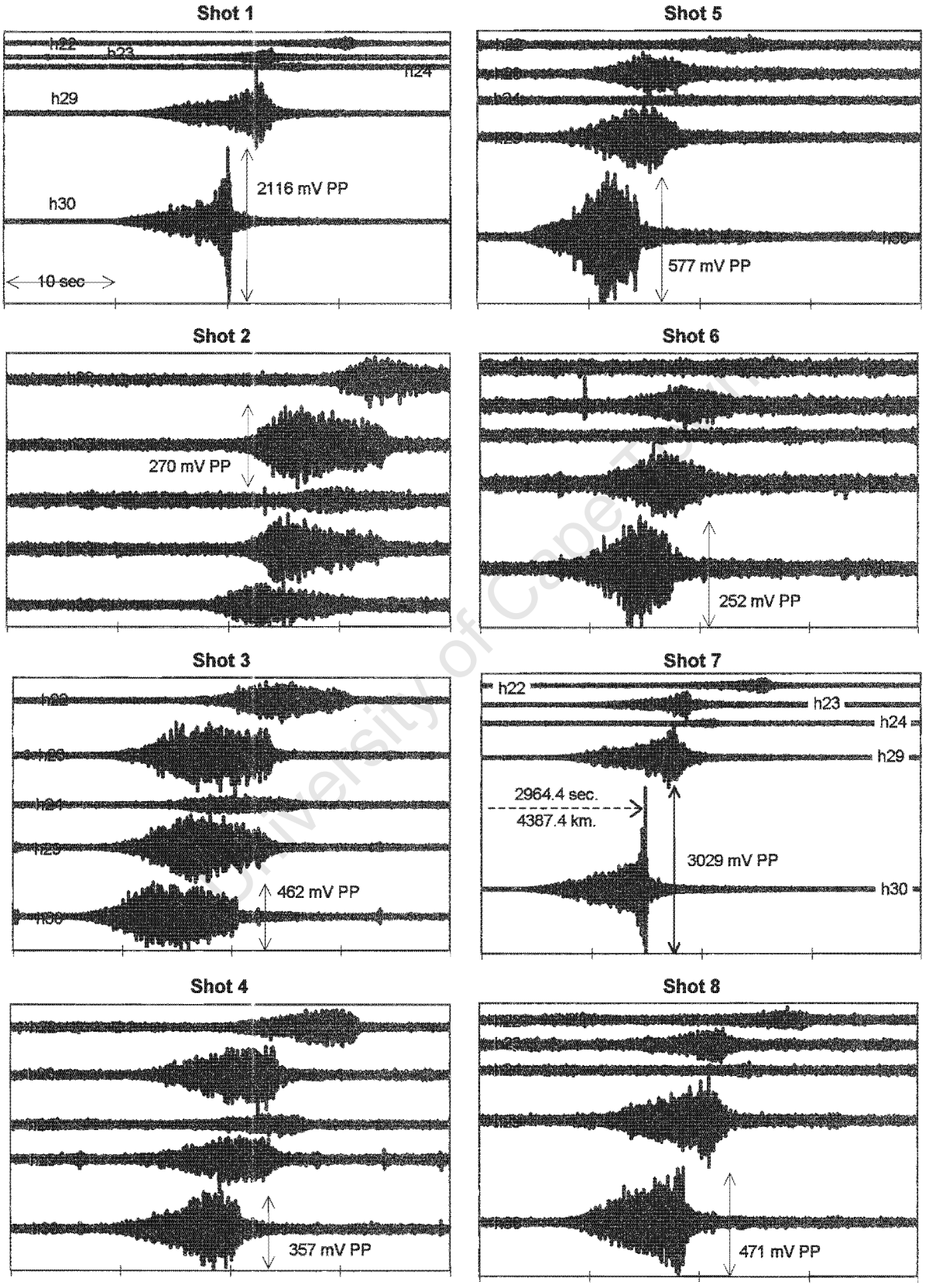

Figure 1-1. Signals received at Ascension

1. Introduction

This deep sound channel is found in temperate and tropical areas of oceans worldwide and is often referred to as the SOFAR channel. Ewing and Worzel first reported on long-range acoustic propagation measurements in this channel in 1948. An understanding of the effects of this channel is essential for long-range sonar and ocean acoustic tomography.

1.3. Explosive sources

Long-range underwater propagation requires high power low frequency sources. Unfortunately, high power low frequency underwater sound projectors are generally expensive to manufacture and maintain and are inefficient as energy converters. Explosive sources are an exception to this rule, being relatively cheap and providing powerful broadband signals. They have other shortcomings, such as producing only non-deterministic wide-band impulses. They were widely used in experimental and sonar applications for many years but have mostly been replaced by other devices, such as electro-acoustic transducers in sonar and arrays of air guns in seismic surveying (Urick, 1983, p. 95-97; Collins *et al.*, 1998). These other devices have the advantage that they can be adapted to specific requirements to provide repetition, synchronicity, directionality, or coded waveforms.

The largest underwater explosions ever detonated may have been those in a series of experiments named *Chase* and *Artemis*. Explosive of up to one kiloton were used and reflections off major undersea topographical features could be recognised as far away as 4000 kilometres (Goertner, 1980).

In a study with some similarities to the test described in this thesis, Bryan *et al.* (1963) detonated a series of more modestly sized shots (3 and 48 pounds in mass) to determine the accuracy of position fixing in the southern Atlantic. The shots were dropped from a vessel travelling through the southern Atlantic and past Cape Town in a southeasterly direction. Signals were received for ranges up to 4700 nautical miles. The shots were received at SOFAR stations at Fernando de Noronha (off the eastern coast of South America) and at Ascension Island. An equation for signal duration as a function of range and the speed of the first and axial arrivals is given in the paper. (This relationship, written with group sound speed as a function of depth, is implicit in equations 3-2 and 3-3 in this thesis.)

1. Introduction

In 1960, shots detonated off Perth, Australia in the SOFAR channel were recorded on hydrophones at Bermuda. The start and end points are within less than 2 degrees (about 200 kilometres) of being antipodal. Analysis of these shot paths by Munk *et al.*, (1988) and Heaney *et al.*, (1991), led to a realisation of how sensitive long-range undersea transmissions are to ocean conditions. This realisation was one of the starting points of the HIFT (Heard Island Feasibility Test) and ATOC (Acoustic Thermometry of Global Climate) projects.

1.4. HIFT and ATOC

Concern about global warming gave rise to HIFT (The Heard Island Feasibility Test, Munk and Forbes, 1989 and Baggeroer and Munk, 1989). The measured increase of greenhouse gases in the atmosphere should result in a global increase in atmospheric temperature. Such an increase would be moderated by the oceans that store both heat and greenhouse gases. The increase of heat in the ocean should be measurable, if the measurement technique can discriminate against the shorter-term local heat fluctuations while identifying the underlying longer-term trend. This is what long-range acoustic thermometry sets out to do.

The objective of HIFT was to determine the feasibility of using extremely long-range coded signals to measure average signal travel times with a precision of 10 to 50 milliseconds. In HIFT, a deterministic sound source suspended from a ship near Heard Island was received at various receivers worldwide, including Bermuda and Ascension in the Atlantic Ocean. The phase stability of the received signals was surprisingly good, but problems arose from the use of a non-stationary source and paths crossing the Antarctic Front.

The ATOC (Acoustic Thermometry of Global Climate) project has the purpose of quantifying global warming and calibrating global climate models by acoustically measuring the heat variability in the oceans (Munk *et al.*, 1994 and Munk and Baggeroer, 1994). Both transmitters and receivers are stationary and paths are chosen to avoid ocean fronts. The ATOC concept utilises:

- The increase of sound speed with increasing water temperatures and
- The spatial filtering effect provided by transit time measurements over larger distances to average out temperature disturbances over smaller ranges, and

- Repeated measurements over a period of months and years to average out over longer-term disturbances.

1.5. ATOC-FACT

ATOC-FACT (Acoustic Thermometry of Global Climate - Feasibility, Ascension to Cape Town) was first suggested by Dr. Dave Palmer. He saw the path from Cape Town to Ascension as an obvious candidate for global ATOC monitoring and the reception of ATOC signals as an extension of the service provided by the listening facility at Ascension.

At first, the intention was to make use of a source that provided some control of the wave-form. Such sources could not be found and time was passing. One of our concerns was that the Ascension facility could be shut down as part of a budget reduction by the United States. We decided to do the test with explosive sources, thereby sacrificing exact timing, repetitions at will, and control of spectral content of the transmitted signals. This meant that we would not be able to determine travel time, and hence water temperature, with any meaningful accuracy. (Palmer (1994) estimates the best travel time precision obtainable from the explosive sources on this path to be 0.1 second.) We would also probably not be able to identify specific ray paths. We hoped, however, to learn about the extent of topog-raphic interference and we thought that we would be able to quantify the transmission in some simple way from the results.

1.6. Thesis – objectives and scope

The waveforms received in this experiment are shaped, and their path is directed, by the processes of absorption, spreading, focusing and differential delay in the sound channel, blocking by seamounts and undersea ridges, changes in the radius of curvature of the earth, horizontal refraction by temperature gradients, and diffraction around seamounts. Some of the shots occurred in or near a filament of warm water, causing the waveforms to be modified in the process of coupling into the surrounding colder water The contribution of each of these processes to the final waveforms is not clear.

The Ascension data set is unique in terms of the quality of the digital recordings, repetition of shots and simultaneous reception at different sites. This allows for exact analysis of the waveforms and for testing different formulations of the wave-shaping processes against a number of different results.

1. Introduction

The thesis objective is to perform a thorough analysis of the data to identify, understand, and, through the use models, to quantify the effects of propagation through an ocean with areas of different temperature profiles and topographical interference.

The work consists of:

- Processing the data to extract usable waveforms from noise and determining peak signal amplitudes and duration.
- Determining great circle trajectories and geodesic distances for the sound from source to receiver and determining possible topographic interference by sea-mounts or ridges along the path.
- Predicting the expected waveforms using both ray and modal propagation models since these models provide different but complementary views.
- Comparisons of predicted and recorded waveforms.
- An investigation into mode changes or reflections that may have taken place.

The thesis should:

- Reduce the risks associated with the choice of exact positions for the sources and receivers at Cape Town and Ascension.
- Establish methods of analysing the results of shot tests.
- Assist in the understanding and interpretation of results obtained from ATOC tests in areas where the signal is coupled between areas with different temperature profiles or where topographic interference occurs.
- Provide a better understanding of the effects of reflected rays.

The environment in which the test was done contains numerous undersea mountains and the southwestern part of the area is subject to occasional massive influxes of warm water. These conditions make acoustic propagation tests more difficult to perform and analyse, but they are representative of somewhat extreme conditions in much of the tropical and temperate oceans of the world. In dealing with this, the thesis can be of use for understanding and analysing such conditions elsewhere.

The approach taken in this thesis is to use the simplest assumptions and models effective for an understanding of the underlying mechanism. High precision of matches between models and results should not be expected. Urick (1983) devotes several pages to discuss-

ing fluctuation in transmitted sound (p. 167 to 194) and comments: "The sea .... is not a simple propagation medium for sonar, as is the atmosphere for radar, but is variable in time and space and in supporting propagation via multipaths". For ATOC-FACT, the non-deterministic nature of the sources precludes the use of most of the newer signal processing techniques to reduce this signal fluctuation.

1.7. Thesis contents

After this introductory chapter, Chapter 2 describes the execution of the experiment and details some of the results, including the waveforms recorded at Ascension. The untangling of causes and their effects begins in Chapter 2 with the recognition of some obvious patterns relating to sources and paths.

Chapter 3 contains a brief review of ray trace and normal mode modelling, presented as an aid to understanding the physical process of SOFAR sound propagation. The concept of a time window (analogous to the depth window in the ray trace model) limiting the start and end of direct rays is introduced. A family of arrival waveshapes predicted for 4.4 Megametres is compared with observed waveshapes at three of the hydrophones.

Chapter 4 considers the patterns of the amplitudes received at the hydrophones (neglecting differences between shots) and compares these amplitudes to undersea obstructions encountered along the path.

Chapter 5 applies the concept of time windowing to the received signals and shows that the early parts of the received signals have to consist largely of reflected energy. It investigates possible ray paths for the early-reflected rays and shows how the steepness of the ray (and the depth of the ray turning point) can be changed on reflection.

Chapter 6 identifies some discrepancies in shape and arrival time between the model prediction and the recorded waveforms. A deeper sound channel axis is modelled for a closer approach to matching the peak amplitudes and arrival times. The deeper sound channel axis gives a better match for the sources closest to the filament of warm water.

Chapter 7 takes a retrospective look at the experiment and some aspects of the thesis, discusses the Cape Town to Ascension path considering the knowledge gained in the

1. Introduction

thesis and makes some suggestions for the use of explosive charges and siting of ATOC sources.

The appendix contains examples illustrating modelling procedures, calculations and processing methods in support of the main document. Many of the files are in Mathcad, which records calculations in a fairly easily readable form. The equations in the main body of text are also in Mathcad. The first section of the appendix gives a brief introduction to the Mathcad format .

Chapter 2. ATOC-FACT Test

The ATOC-FACT (Acoustic Thermometry of Global Climate - Feasibility, Ascension to Cape Town) transmission test was done in November 1992 to evaluate the propagation of undersea sound from a number of sites near Cape Town to Ascension. This chapter describes the test, shows the results, and makes some of the comparisons that are immediately evident.

2.1. Test execution

The shots were placed on a line that started at Cape Town and ran southwest for maximum change in subtended angle at Ascension for minimum excursion distance. Successful receptions from the easterly sites on the edge of the continental shelf would demonstrate the feasibility of siting an ATOC receiver or transmitter near Cape Town in an area easily accessible by cables from shore and with a relatively good infrastructure. The more southwesterly sites were chosen to provide a reference acoustic path clear of potential topographic interference from known undersea features such as Seamount Bonaparte and St. Helena. (Figure 2-1.)

Given the possibility of screening by Walvis ridge, St. Helena Island, and seamount Napoleon, the amount of attenuation along the path was uncertain. To ensure reception of reasonable amplitude signals at Ascension, it was planned to detonate two different size charges at each of five sites, after an initial test with one of the smaller charges. The charges chosen were 8 and 25 kg of TNT.

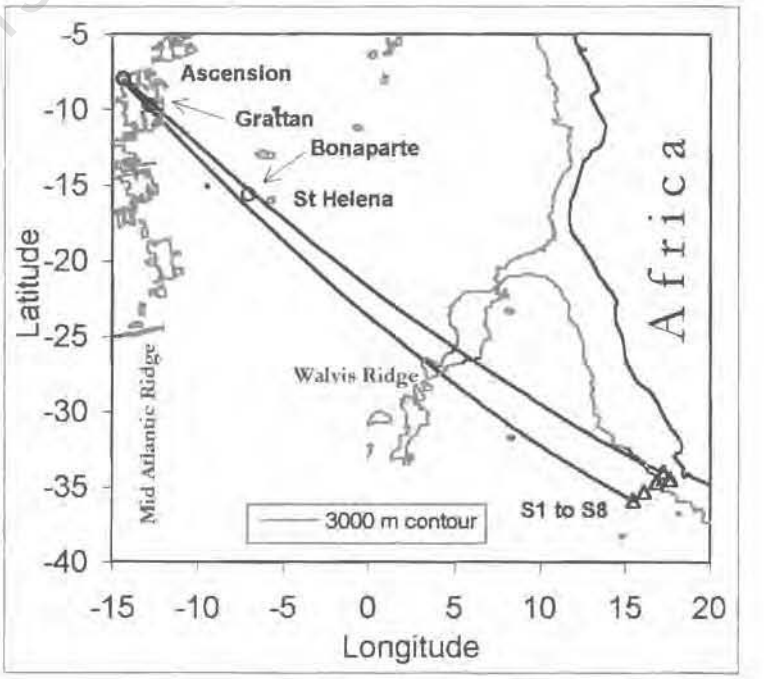

Figure 2-1 ATOC-FACT sites, sound paths and possible sources of topographic interference.

2. ATOC-FACT Test

The detonations took place in November 1992, from the South African Naval vessel, SAS Umkomaas. Figure 2-2 shows the detonation sites. Special canisters had been manufactured and filled with TNT. They were armed on site with electrical detonators and let down at the end of an electric cable to the estimated depth of the sound channel. This allowed detonation at a fixed time, but the on-site depth estimates were to prove badly in error, particularly when strong currents were present. In the event, the second, third and fourth of the smaller charges would not detonate. It seems probable that water penetrated a small volume of air near the detonator and shorted out the electrical detonation impulse. On the charges deployed subsequently, this volume was filled with a silicon sealant after the detonator had been inserted. All the later charges detonated successfully, but at the sites of shots 2, 3, and 4, only the larger charge was fired, due to the shortage of the smaller charges. Shot positions and times were recorded using a Global Positioning System receiver. Receptions at Ascension were recorded with GPS time markers.

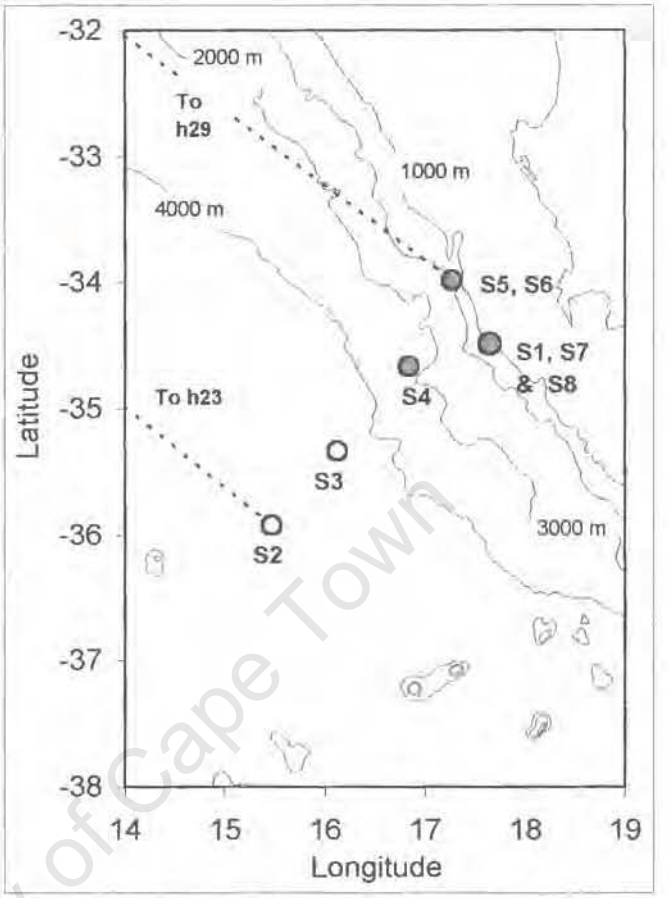

Figure 2-2 Shot sites southeast of Cape Town

2.2. Sound Speed Profile for the path

An article by Munk *et al.* (1988, Figure 7) shows that the sound speed minimum is 1482 metres per second at Ascension and gradually changes to 1480 metres per second over the length of the path to the source location. The sound speed minimum occurs at 800 metres at Ascension and remains fairly constant until 22 degrees south, where it starts going deeper to reach about 900 metres at the source location. In addition to these average conditions, the variability of the sound speed profile increases towards the south and

southwest. The occasional incursion warm water described in the next section is one of the causes of this variability.

2.3. Warm water from the Agulhas Current

A long filament of warm water from the Agulhas current had moved into the planned source area before the test and it seemed likely that this would affect the sound speed profile in the area close to the sources. Due to the failure of equipment intended for taking bathythermographs from the deployment vessel, the actual profile could not be verified from the vessel doing the test.

However, copies of satellite images of sea surface temperatures were obtained. A copy of the best picture (and closest in time) not obscured by clouds is shown in Figure 2-5. The positions of the shots relative to the swirl of warm water originating in the Agulhas current

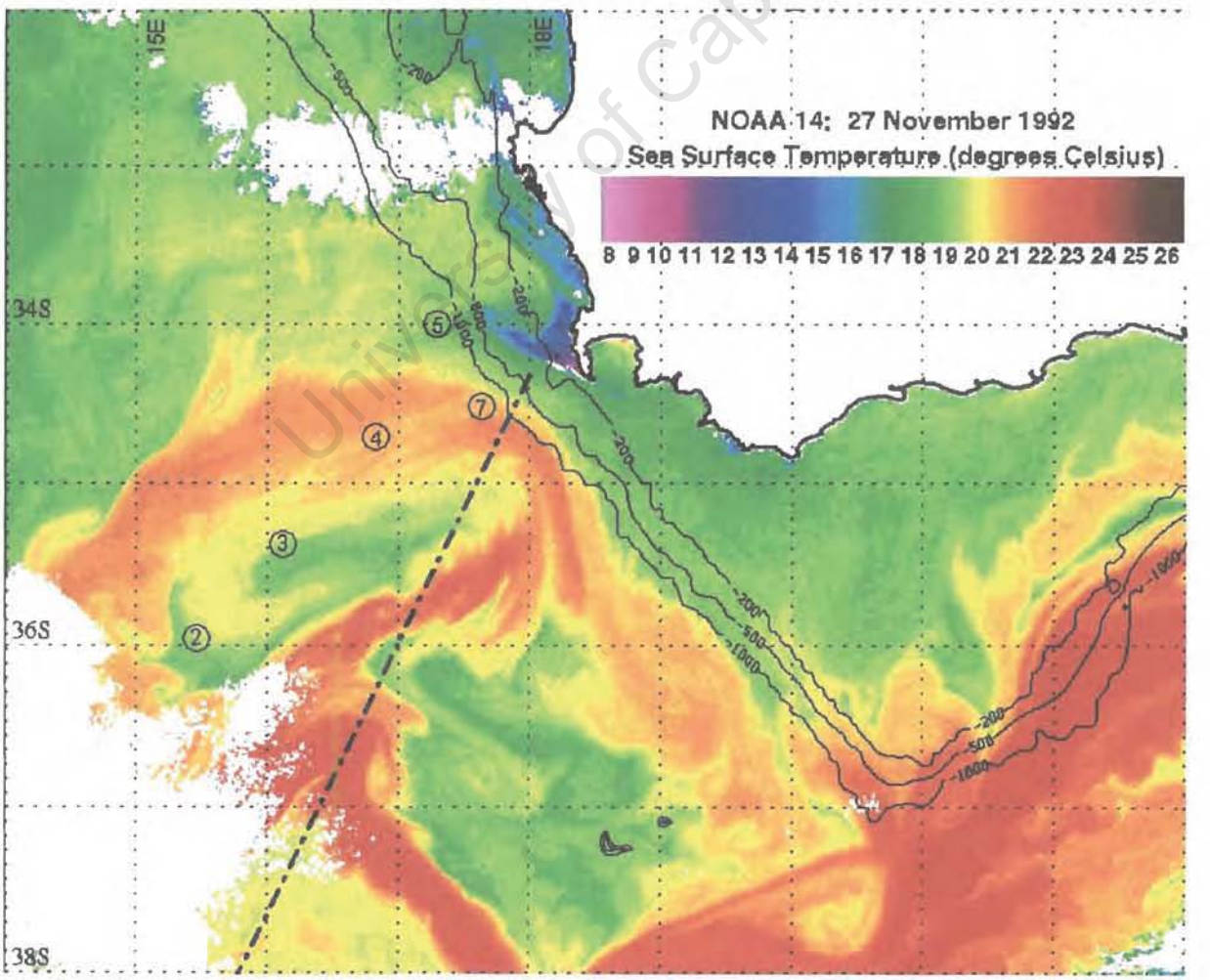

Figure 2-3 Sea Surface Temperatures.

and extending westward are shown inside the black circles. The digit "5" indicates the site for shots 5 and 6 and the digit "7" indicates the site for shots 1, 7 and 8. Other satellite images in this series (not shown) show that the northwestern arm of the body of warm water did not change much in position between the image in Figure 2-5 and the day of the main test.

The German research vessel Polarstern took a series of XBT readings at this time while underway from Cape Town to Neumayer research station in the Antarctic. The details of this voyage are given in: Reports on Polar Research 135/94, "The expeditions ANTARKTIS X/6-9 of the Research Vessel 'POLARSTERN' in 1992/3."

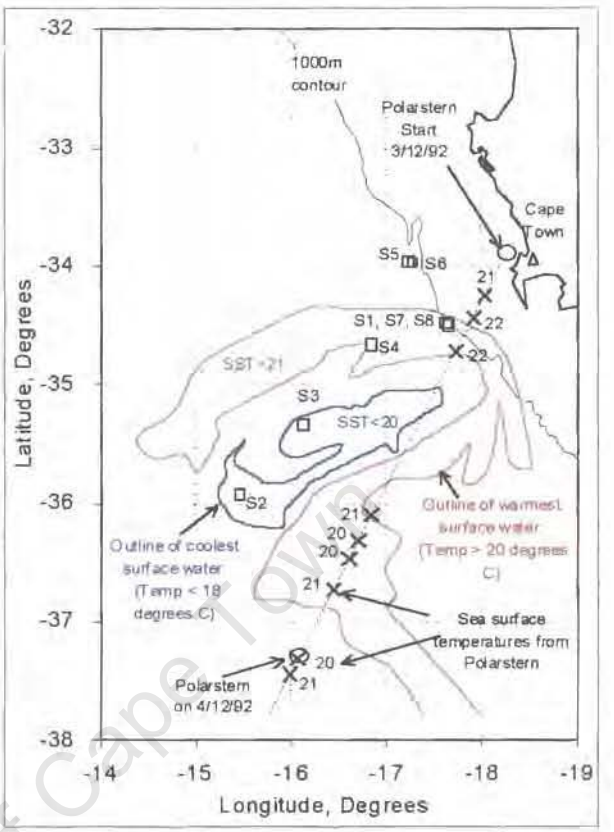

Figure 2-4 Route of the Polarstern and SST contours.

Figure 2-4 shows the shot sites and the route of the Polarstern with approximate coordinates for the sea surface temperatures and XBT recordings on the Polarstern. The red and blue lines are crude contours of sea surface temperature taken from Figure 2-3 and included here for orientation.

Figure 2-5 shows the first part of the XBT section recorded on board the Polarstern during the voyage. It travels through a narrow warm filament (22 °C) near 34.5 degrees south that is in good agreement with the satellite image. Further south, between 35.5 and 37 degrees, the section shows an area with temperatures between 20 °C and 21 °C. This corresponds very roughly with the satellite measurements of sea surface temperatures shown in Figures 2-3 and 2-4. Since the measurement by satellite was on 27 November 1992 while the Polarstern started her voyage on 3 December 1992 and passed 37 degrees south on 4 December 1992, some difference in surface temperature distribution is not surprising. An arm of this warm water lay across the line of the sources, with S2, and S3 lying to the southeast of the lower arm. S4 lay inside, or at least on the edge, of the arm of warm water.

2. ATOC-FACT Test

S1, S7, and S8 were located on the northeastern edge of the arm while S5 and S6 to the northwest of the arm appear to be clear of the warm water. (Near Cape Town, the likelihood of encountering warm water eddies increases farther offshore according to Garzoli *et al.*, 1995, in a study of southern Atlantic currents. This report describes an Agulhas Eddy Corridor stretching from southeast to northwest off Cape Town.)

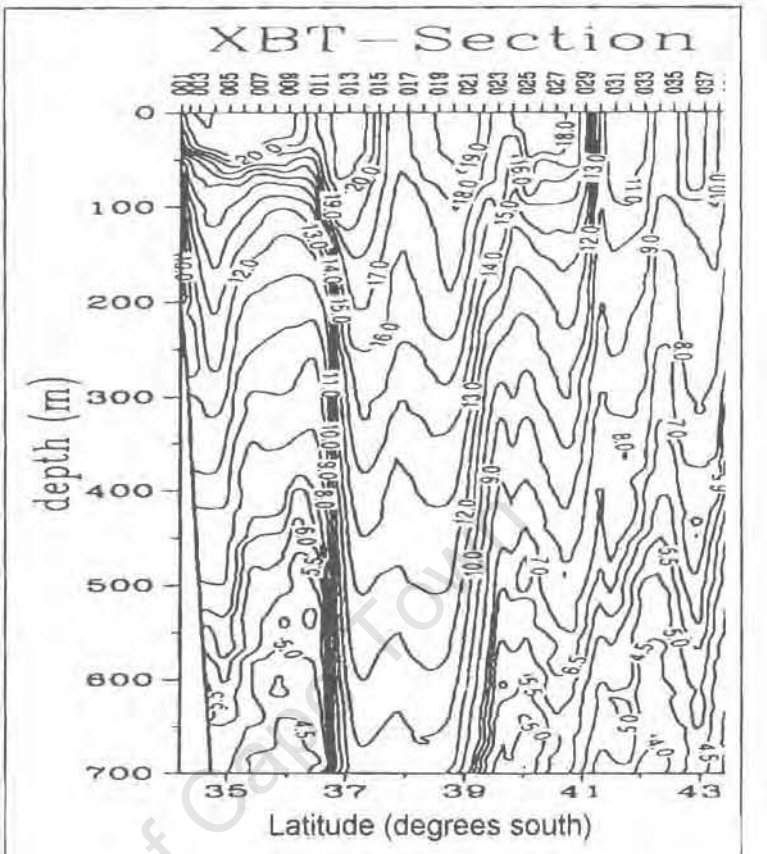

Figure 2-5 Polarstern XBT section

The XBT section runs almost parallel to the line through shots 4, 3, and 2 and down the length of the upper arm of warm water lying between 37 and 39 degrees south. The upper arm consists of a warm water filament that meanders across the XBT section three times. Just north of 37 degrees the surface temperatures rise abruptly and then decrease again – this marks the point where the Polarstern crosses the filament of warm water for the last time. After 37 degrees south there is an abrupt transition to colder water. At greater depths, the location of this crossing is not so sharp. As the depth increases the upward pointing peak marking the filament of warm water moves farther north until it centres at 36 degrees south at a depth of 700 metres. A cold area (downward peak) is situated at about 35 degrees south. This downward peak is horizontally displaced northwards with increasing depth. Unfortunately, this pattern does not indicate what is happening at shots 2 and 3. It will be shown later that there is reason to believe that the sound speed profile was depressed by hundreds of metres at shots 2, 3, and 4. The picture built up here does not confirm this, but also does not preclude the possibility of the sound speed profile being displaced downwards.

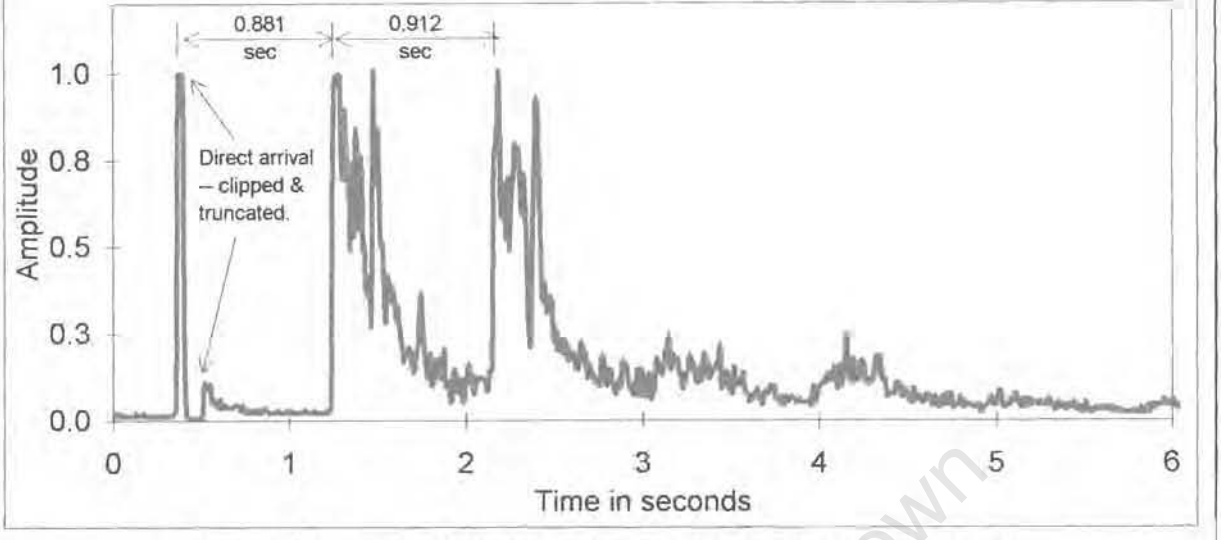

Figure 2-6 Timing of shot arrival and echoes for shot 1 at source

It seems reasonable to assume that the temperature structure of the warm water filament measured by XBT in the southeast portion also applies to the northwest portion of the warm water filament. Overall, the XBT measurements confirm the picture of a filament of warm water extending downwards for hundreds of metres.

2.4. Recordings at the source

The first four shots were recorded using a hydrophone deployed near the sea surface. Unfortunately, the tape recordings were contaminated with radio frequency interference from the ship radio, making them difficult to interpret. On the fourth recording an intermittent fault in the tape recorder caused it to stop recording at random times, resulting in an indecipherable record. After the fourth shot, the hydrophone cable became entangled in the propeller of a small boat and the hydrophone was rendered unusable for the rest of the shots.

The recordings for the first three shots proved usable, in that the echo delays after the first and second reflections could be determined. Figure 2-6 shows the envelope of the absolute values of the recording for shot 1, annotated with the delays between the direct arrival and the bottom-surface and surface-bottom-surface reflections. Figure A-4 in the appendix is an example of the vertical sound paths and associated delays. The detonation depths calculated from the recorded times using the equations in Figure A-4 are given in Table 2-1. Since only three shot depths could be calculated by this method, an alternative is described next.

2.5. Bubble pulse modulation

An underwater explosion forms a gas bubble that expands rapidly and then collapses under ambient pressure, rebounds, and oscillates while the gas globe migrates to the surface (for shallow explosions) or is extinguished (for deeper explosions). The sound radiated from the explosion is modulated by the oscillation of the bubble. The frequency of oscillation of the gas globe is a function of the maximum bubble size, which in turn depends on the mass and type of the explosive charge and on ambient pressure, which is determined by the depth of the explosion. The frequency of the first bubble pulse can be calculated from Equation 1-1. (Urick, 1983, Arons, 1948)

$$d = 2.11 \cdot m^{\frac{1}{3}} \cdot f^{\frac{6}{5}} - 10 \quad \text{..... Equation 2-1}$$

where d is the depth of the explosion in metres
m is the mass of the explosive of TNT in kilogram
f is the bubble pulse frequency in Hertz

The maximum size of the second bubble is smaller than the first. This results in an increased modulation frequency, but at reduced amplitude. The modulation frequency of the first pulse is about 72% of the second. Subsequent bubble pulses continue to increase in frequency and decrease in amplitude. The first two bubble pulses have most effect on the radiated sound. The effect of this modulation can be seen in the frequency spectrum of the radiated sound of shot 5 in Figure 2-7. The spectrum shows a series of peaks that result from modulation at the fundamentals and harmonics of 17.5 and 24.4 Hz

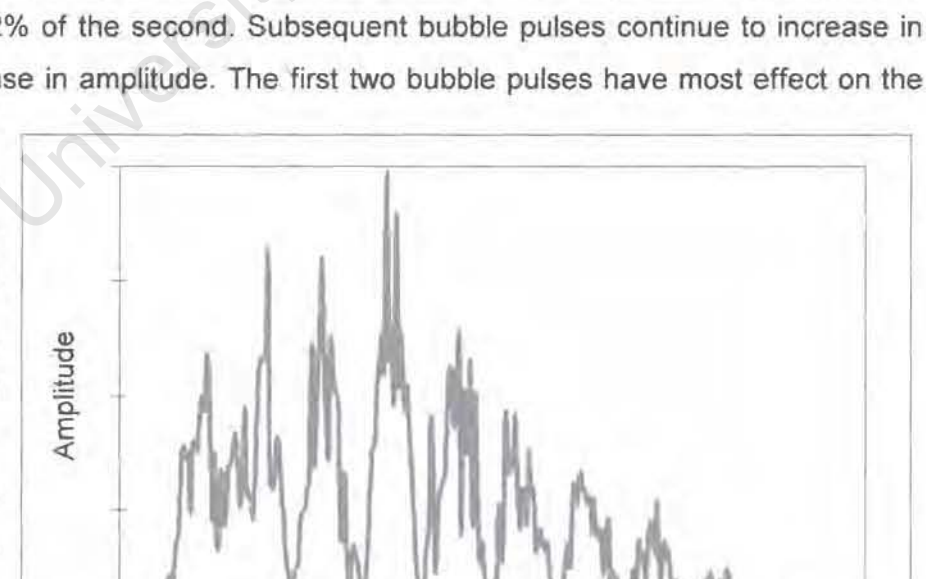

Figure **Error! Style not defined.**-7 Spectrum of S5 recording

bubble pulse frequencies. (The spectra of all the shots is shown in Figure A-1 in the Appendix.) The bubble pulse frequencies can be determined by taking the cepstrum of the signal (Urick, 1983, Mitchell *et al.*, 1976, Collins *et al.*, 1998). For the shots received at Ascension during ATOC-FACT, this bubble pulse modulation provides a way of checking shot depth calculated from the surface and bottom reflections for the first three shots and for determining the depth of the rest of the shots. The figures calculated from bottom reflection and the bubble pulse modulation frequencies are compared in Table 2-1. The calculation of source depth and the determination of the bubble pulse frequencies from the cepstrum are shown in appendices A.8 and A.9.

Shot	Date	Time	E Long.	S Lat.	Shot Mass	Depth*	Depth+
S1	1992/11/23	12:33:14	17.648	-34.488	7.99	706	738
S2	1992/11/30	10:56:30	15.465	-35.926	25.10	465	514
S3	1992/11/30	16:45:30	16.127	-35.339	24.85	675	681
S4	1992/11/30	21:28:00	16.835	-34.666	25.40	-	507
S5	1992/12/01	7:32:00	17.269	-33.983	25.38	-	403
S6	1992/12/01	8:40:30	17.228	-33.960	7.99	-	401
S7	1992/12/01	12:56:00	17.640	-34.483	24.60	-	765
S8	1992/12/01	14:06:00	17.620	-34.485	8.04	-	440
	yyyy/mm/dd	HH:MM:SS	Degrees	Degrees	kg. TNT	Metres	Metres
*From bubble pulse +From bottom reflection time							

2.6. Shot times, coordinates and depths

The shot times in Table 2-1 are in HH:MM:SS from GPS. The accuracy of the shot timing is estimated as plus or minus 1 second. This figure includes:

- The timing errors incurred by countdown from a GPS clock to an operator pushing a detonator button,
- The positional error from the GPS receiver on the main vessel to the subsurface charge at the end of a cable several hundred metres long below a secondary craft about 50 metres from the main vessel, and
- GPS positional inaccuracy.

	Longitude	Latitude	Depth
h22	-14.49	-8.01	800
h23	-14.42	-8.07	800
h24	-14.45	-8.06	800
h29	-14.27	-7.95	800
h30	-14.26	-7.99	800

Table 2-2 Hydrophone Coordinates

A strong current from the northwest hampered deployment of charges 5 and 6. The second last column of Table 2-1 shows source depth as calculated from reflection times of the

source recordings. The last column shows source depth calculated from the modulation frequency (bubble pulse frequency).

2.7. Recordings

All eight shots were recorded at both Ascension and Bermuda. Dr. Andrew Forbes, on the Australian fisheries research ship, the Southern Surveyor, recorded shot 2 off the south coast of Tasmania. The signals recorded at Ascension were amplified where required, stored on tape, digitised by sampling at 1 kHz, recorded with a resolution of three to four decimal digits, and transmitted to the USA. The coordinates and depths of the hydrophones at Ascension are listed in Table 2-2. The frequency spectra of the signals (after filtering out frequencies lower than 15 and higher than 150 Hz) are shown in Figure A.1.

2.8. Arrival waveforms

The hydrophones at Ascension were not calibrated to an absolute level but the amplifiers were set so that the background noise in the sea, on average, gave an output of - 45 dB re 1 millivolt rms. The received signals shown in Figure 2-8 and 2-9 were amplified by 60 dB to give a background noise level of +15 dB re 1 millivolt (15.9 mV peak-to-peak). The detonation and reception times, ranges and travel times are shown in Table A-3 in the appendix.

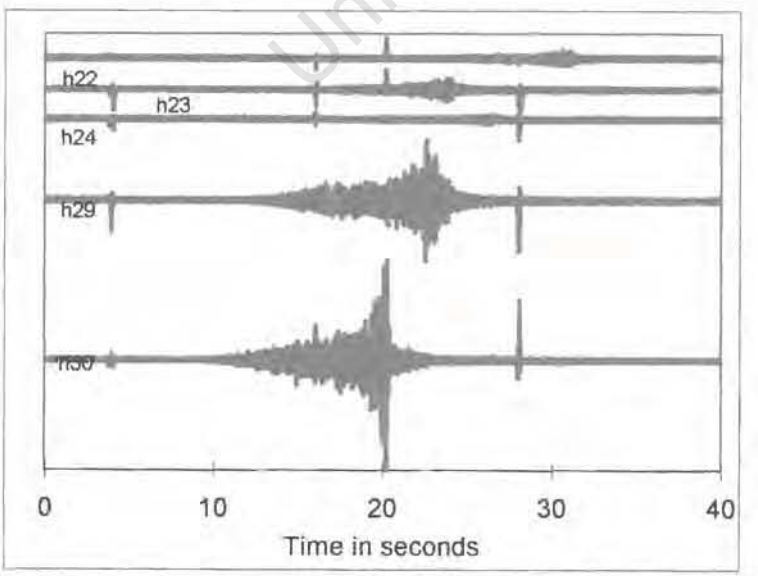

Figure 2-8 Received signals (S1) with radar spikes.

2. ATOC-FACT Test

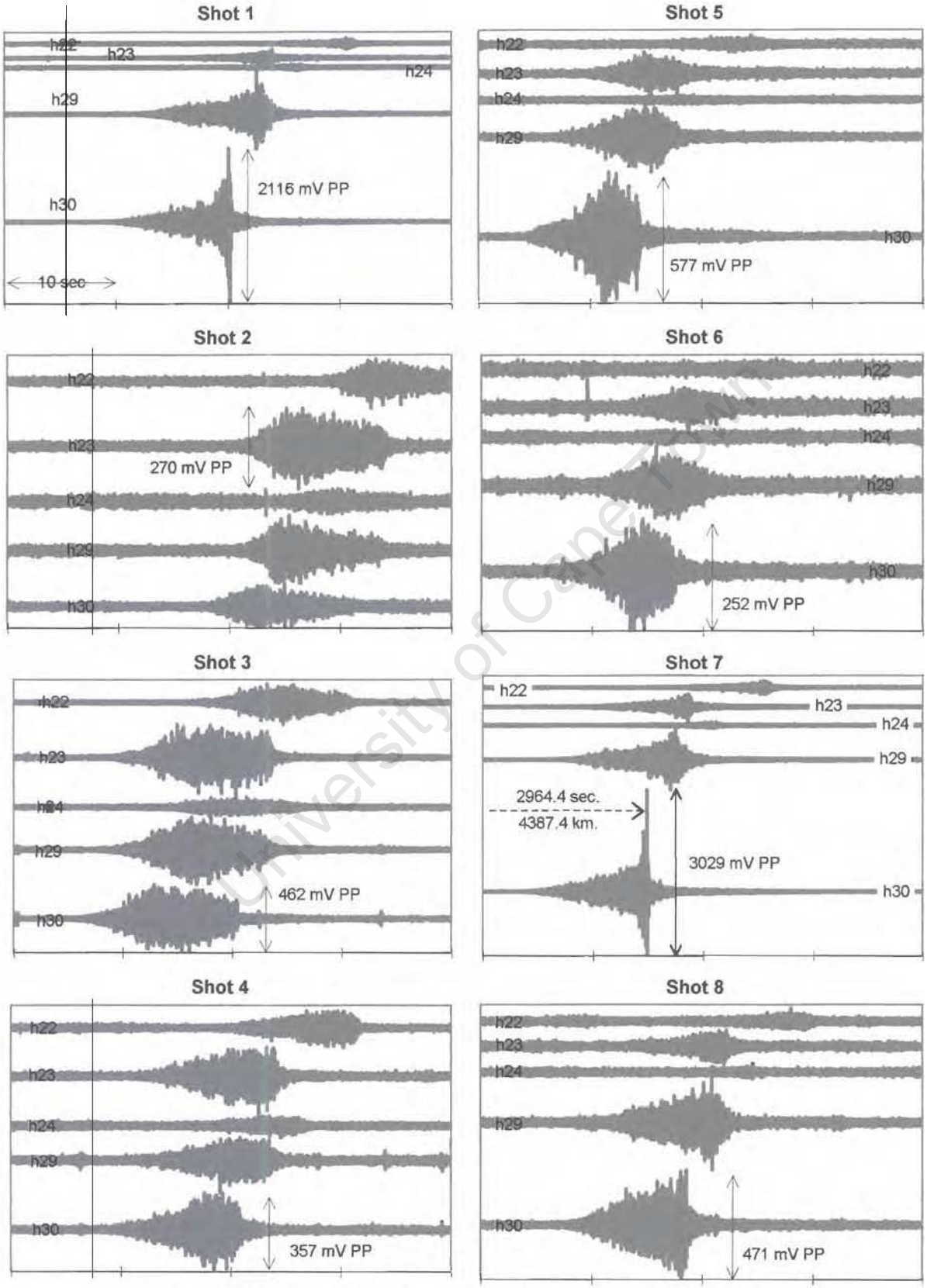

Figure 2-9 Signals received at Ascension (Repeat of Figure 1-1.)

Fig. 2-8 shows the signals received from the first shot. The prominent vertical lines present at about 12 second intervals are due to radar interference during transmission of the digitised signals from Ascension.

Figure 2-9 shows the recordings of all eight shots. The spikes due to radar interference have been removed by a specially constructed spike filter and by high and low pass filters that remove energy at frequencies outside the signal bandwidth of 15 to 150 Hz. The spectra of the shot signals are shown in Figure A-1 in the Appendix. The largest signal amplitudes received vary by a factor of about 10 between shots. The smallest signals are hardly detectable above the background noise. A summary of the calculated source level, transmission loss and signal-to-noise ratios is given in Appendix A-2.

The timing of the signals between hydrophones is preserved in the recordings and in Figure 2-9. A timing channel was recorded for each shot and digitised along with the five hydrophone channels to give an exact time reference. As an example of the time delays between hydrophones, it can be seen that the signals arrived first at hydrophone 30 and last at hydrophone 22. The delay in arrival time between these two signals is about 10 seconds (Palmer, 1994). Detonation and reception times are listed in Table A-3 in Appendix A.7.

There are differences in amplitudes both between shots and between hydrophones in Figure 2-9. There are also some obvious patterns. For instance, the time delay of each hydrophone is relatively constant for the different shots, since the angle of arrival for different shots at Ascension changed by only about 4 degrees from S2 to S5. Another obvious pattern is in the hydrophone amplitudes – hydrophones 30, 29, and 23 have the largest amplitudes while hydrophones 22 and 24 have the smallest.

2.9. Best signals

Each shot is received with maximum amplitude on one particular hydrophone. These receptions for each shot are displayed in Figure 2-10. For compactness, only the positive peak-detected function of each signal is displayed. The amplitudes have been normalised to the peak value of shot 7 as received on hydrophone 30 and adjusted for the different mass of charge of the shots according to equation 1-2 below. The peak amplitudes of the signal have been preserved by taking a running maximum value. (The processing is shown in Appendix A.10.)

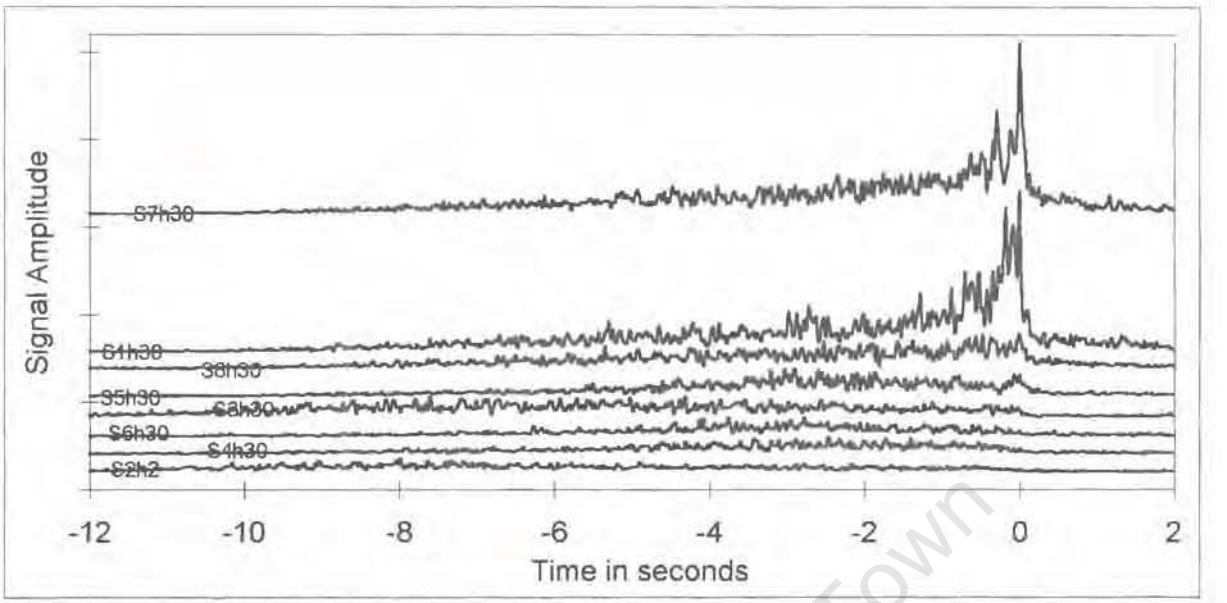

Figure 2-10 Positive envelopes of the best signals for each of the shots.

2.10. Peak pressure as a function of explosive mass and distance

Equation 2-2 (from Urick, 1983) provides the means of compensating the received pressure amplitude for different size charges. The charges were approximately 25 and 8 kilogram mass. Using the larger charge as the norm, the pressure peak from the smaller charges has to be increased by a factor of $(25/8)^{1.13/3}$, that is, by approximately 1.54, for the comparison.

$$z = 2.11 \, m^{\frac{1}{3}} \, f^{\frac{6}{5}} - 10 \quad \text{..... Equation 2-2}$$

where P = Peak pressure resulting from the explosion
m = mass of explosive
r = radial distance in metres from the centre of the explosive mass

2.11. Finding patterns in the received signals

The differences between signals are due to three types of factors. The first of these is changes at the source, such as the size of charge and the depth of detonation relative to the axis of the sound channel. The second factor is path differences such as distance, sound speed profile, and topographical interference. The third factor is differences due to the hydrophone, such as sensitivity, noise, and depth. The problem is to untangle the effects of the different factors. Differences at the source mainly affect the shape of the signal, while path differences change signal attenuation and duration. Differences at the hydrophone should be constant for the duration of the test.

2. ATOC-FACT Test

Source differences: As an example, a difference due to the shot affecting the shape of the signals can be seen between shots 7, 1 and 8. These three shots occurred at almost exactly the same site, but shots 7 and 1 have shapes that tend towards the expected SOFAR shape (a slowly increasing amplitude with a large, sharp peak just before the signal termination) (Urick, 1983; Porter, 1972; Munk, 1974; Guthrie, 1972) while the amplitude of shot 8 increases almost linearly with time up to the termination. This difference must be mainly due to the shot since the paths and hydrophones are the same for all three shots. Chapter 3 will show that the size of the peak is determined by the source and receiver depths relative to the sound channel axis.

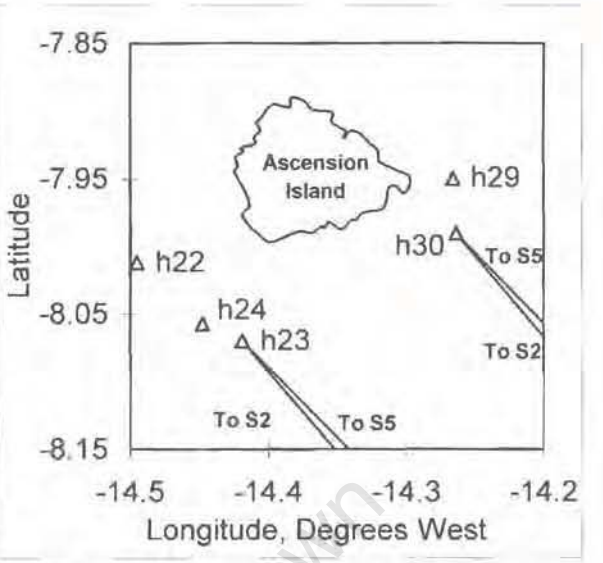

Figure 2-11 Ascension receiver sites

Path differences: The path usually changes with both the shot and the hydrophone. However, with the help of topographical plots, it is possible to identify some of the topographical features affecting the signals. For example, Figure 2-11 shows that hydrophones 23, 24, and 22 are almost in line for the shot signals, particularly for the more northeasterly shots. These three hydrophones share almost identical paths up to h23, yet there is a considerable difference in the amplitude of the received signals. This difference must be due to topographic interference encountered in the short shallow section of path after the signals pass h23.

In Figure 2-12, the amplitudes of the received signals have been normalised to the peak amplitude received at hydrophone 23. This shows up an unexpected result –

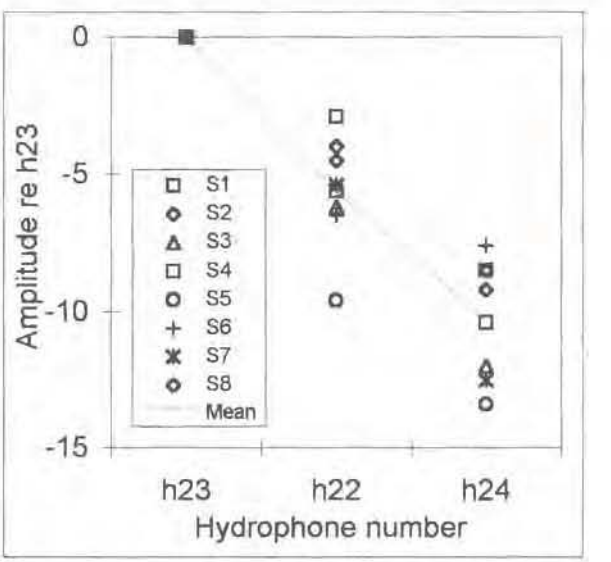

Figure 2-12 Hydrophone comparison – h23 outperforms h22 and h24.

hydrophone 24 receives less signal than hydrophone 22 although it is closer to hydrophone 23 and undersea obstacles blocking hydrophone 24 could be expected to also block hydrophone 22. It is probable that hydrophone 24 was lacking in sensitivity as compared to the other hydrophones, both for this test and for HIFT (Palmer *et al.*, 1994), but the low sensitivity might also be due to local topographical screening over a relatively large sub-tended angle. (Dr. Dave Palmer, who retrieved the signals from Ascension, remarked that hydrophone 24 had been noisy for some time.)

Hydrophone differences: All the hydrophones are reported as being at the same depth, 800 metres, which is also the depth of the sound channel axis at Ascension. Hydrophone depth should therefore not cause any perceptible differences. It is also reasonable to assume that the sensitivity of each of the hydrophones was constant for the duration of the test.

2.12. Representative hydrophones

It seems probable that the signals at hydrophones 22 and 24 are only attenuated replicas of the signals at hydrophone 23. To simplify the presentation of results, hydrophone 23 will be taken as representative of hydrophones 22 and 24.

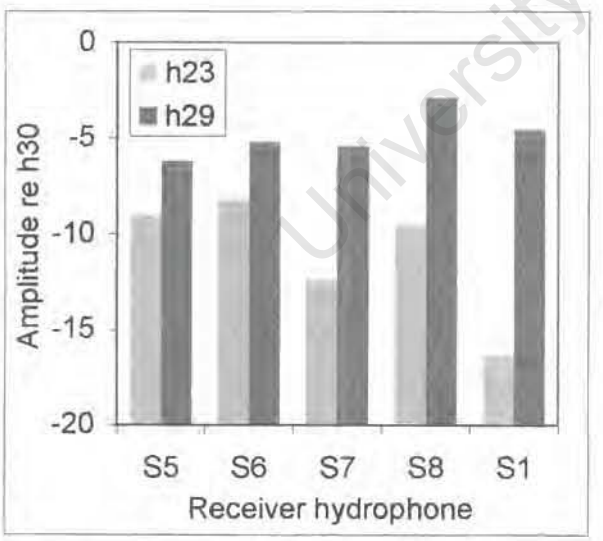

Figure 2-13 Normalised signals compared to h30

2.13. Similarity in paths

The shot sites are spaced out along a 270-kilometre line running from southwest to northeast. However, shots 5 and 6 are within 4.6 kilometres of each other and shots 1, 7, and 8 are within 2.7 kilometres of each other. The positions are plotted in Figures 2-2 and 2-11 while distances between sources and hydrophones are given in Table A-3 in the appendix. As with the hydrophones that lie on the same bearing, one would expect similar results from shots with the same tracks once the differences in the shot amplitude and other source differences have been discounted.

2. ATOC-FACT Test

Comparing the amplitudes of shots 5 and 6 (Figure 2-13) gives results that are the same to within 1 dB, once the effect of the different mass of explosive has been discounted. Comparing the amplitudes of shots 1, 7, and 8 in Figure 2-13 gives agreement to within 2 dB on hydrophone 29 but hydrophone 23 shows a total spread of 8 dB in amplitude. The results for shot 5 will be used to represent shots 5 and 6. Shot 7 gives the median result for shots 1, 7, and 8 and will be used to represent that site.

Chapter 3. Refracted Arrival Waveforms

Arrival waveforms are the sum of the pressure changes at the hydrophone over a period of time in response to a transmitted signal. This chapter uses simple models to illustrate how arrival waveforms are affected by the sound speed profile, source depth, and undersea mountains. Undersea obstructions and off-axis sources reduce signal duration by causing dead bands in time at the start and end of the arrival waveform respectively. At the end of the chapter, a comparison of some of the waveforms received at Ascension with a more complex model will show that the depth of the source accounts for some of the changes in arrival waveshapes.

For the models in this chapter, it is assumed that rays striking the bottom or surface are absorbed. This is an unrealistic assumption for uneven terrain over shorter distances, but it simplifies the modelling and will clarify the difference between refracted and reflected rays. Reflected rays will be addressed in a later section.

Chapter 2 showed that there are pronounced differences between the recorded arrival waveforms for different shots and that the sources were at different depths. In this chapter, the changes resulting from shots at different depths in deep water will be illustrated by modelling. To keep the ray trace model simple, a simple source waveform and a range of 150 kilometres will be used.

3.1. Deep water sound speed profile

The way in which sound propagates in the ocean (neglecting reflections at the boundaries) is determined by the speed of sound in water. Sound speed in the ocean usually changes over a short scale with depth and over a much larger scale with horizontal distance. The sound speed for an area can be characterised by an average sound speed profile, that is, sound speed plotted against depth. For the ATOC-FACT area, the sound speed profile does change between the source and receiver areas, but the change is small. As stated in the introduction, the approach will be to start with the simplest models and make them more complex when required. The SSP at Ascension is a good average for most of the path and will be used as the SSP for the whole path. This assumption of range invariance allows the use of the normal mode model and simplifies the calculations for the ray-trace model.

3. Refracted Arrival Waveforms

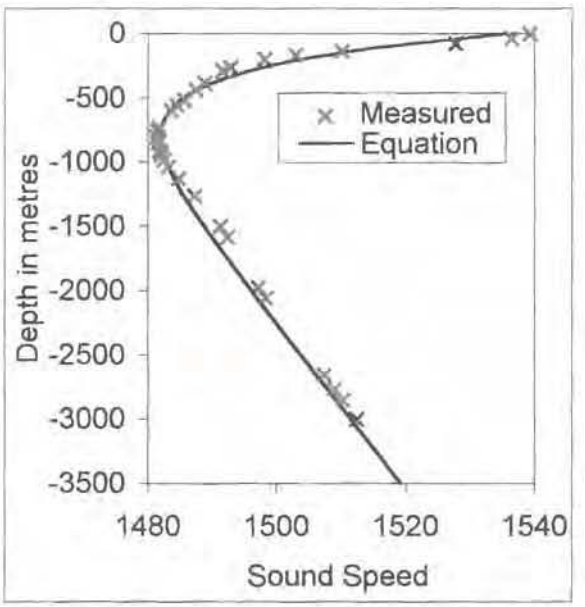

Figure 3-1 The sound speed profile at Ascension Island

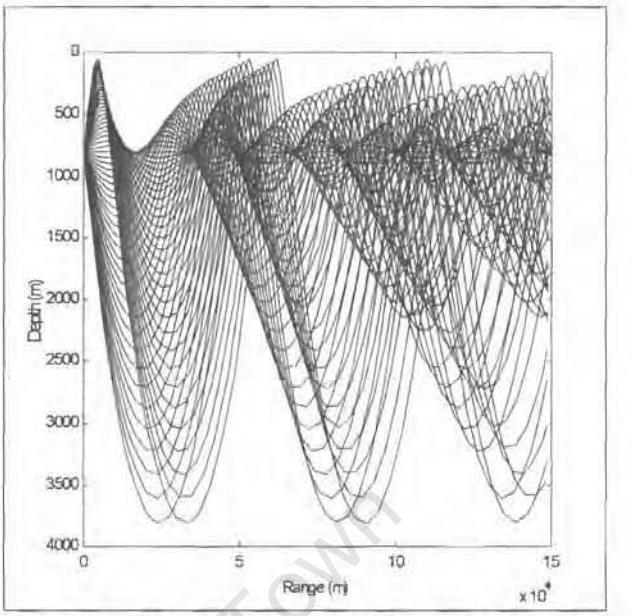

Figure 3-3 Ray-trace model for 150 km.

The sound speed profile at Ascension is shown in Figure 3-1 together with the canonical profile fitted to the point values. The Munk canonical profile equation (Munk, 1974; Munk and Wunsch, 1978; Munk *et al.*, 1995) and the values assigned for fitting the Ascension profile are given below:

$$c(z) = c_0 \left[1 + \frac{h\gamma}{2} \left(e^{2\frac{z - z_A}{h}} - 2\frac{z - z_A}{h} - 1 \right) \right] \quad \text{Equation 3-1}$$

where

c(z) is the sound speed in meters per second,

z is the depth in metres,

c_0 is the axial sound speed (1482 meters per second),

h is the buoyancy scale (576 metres),

γ is the adiabatic temperature gradient ($1.04167 * 10^{-5}$ m^{-1}),

z_A is the axial sound speed (1482 m/s),

The Munk equation for the sound speed profile will be used in both a ray trace and a normal mode model to show the effect of source depth and undersea obstructions.

3. Refracted Arrival Waveforms

3.2. Ray trace modelling

Ray tracing is an intuitive method that gives good results in most cases. It is generally the first model applied to an acoustic transmission problem and more complex models are only used if ray tracing proves inadequate. It unfortunately does not give true results in areas where there is no direct path, that is, ray tracing predicts zero intensity in shadow zones where, in practice, a signal may be present. In addition, it can predict unrealistically high intensities in areas where rays converge and cross. The ray tracing results shown here were obtained with the Bowlin "Ray" program (Bowlin, 1994) and with modifications of a simple ray code in Matlab (Porter, 1994).

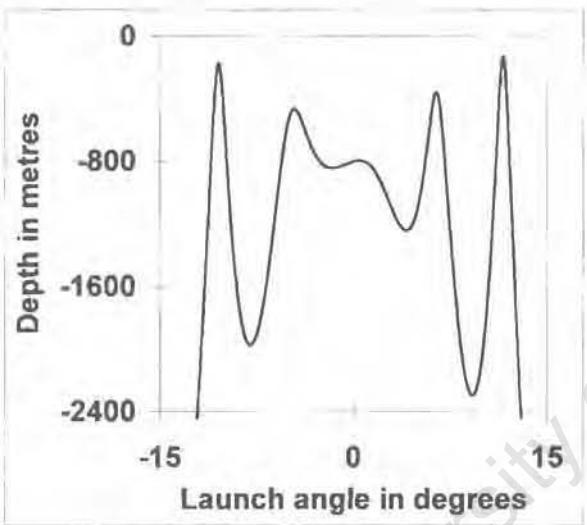

Figure 3-5 Ray termination depth vs. launch angle.

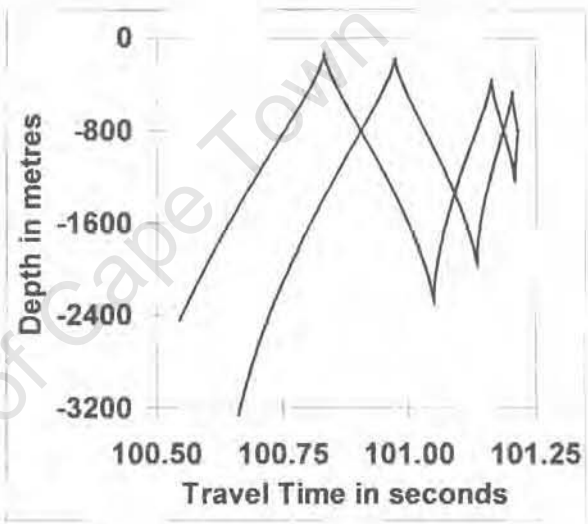

Figure 3-7 Ray arrival timefront

3.3. Axial source

Figure 3-2 shows the paths traced by selected rays over 150 km. This type of graph gives a good picture of the source to receiver relationship, but for longer ranges it contains a great deal of repetition. An alternative, summary view of an input-output relationship given in Figure 3-3, shows the depth of the ray at the termination range as a function of launch angle. Another summary view, focusing on the characteristics at the receiver, is shown in Figure 3-4. This summary view is called the timefront and shows the ray termination depth plotted against the travel time of the signal. This graph is particularly useful in constructing arrival waveforms.

3. Refracted Arrival Waveforms

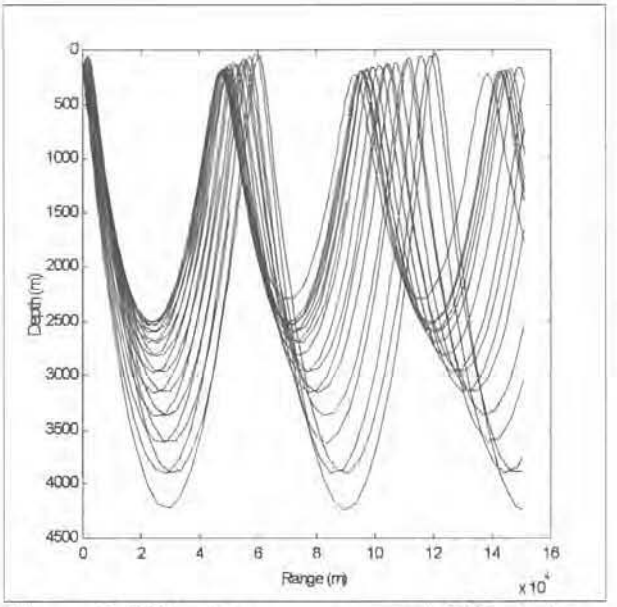

Figure 3-9 Ray trace – source at 200 metres.

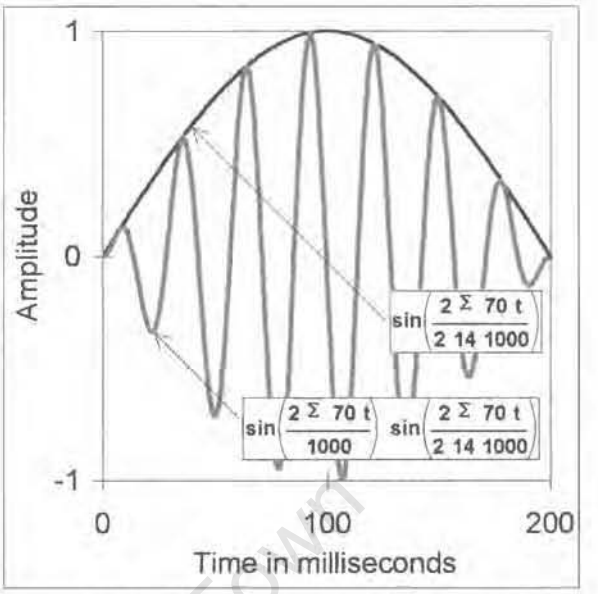

Figure 3-11 The source signal for simulating arrival waveforms at 150 km.

Figures 3-2 to 3-4 are derived from the ray trace model and illustrate some of the properties of deep-water transmission:

- The rays with smaller launch angles stay closer to the sound speed axis, travel slower, and arrive later.
- Conversely, rays with larger launch angles have turning points farther away from the sound axis, travel faster, and arrive earlier.
- For equally spaced launch angles, the density of rays is greatest close to the axis.
- Figure 3-4 shows that a receiver on the axis of the sound channel will intercept the slower, later arrivals (the rays with smallest launch angle). If the receiver is moved off the axis, the rays launched with smaller angles are not intercepted. Stated in terms of arrival times, this means that off-axis receivers do not receive the later signals.

The reciprocity theorem applies to the last point. Very simply, the reciprocity theorem states that the transmitter and receiver can be interchanged without affecting the received energy. This means, for instance, that the results are the same regardless of whether an off-axis receiver is used with an axial source or the receiver is off-axis and the source is axial.

It follows from the points above (and Figure 3-4) that the first arrivals are widely spaced in time while the later arrivals are increasingly closely clustered. This increasing density of rays resulting in a peak with an abrupt termination (corresponding to the arrival of the slowest energy travelling close to the sound channel axis) is often called the "SOFAR crescendo".

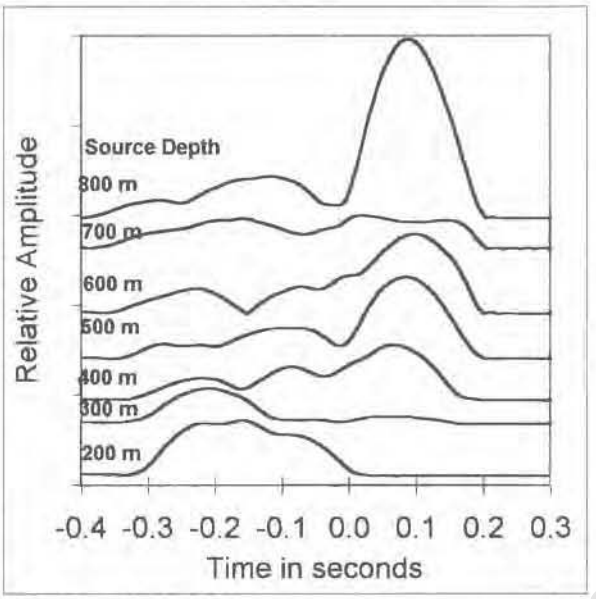

Figure 3-13 Effect of source depth on the shape of the received signal.

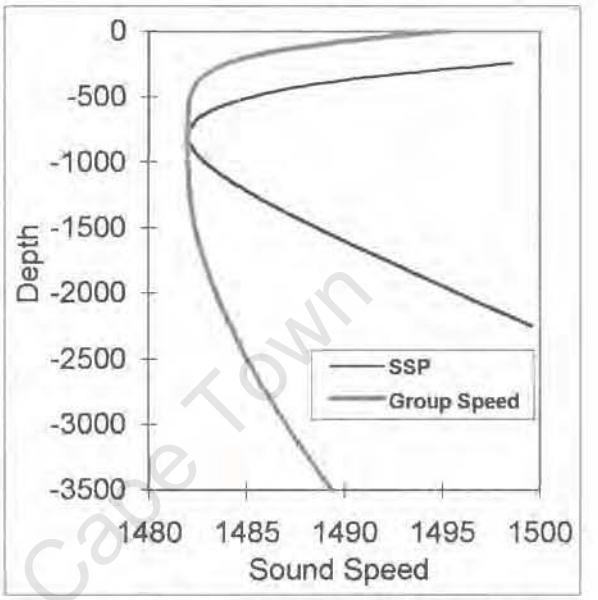

Figure 3-15 Sound speed profile and group speed for Ascension.

3.4. Trapped energy

An inherent feature of the model is that rays with small launch angles are trapped in the sound channel. Rays with launch angles of greater than about 12 degrees (for this SSP) escape from the channel and are reflected and absorbed at the surface and bottom. If the sound speed profile were to change gradually, either by varying the depth of the axis or by compression or expansion of the channel depth, the rays would still be trapped in the new channel, except for losses at the extreme angles.

3.5. Source off the sound axis – raytrace model

The way in which the sound rays travel can be further illustrated by considering a source above the axis at a depth of 200 metres. Figure 3-5 shows that the rays for the off-axis source are simply a selection of the rays shown previously in Figure 3-2. The rays with upper vertices deeper than the source are missing in Figure 3-5, creating a dead band around the sound channel axis, in which there are no turning points. This means that the rays closer to the axis (later arrivals) are missing, causing the final peak in the arrival waveform to be truncated.

3.6. Arrival waveforms modelled at 150 km.

Figure 3-6 (grey trace) shows the source waveform to be used in a model calculating arrival waveforms for a 150 km path. The upper trace (black) is the positive envelope of the signal. The positive envelope is a convenient and compact way of showing signal shape and will be used for the arrival waveforms. The way in which the energy at the trailing edge of the signal is progressively attenuated with the source farther off-axis is shown in Figure 3-7. The zero point on the time scale of Figure 3-7 represents the instant when the start of the axial signal arrives at the receiver. The 200 milliseconds of signal after this is the duration of the source signal. The signals in Figure 3-7 were synthesised using the normal mode model. This model will be discussed in a later section of this chapter.

3.7. Delay as a function of turning point depth.

It is clear from the discussion above, that rays with deeper turning points travel more rapidly and form the early part of the arrival waveform. This relationship between turning point depth and arrival time for the canonical sound speed is quantified in the equations below. Equations 3-2 and 3-3 define group slowness (the reciprocal of group speed) as a function of the sound slowness at the ray turning point depth. These equations are from page 108 and 109 of Munk, *et al.*, (1995).

$$s_g(z) := S_A \cdot \left[1 - \gamma \cdot h \cdot \frac{\frac{\phi_P(z)^4}{48}}{1 + \frac{\phi_P(z)^2}{12}} \right] \quad \text{.....Equation 3-2}$$

where

$$\phi_P(z) := \sqrt{\frac{1}{(\gamma \cdot h)} \left(\frac{S_A^2 - S_P(z)^2}{S_A^2} \right)} \quad \text{.....Equation 3-3}$$

Figure 3-8 shows the sound speed profile and the group speed calculated using the equations above. In this context, the group speed is simply the average speed of energy with a particular turning point depth. Since the energy has to transit through regions of lower sound speed it follows that the group speed has to be slower than the turning point speed, except for the limiting case of the axial ray when the turning point is on the axis. Once the group speed has been calculated, the delay is obtained by dividing the group speed by

range, as has been done for Figure 3-9. The arrival time of the axial ray is used as the reference on the time axis.

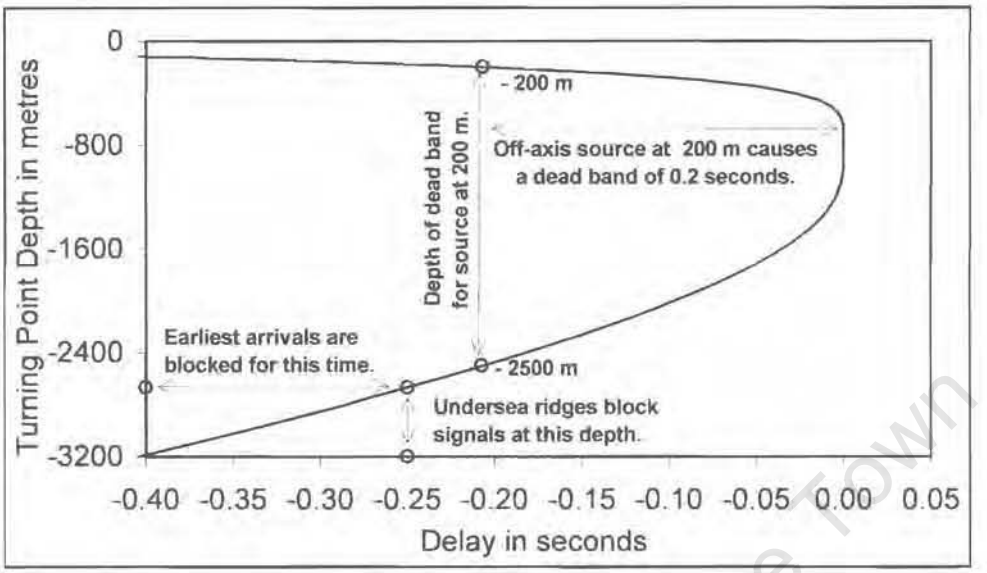

Figure 3-17 The relationship between depth and delay.

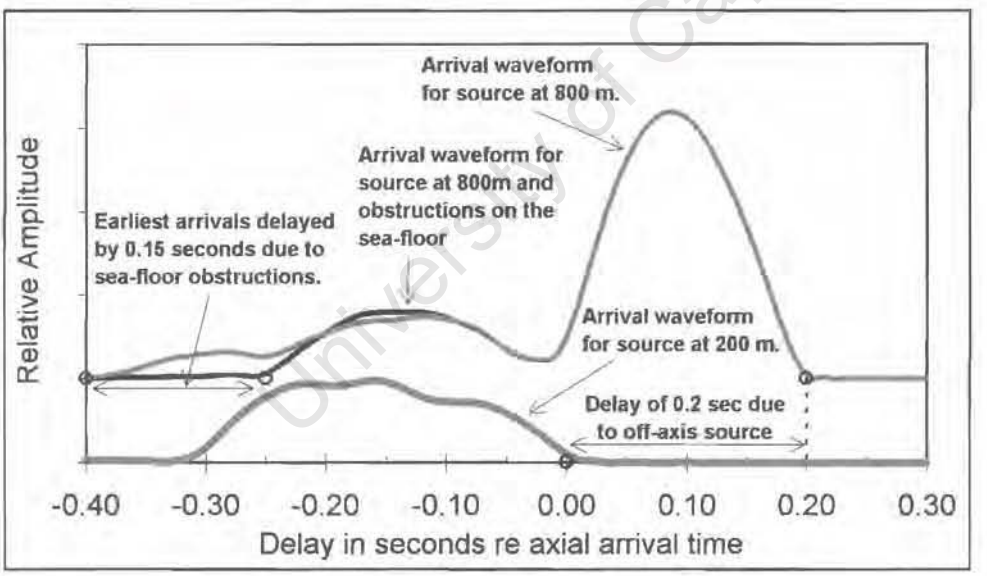

Figure 3-19 Effects of off-axis source and sea-floor obstructions.

Figure 3-9 shows that an off-axis source will have a dead band in depth, that is, a range of depth above and below the axis in which there are no turning points. At the receiver, this depth range is converted into an equivalent dead band in time of arrival. The dead band depth extends from the shallow source through the sound channel axis down to the source sound speed profile conjugate depth. (The SSP conjugate depth is the depth of the closest turning point of the ray on the opposite side of the sound channel axis.) In Figure 3-9 the source depth is - 200 metres and the conjugate depth is - 2500 metres. The time dead band

extends from the arrival time of the slowest rays of the off-axis source to the arrival time of the axial arrivals. An example of the arrival waveforms is shown in Figure 3-10.

Figures 3-9 and 3-10 also show the effect of undersea ridges or mountains that obstruct the deepest (fastest) rays. This results in a shorter arrival waveform, as for the off-axis source, but with the start, not the end, of the waveform being truncated.

3.8. Normal mode modelling

Normal mode theory describes sound propagation as the transmission of acoustic energy by a number of modes. If the sound speed is range-independent and a function only of depth, the modes travel at different group speeds. Each mode carries a replica of the source waveform. The arrival waveform is the sum, over time, of the modes, as can be seen from Equation 2-4, from Jensen *et al.*, (1994). (The mode coefficients, ψ, alternate in sign, so the summation is like a successive approximation.)

The equation describing the composition of the arrival waveform is:

$$S_t = \text{icfft}\left[S_f \, e^{1j\cdot\frac{\pi}{4}} \cdot \sum_{m=1}^{n} \left(\psi s_{m,f} \, \psi r_{m,f}\right) \cdot \sqrt{\frac{2\cdot\pi}{k_{m,f}\, r}} \cdot e^{1j\cdot k_{m,f}\, r} \right] \quad \text{..... Equation 3-4}$$

where

S_t = signal in time domain (received)

S_f = signal in frequency domain (transmitted)

$k_{m,f}$ = horizontal wavenumber (eigenvalue) as a function of mode and frequency

m = mode number

n = highest mode number of interest

f = frequency

ψs = eigenfunction value at source as a function of mode and frequency

ψr = eigenfunction value at receiver as a function of mode and frequency

r = range

icfft = inverse complex fast Fourier transform

The 1/r term for attenuation of amplitude with range has been deliberately omitted in this equation. The eigenfunction values for source and receiver in the equation can be inter-changed without changing the output signal, as predicted by the reciprocity theorem.

3. Refracted Arrival Waveforms

Figure 3-11 shows the intensity patterns of the first, sixth and thirtieth modes calculated for a frequency of 70 Hz. Higher modes extend farther above and below the acoustic axis. It follows that the lowest mode has the lowest speed and that the propagation speed increases for the higher modes. In the raytrace model the ray reaches maximum velocity at the turning point of the ray. The equivalent turning point in the normal mode model is the depth at which the mode standing wave starts to decay exponentially. (More precisely, in the WKB approximation to the modal solution, the turning point is at the depth where the vertical wavenumber, k_z, is zero. (Jensen, *et al.*, 1994, p. 292-293)) As an example, the upper and lower turning points of the first mode in Figure 3-11 are at 450 and 1200 metres, respectively. This corresponds to the turning point of a ray with a launch angle of 4.8 degrees.

The influence of source depth (in the ψs term) in Equation 2-4 is shown in Figure 3-12 where the amplitude of the field at various depths is plotted for sources at 200 and 800 metre depths. The amplitude plotted in Figure 3-12 is the sum of the first 49 modes. Since the first mode is a maximum at 800 metres, the on-axis (800 metre) amplitude is greater than the off-axis amplitude. The amplitude of all modes must be zero at the sea surface so the amplitude tends to get less as the depth of the source is reduced above 800 metres.

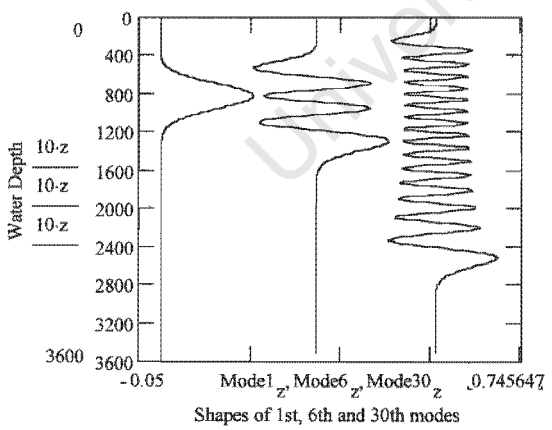

Figure 3-21 Mode amplitude patterns.

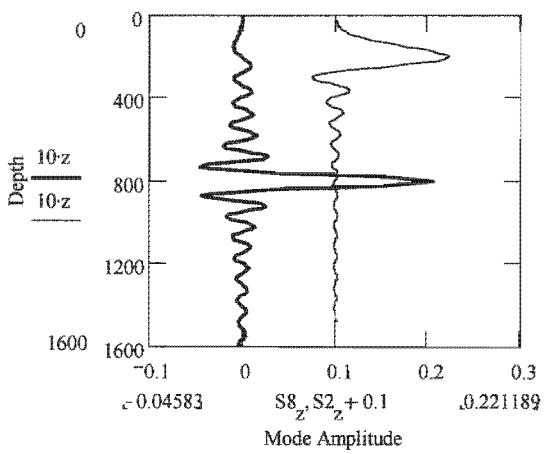

Figure 3-23 Receiver amplitudes for on-, and off-axis sources.

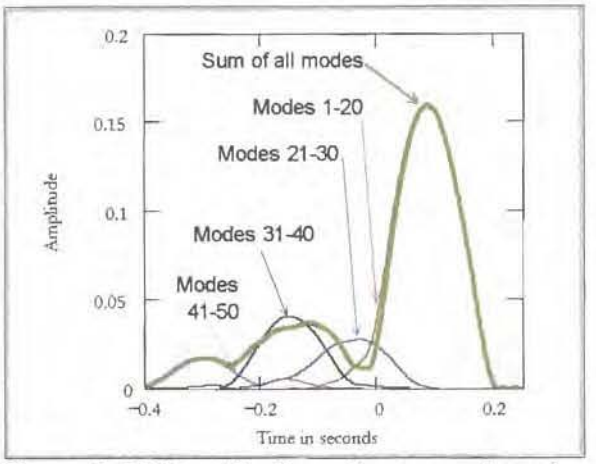

Figure 3-25 Contribution of groups of modes – source on-axis.

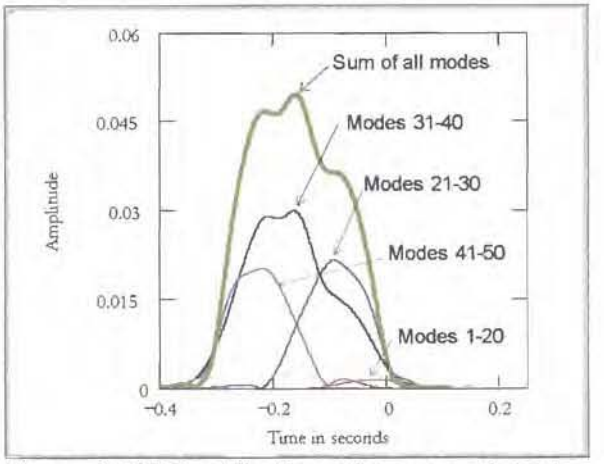

Figure 3-27 Contribution of groups of modes – source off-axis.

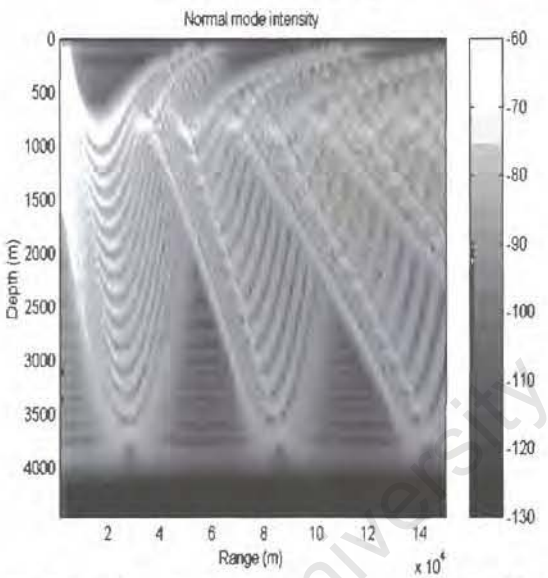

Figure 3-29 Mode intensity – Source at 800m

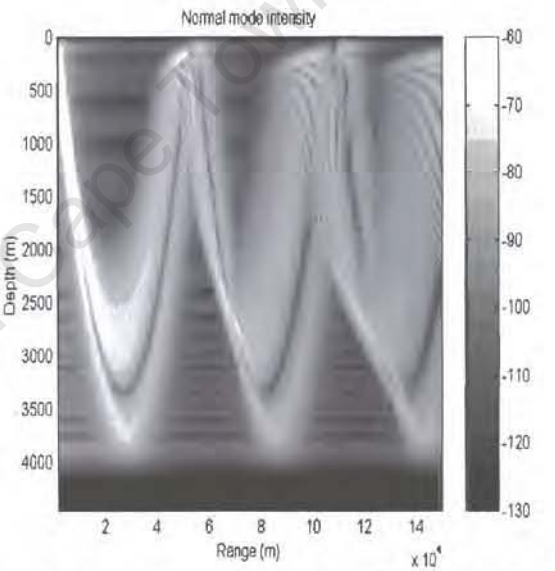

Figure 3-31 Mode intensity – Source at 200 metres

An important difference between the raytrace and normal mode models is that the normal mode model accounts for the frequency of the waveform, whereas the raytrace model assumes a high frequency. The shape of the mode is affected by the frequency; the longer the wavelength, the farther the mode will extend above and below the sound axis. It follows that the normal mode model exhibits both modal and frequency dispersion – the higher modes and longer wavelengths travel faster.

3.9. Mode arrival times – normal mode model

Applying the normal mode model to the example used for the ray-trace model above and taking the envelope of the source signal to be a half sine with duration 200 milliseconds, as

shown in Figure 3-6, gives the arrival wave-shapes shown in Figure 3-13. The positive half of the signal envelope is shown together with the sum of groups of modes. The largest amplitudes are associated with the lowest modes (in Equation 2-4 the wavenumber k is larger for the lower values of m) and the lower modes are the last to arrive.

Figure 3-14 is similar to Figure 3-13, but shows the mode amplitudes and timing for an off-axis source. The amplitudes of the lower modes are reduced and the prominent peak and sharp termination (the SOFAR crescendo) of the signal is missing. Note that the amplitudes of the off-axis source are much smaller than that of the axial source.

3.10. Ray - mode duality

Figures 3-15 and 3-16 are plots of sound intensity calculated with a modified normal mode example (Porter, 1994) for an on-axis and off-axis source respectively. Correspondence between ray-trace paths and normal mode model intensities can be seen in the comparison of Figures 3-2 and 3-15. Figures 3-5 and 3-16 make a similar comparison but for an off-axis source. Rays can be visualised as being the arithmetic sum of modes; modes can be visualised as being the sum of rays. Figures 3-15 and 3-16 illustrate the effect of summing mode energy. Arrival waveforms are examples of the summing of both rays and modes over time.

3.11. Modelling limitations and extensions

Amplitudes for ray trace modelling: The simplest implementation of the ray trace equations does not provide a means of assessing ray amplitude. The amplitude can, however, be estimated by utilising the concept of a ray tube, where the tube is defined by the width between adjacent rays. The amplitude of the ray is inversely proportional to the area of the tube. A comparison with the area of a tube for spherical spreading yields absolute amplitude. Examples of uses of this extension are:

- *Dynamic Ray Tracing* adds two further equations to the basic ray tracing model to keep track of the area of the tube (Bold and Birdsall, 1986, Jensen *et al.*, 1994.).
- *Gaussian Beam Tracing* associates a Gaussian intensity distribution with each ray. This results in a blurring or shading of amplitudes that is closer to the results given by modal models.
- The amplitude of rays traced by simple code can be estimated at a point by tracing the adjacent rays and estimating the area of the tube from the separation of the

endpoints. (In two-dimensional models, this simplifies to estimating the height of the tube.) This is the technique used by the Bowlin ray trace model for producing various results in this document.

Ray chaos in ray trace modelling: Some initial conditions in range-dependent environments can lead to rays, initially close together, diverging exponentially from each other. This condition also results in an exponential increase in the number of eigenrays between these launch angles at long ranges. This extreme sensitivity to initial conditions can also result in different reverse tracks when traced by a finite precision computer. At long ranges, the density of these rays can become so high that the ray chaos can be described as "saturated" and a "predictability horizon" is encountered. Beyond the predictability horizon, signals are unpredictable in the sense that a summation of the eigenrays can be quite unlike the real signal (Tappert and Tang, 1996, Spiesberger and Tappert, 1996, Wolfson and Tappert, 2000.). This is a serious problem in range-dependent ray trace modelling since there is no remedy apart from using different initial conditions or using full-wave models.

Normal mode model range-dependence: The normal mode model is theoretically an exact solution to the wave equation – provided that an infinite number of modes is summed and that there is no variation in conditions with increasing range. In practice, the accurate calculation of the figures for a sufficient number of modes can be problematical. Also, real-ocean conditions approaching range-invariance are not often encountered.

Other full-wave models: Other full-wave models (such as the parabolic equation model) are limited in their applicability by the assumptions made in deriving the solution to the wave equation. At best, the models can only be said to be weakly range-dependent and are unlikely to give good results in the area considered here.

3.12. Comparing models and recordings of selected shots at 4.4 Megametres

A normal mode prediction of the arrival waveshapes at 4.4 Megametres for sources at various distances off the sound channel axis is shown in Figure 3-17. The calculation of the model is similar to that of the normal mode model for 150 kilometres, except that a more complex waveform was used to simulate the explosive source. This calculation is shown in the appendix. Comparing Figure 3-17 with Figure 3-7, the duration of the arrival waveform is greater, but the same pattern of a reduction in the peak amplitude as the source moves farther off-axis is evident.

3. Refracted Arrival Waveforms

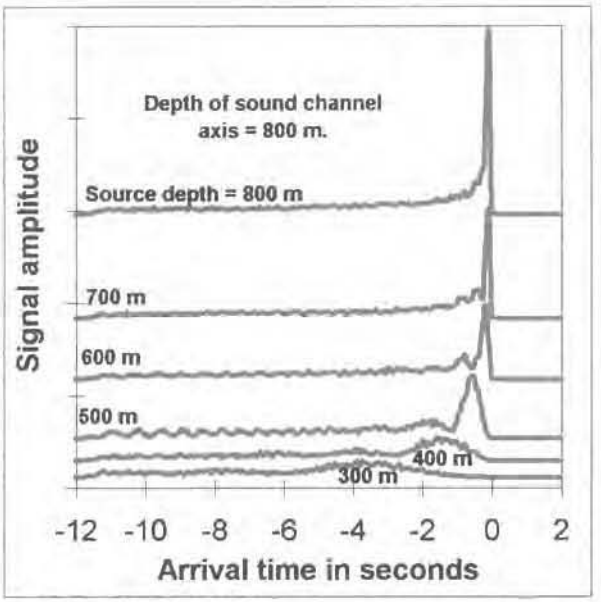

Figure 3-33 Normal mode synthesised arrival waveforms

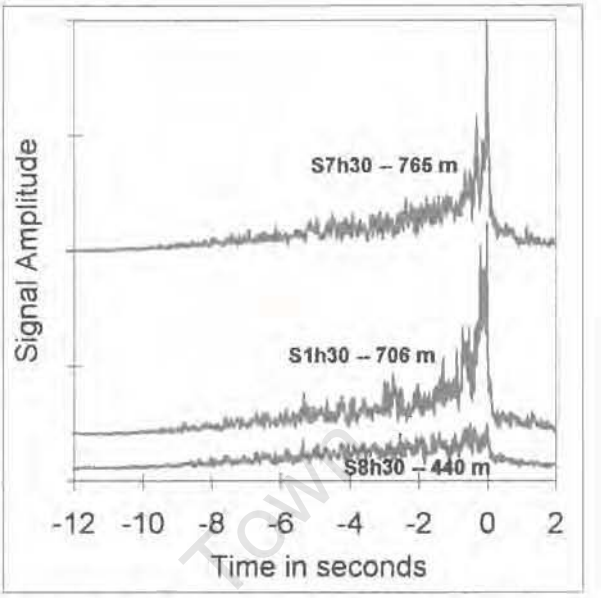

Figure 3-35 Recorded arrival waveforms for shots 7, 8 and 1

As stated in Chapter 2 under the heading of source differences, shots 7, 1, and 8 have a common path and differences in shape must be due to differences at the source. It was also shown (Table 2-1) that the shots occurred at different depths. It should now be possible to compare these shots to the prediction by using Figure 3-17. For this comparison, Figure 3-18 shows the envelopes of the selected best recordings for each of shots 7, 1, and 8. The amplitudes have been adjusted to account for the different mass of explosive charge per shot so that peak values in the graph can be compared. The best estimate of the depth of the source is indicated on each trace. Figures 3-17 and 3-18 are each normalised to the largest peak in the figure so that the amplitudes between the figures cannot be compared, but only the shapes.

The shapes of shots 7, 1 and 8 appear to fit with the predicted pattern of reducing amplitude with increasing distance off-axis, insofar as it is possible to judge with just three shots of which the first two are close in depth. A more precise comparison will be done in a later chapter. However, the shape of the waveform before the peak is not a good match. This is a sign of reality being more complex than the simple model. Some of this complexity will be explored in later chapters.

Chapter 4. Topographical Interference And Signal Amplitudes

In this chapter the relative signal amplitudes at the hydrophones are compared with the extent to which the signal path is obscured. Some different views of the undersea topography are presented and the more obvious interference effects identified. The peak amplitudes of the different hydrophones for a single shot are compared, that is, the differences between sources are suppressed for this comparison. The maps in this section are based on data from the GEBCO (General Bathymetric Chart of the Oceans) Digital Atlas on CD-ROM and from the map "NRL 1989: Bathymetry of the South Atlantic Ocean". To form an effective picture of the whole area and of the much smaller areas where interference occurs, different types of synoptic and zoomed-in views of critical areas are shown. The first views are contour maps of the shallower areas where interference occurs. The signal tracks were calculated as great circles rather than geodesics, since the difference in results is too small to affect the results shown in this chapter.

4.1. Contour maps

Figure 4-1 shows the first obstacle on the path, Walvis ridge, and the tracks to the extreme southwestern and northeastern hydrophones for each source site. For example, the tracks for S5 to h23 and s5 to h29 (S5h23 and S5h29) are shown at the northeast end and those for S2h23 and S2h29 at the southwest end. Tracks for S6 are not shown since they would be nearly identical to those of S5. The depth of the ridge under the tracks varies from about 1500 metres at the northeast end to about 3000 metres near the southwest end. Although Walvis ridge must obviously interfere with the signals, it does not appear to affect the relative amplitudes considered in this chapter. The complex reflections off the ridge will be considered in Chapter 5.

The next area with underwater peaks is near St Helena (Figure 4-2). Seamount Bonaparte intercepts the signals from S1 and S4 to hydrophone 23. The sources farther away from centre, such as S2 and S3 to the southwest and S5 to the northeast are not blocked.

4. Topographical Interference And Signal Amplitudes

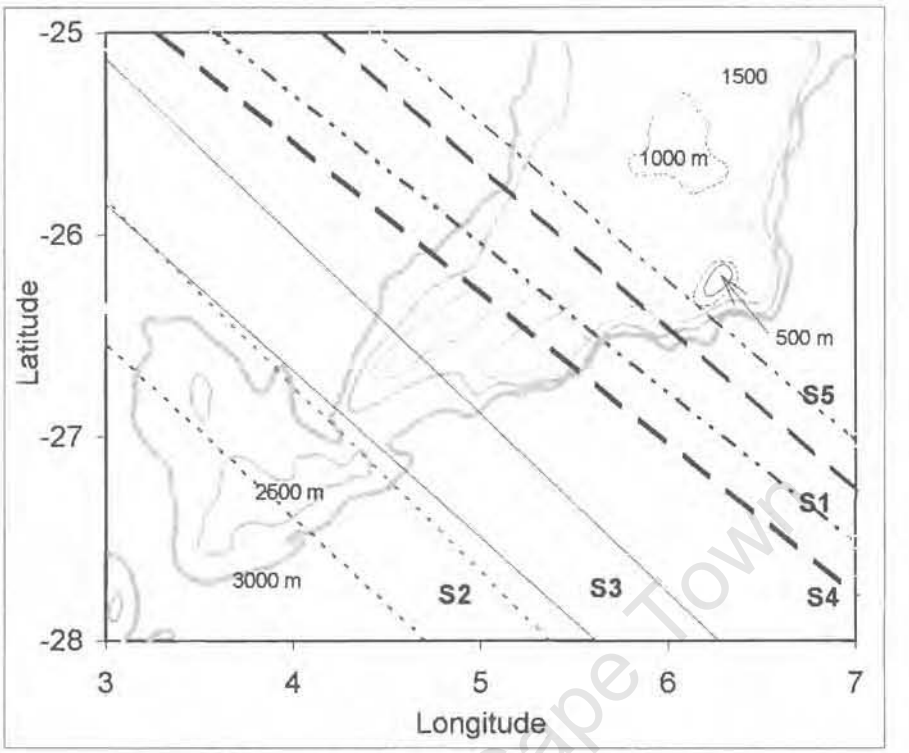

Figure 4-1 Shot track margins over Walvis ridge.

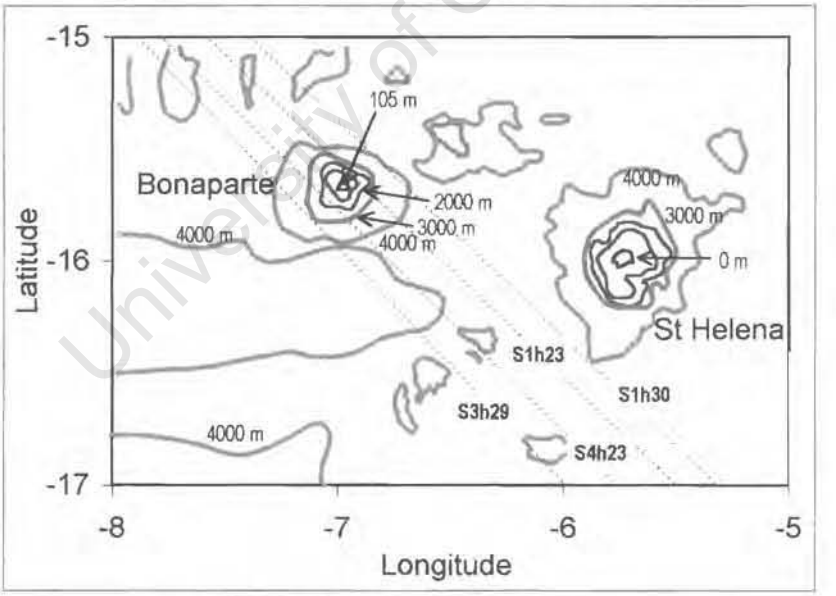

Figure 4-3 Signal paths at St Helena.

The final shallow area at seamount Grattan, close to Ascension Island, is shown in Figure 4-3. This peak intercepts a number of the tracks. The outermost tracks, such as S2h23 and S1h29 are not obstructed while the innermost tracks such as S2h30 and S1h23 are blocked by a peak reaching almost to the surface (72 metres).

4. Topographical Interference And Signal Amplitudes

In summary, the paths of the signals from the more southwesterly shots such as S2 are not blocked on the way to the more southwesterly hydrophone, h23. Similarly, the tracks from the northeasterly shots, such as S1, are not blocked on the way to the northeasterly hydrophones, h30 and h29. Tracks crossing from northeasterly shots to southwesterly hydrophone are intercepted by Grattan. Similarly, the tracks crossing from southwesterly hydrophones to northeasterly hydrophones are intercepted. Seamount Bonaparte blocks some rays from shot S4 and S7 while allowing rays from the outer shots to pass.

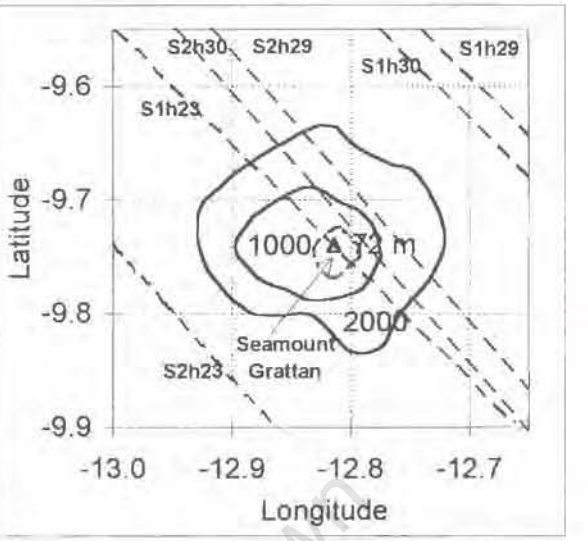

Figure 4-5 Signal paths at Seamount Grattan

4.2. Profiles

Along-track profiles give a different perspective. Figures 4-4 to 4-8 show the deep trough (5000 metres) on either side of Walvis ridge, the 4000-metre plateau at seamount Bonaparte, and the 3000-metre plateau from which seamount Grattan rises, just short of Ascension Island. These figures show that the topography is shallow enough to interfere with the signals only in a few small areas. In addition, a small change in the signal track can result in a very different profile, due to the small width of interfering seamounts such as Bonaparte and Grattan.

The profiles below are constructed using intersections with contour lines only. There is no interpolation between depths. This results in a somewhat crude graph and a loss of the information that is usually read implicitly (by interpolation) by the viewer of contour maps.

4. Topographical Interference And Signal Amplitudes

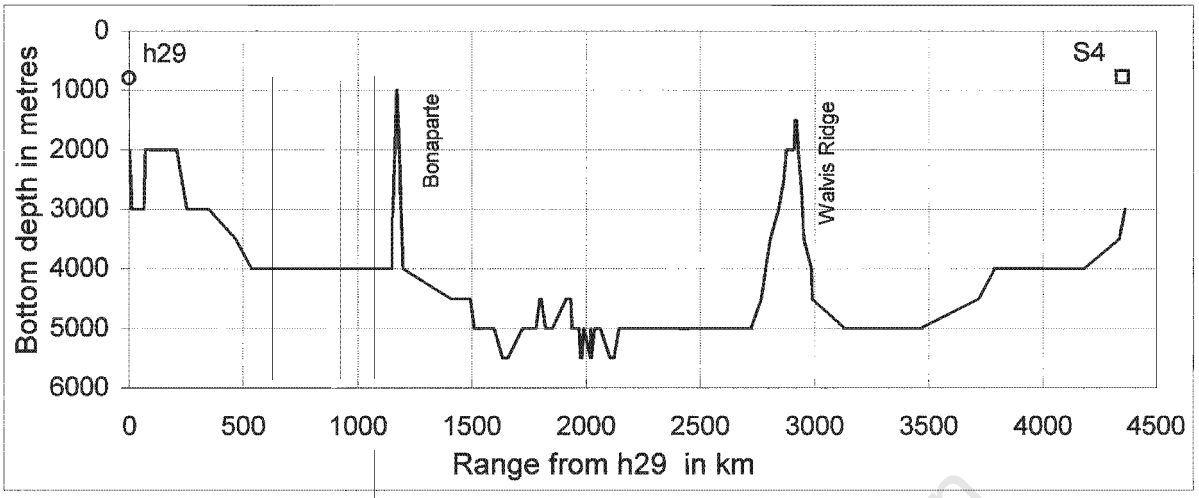

Figure 4-7 Track profile, S4 to h29.

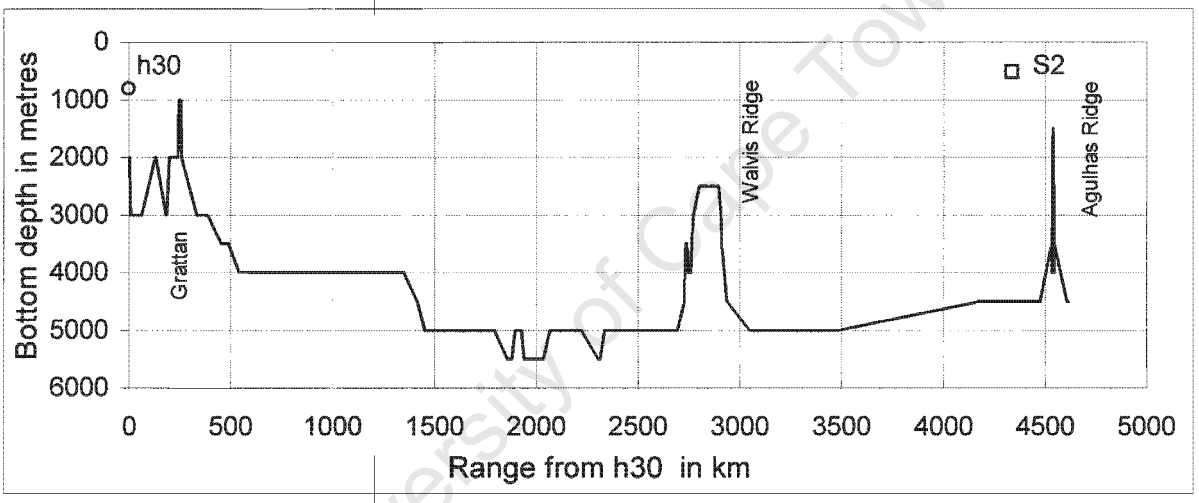

Figure 4-9 Track profile, S2 to h30.

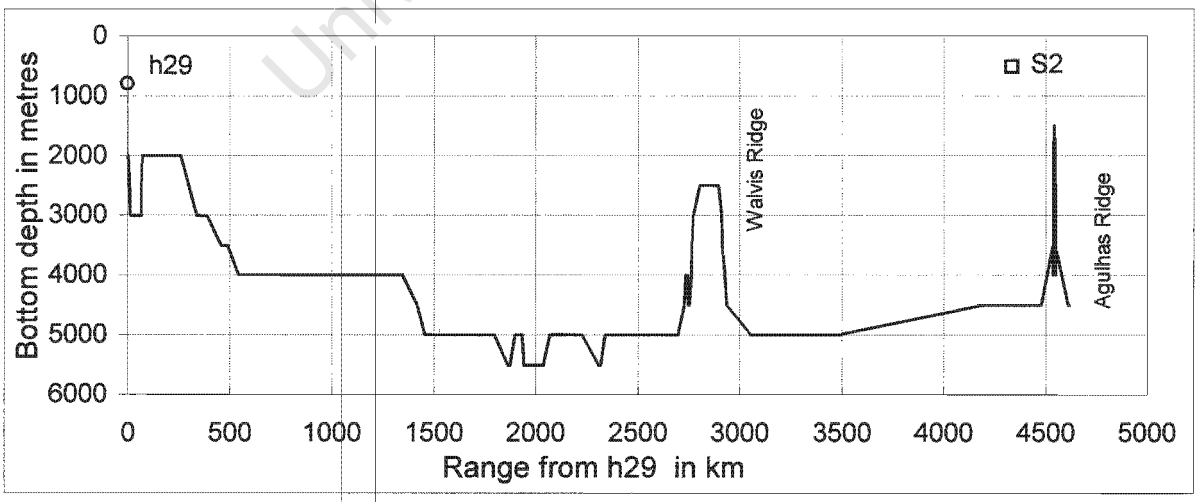

Figure 4-11 Track profile, S2 to h29.

4. Topographical Interference And Signal Amplitudes

The profile tracks show:

- The track from shot 4 to hydrophone 29 (Figure 4-4) crosses Walvis Ridge at a point where the sill is less than 2000 metres deep. Seamount Bonaparte blocks the path, while Grattan is clear.
- For the S2 to h30 track (Figure 4-5), Walvis ridge is about 2500 metres deep and sea-mount Grattan shows up as an obstruction.
- The shot 2 to hydrophone 29, (Figure 4-6) track misses Bonaparte and the Walvis ridge sill is relatively shallow. This view erroneously shows that the track misses Grattan, since the track does not intersect the 1000 metre contour, but it will be shown in a later view that there is some obstruction by Grattan.
- Bonaparte blocks the S4 to h23 track in Figure 4-7 while Grattan projects above the Ascension plateau. Here again, the way in which this view is constructed has resulted in the peak not being shown correctly, as will be shown in the azimuth view, Figure 4-11.
- The S7 to h23 (Figure 4-8) track is blocked by both Grattan and Bonaparte.

4.3. Azimuth views

Possibly the best summary view for understanding the complexity of the obstructions with changing tracks is the azimuth view, looking from the source towards the hydrophones. This is like looking along the great circle path between source and receiver with a narrow angle of visibility to either side of the track. Five views are presented here, one for each of the separated source sites. The figure for shot 5 is representative of both shots 5 and 6 and the figure for shot 7 is representative of shots 1, 7, and 8. As the point of view shifts from the most southwesterly shot (S2) to the most northeasterly shot (S5), the seamounts Bonaparte and Grattan move from the right of the receivers across to the left. Since Bonaparte is much closer to the sources than Grattan, it moves much more than Grattan does. As they move across, each of the hydrophones is obscured in turn by one or both of the seamounts. A graph comparing the relative signal strengths in decibel (dB) for each shot for the three hydrophones h23, h30 and h29 is included with each azimuth view in the following five figures. The graph of signal strength is normalised to the strongest signal.

4. Topographical Interference And Signal Amplitudes

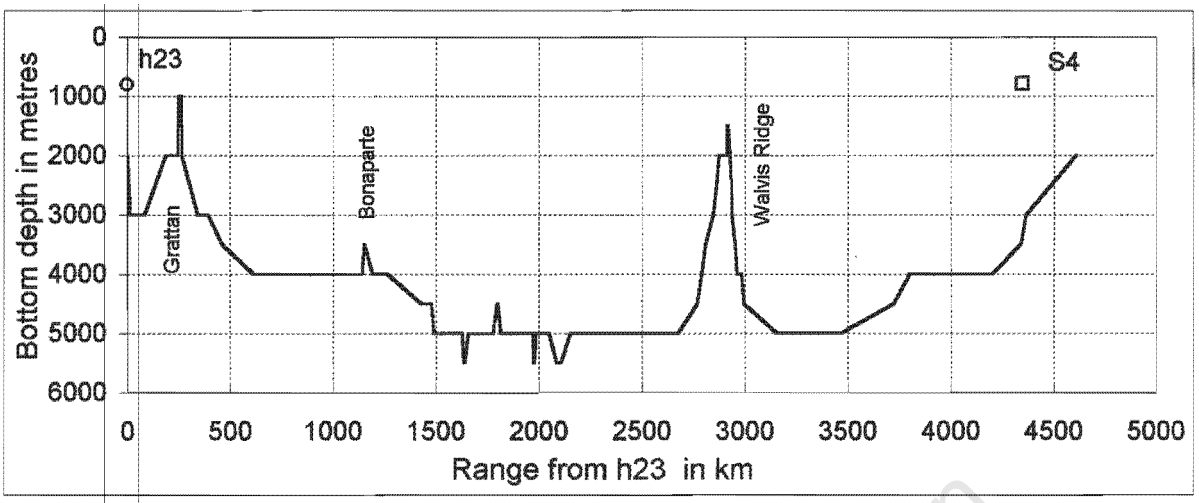

Figure 4-13 Track profile, S4 to h23.

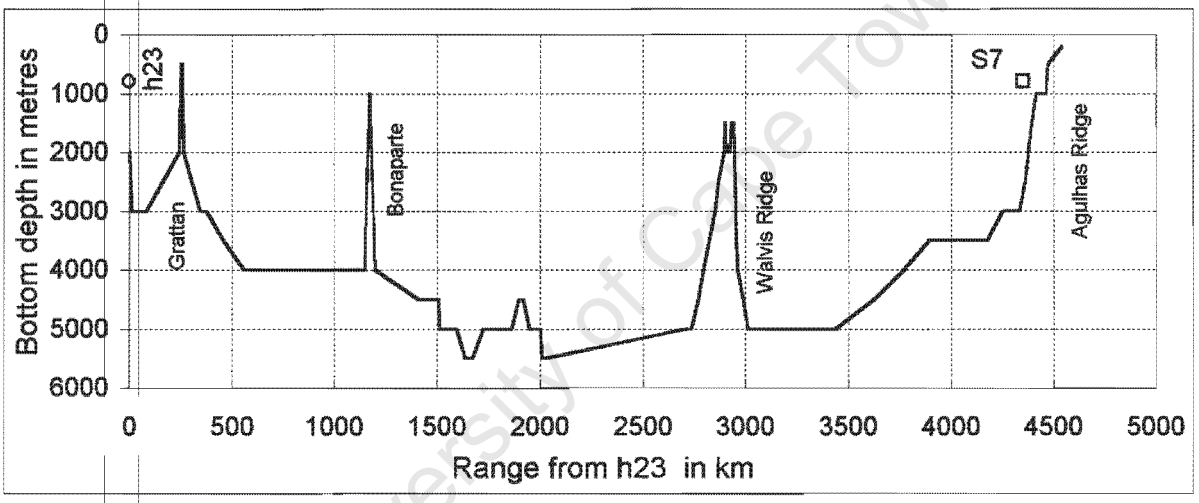

Figure 4-15 Track profile, S7 to h23.

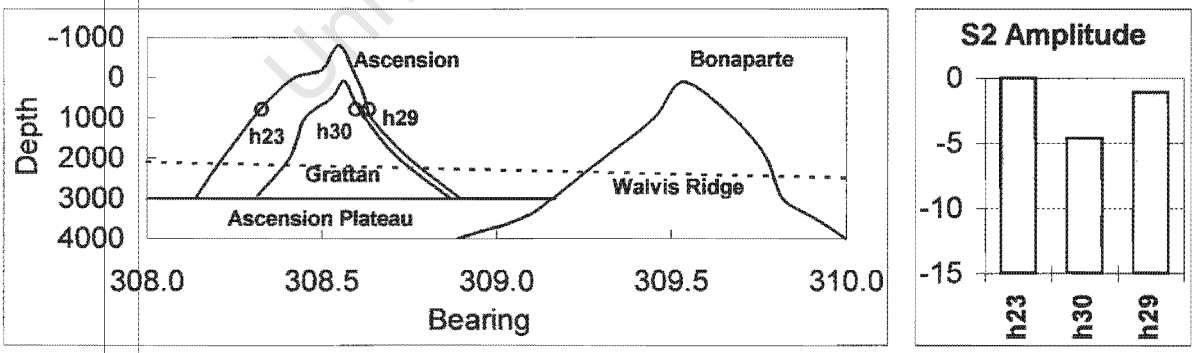

Figure 4-17 View and relative hydrophone amplitudes for S2

The outline of Ascension Island is included here for orientation only, since the hydrophones are closer than Ascension Island, and so it does not obscure any of the sources. Walvis ridge and the plateau in front of it are included for completeness but they do not affect the relative signal strengths at the hydrophones.

4. Topographical Interference And Signal Amplitudes

In Figure 4-9 (the first of the azimuth views, using S2 as source), the signal paths to hydrophones 23 and 29 are clear of obstructions while hydrophone 30 is just obscured by Seamount Grattan. The signal amplitudes agree with this picture, with hydrophone 23 receiving the largest signal. The signal path to hydrophone 29 is close to grazing but calculation shows it to be outside the horizontal diffraction zone (Munk *et al.*, 1988) where the amplitude could be increased or decreased by edge effects. The amplitudes of h29 and h23 appear to be nearly identical for S2 and S3 (Figure 4-10), confirming that the paths are clear. The signal reaching h30 is probably mainly by refracted rays passing over the slope above the intercept point.

For S3 in Figure 4-10, Grattan moves across the hydrophones, away from hydrophones 29 and 30, and closer to hydrophone 23. None of the three hydrophones is obstructed by the major topographical features mapped in the graph. The amplitude graph, however, indicates that there are probably minor features close to hydrophone 29 that slightly reduce the amplitude of the signals reaching it. (In the following graphs, hydrophone 29 always shows somewhat less signal than hydrophone 30 when they are apparently both unobstructed.) Hydrophone 30 is farthest from Ascension (closest to the source) and is the least likely to be obstructed by minor local features. The change in relative signal amplitudes from S2 to S3 is consistent with the change in path – clearing the path to hydrophone 30 results in increased signal at this hydrophone.

For S4 (Figure 4-11), the lines to all three hydrophones appear to be close to grazing. A closer analysis of the relative bearings from the grazing points to the source and receivers indicates that hydrophone 23 is obscured by Grattan and is outside the horizontal diffraction zone. Both hydrophones 29 and 30 are in the horizontal diffraction zone of Bonaparte with h29 just clear and h30 blocked. According to this, the amplitudes at both hydrophones 23 and 30 are larger than expected. However, for these lines the vertical obstruction of Napoleon and Grattan is so small that refracted rays over the obstructions probably reach h23 and h30. (It will be shown in Chapter 5 that the received signal from S4 is composed of rays some distance off the axis.)

4. Topographical Interference And Signal Amplitudes

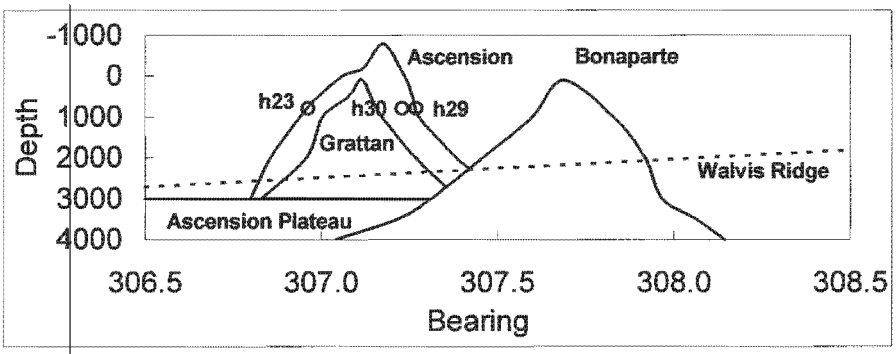

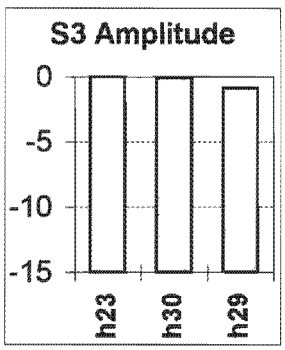

Figure 4-19 View and relative hydrophone amplitudes for S3

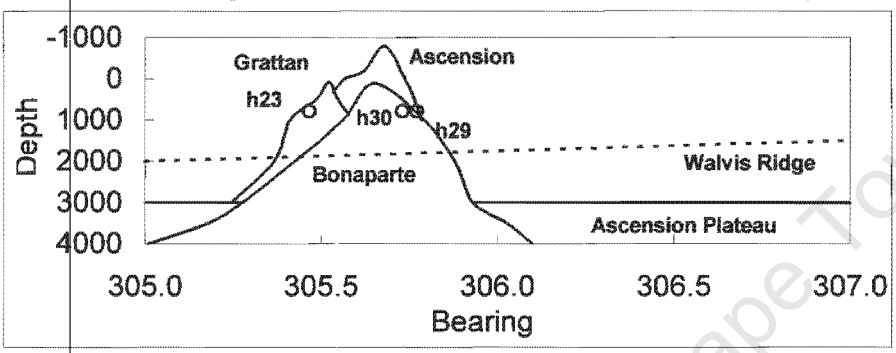

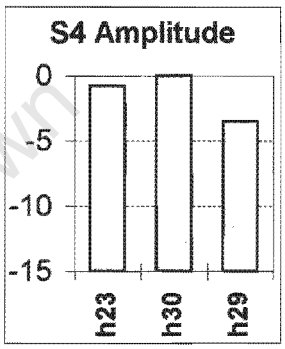

Figure 4-21 View and relative hydrophone amplitudes for S4

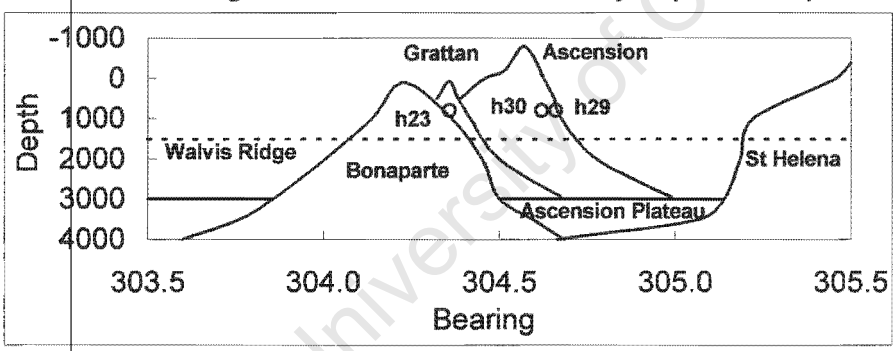

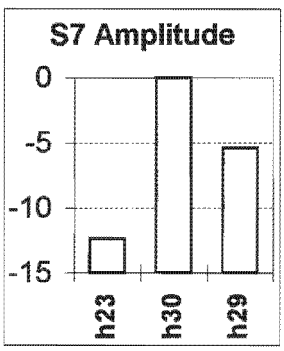

Figure 4-23 View and relative hydrophone amplitudes for S7

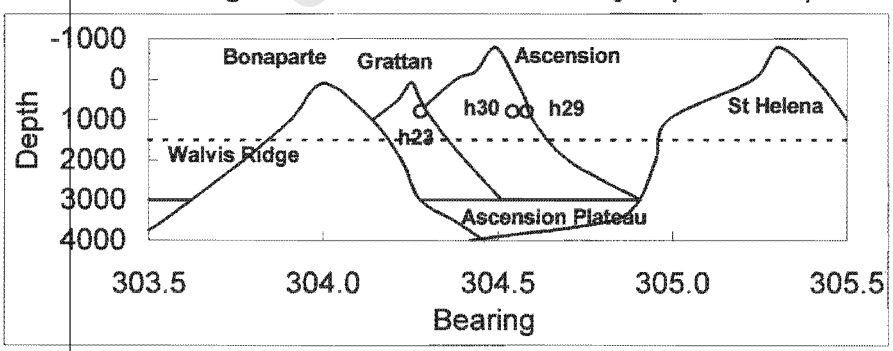

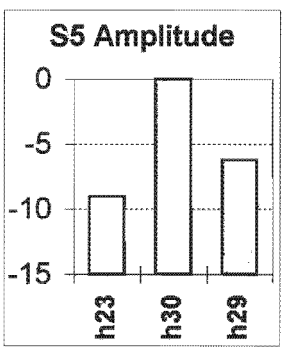

Figure 4-25 View and relative hydrophone amplitudes for S5

4. Topographical Interference And Signal Amplitudes

If the signal reaching h23 and h30 were composed largely of diffracted energy, one would expect the high frequencies to be more attenuated, since shorter wavelengths are more attenuated in diffracted energy. Comparing the spectra of S4 received at h23, h29 and h30 (Figure A-2 in the appendix) shows that the opposite is true – the high frequencies are larger in amplitudes for h23 and h30. This confirms that h23 and h30 are not obscured, contrary to the picture in Figure 4-11.

For S7 in Figure 4-12, the path to hydrophone 23 is obscured by both Bonaparte and Grattan, while the paths to hydrophones 30 and 29 are unobstructed. The amplitude of hydrophone 23 has decreased greatly, as would be expected.

For S5 (Figure 4-13), Seamount Bonaparte has moved off the track to hydrophone 23 but Seamount Grattan still blocks the path. Compared to the previous figure, the amplitude of the signal at hydrophone 23 shows a small increase while the amplitudes at hydrophones 30 and 29 maintain their relative amplitudes to within 1 dB.

The discussion in this chapter has assumed that the only difference between the signals received from the shot on different hydrophones is the amount of attenuation along the transmission path. A close look at Figure 2-9 shows that this is probably true only as a first order effect. There are minor differences in shape, such as the way in which shot 3 tails off on hydrophones 23, 29, and 30. The signal on hydrophone 23 shows more of a peak at the termination than that on hydrophone 30, which is again slightly more peaked than the signal on hydrophone 29. The same effect can also be seen on shot 4. It seems unlikely that this effect was caused by blocking topography along the path. It might be due to varying strength of reflections off local topography at the hydrophone. There is a similar but much larger effect on shots 1 and 7 where the signal peak on hydrophone 30 is far larger in proportion than that on hydrophone 29. This may be due to ocean variability.

This chapter has shown that there is good correlation between the obstruction caused by seamounts Bonaparte and Grattan and the relative signal attenuation at the hydrophones.

Chapter 5. Off-Axis Sources, Obstructions And Reflections

Chapter 3 showed that off-axis sources truncate the trailing edge, and sea-floor obstructions the leading edge, of the arrival waveform, thus forming a window that lets through only part of the waveform. This chapter shows that for the signals received at Ascension different sea-floor obstructions and source depths resulted in signal windows with different widths. An unexpected result is that the time window is relatively short compared to the recorded signal duration for all the signals. This means that, for all the signals, energy was received at times when no direct refracted rays could have arrived. This non-refracted energy could only have been carried by reflected rays, resulting in arrival waveforms composed of a combination of direct and reflected rays. The earlier arrivals are entirely reflected and the later arrivals are almost entirely direct. For some waveforms, the direct ray window was completely closed and these arrivals must be composed entirely of energy from reflected rays. In the last part of the chapter reflected rays are investigated and it is shown how the depth of the ray turning point can be changed on reflection.

5.1. Mismatch in the duration of the arrival waveform

In Chapter 4, it was shown that Walvis ridge varies between 1500 and 2500 metres in depth for the shot tracks. The duration of the signals passing over this ridge and being received at some point beyond the ridge can be found using equation 3-2 which calculates arrival time as a function of turning point depth. Figure 5-1 shows the calculated depth versus delay curve for the sound speed profile at Ascension and a path length of 4.4 Megametres. The time window for shot 7 and hydrophone 30 is illustrated, showing that the signal window only lasts for 1.5 seconds. (The implicit assumption in using this graph to determine waveform duration is that all rays deeper than the obstruction are totally absorbed.) In the same way, the time window duration for an axial source and ridges at 1500 and 2500 metres can be read from the graph as 0.7 and 6 seconds respectively.

In contrast to this, the recorded arrival waveforms (Figures 2-9) are about 10 to 15 seconds long. There is clearly a serious disagreement between the duration of the predicted and observed waveforms. This can only be due to faster-travelling rays (deeper rays) arriving at the receiver although their direct path is blocked by Walvis ridge.

5. Off-Axis Sources, Obstructions And Reflections

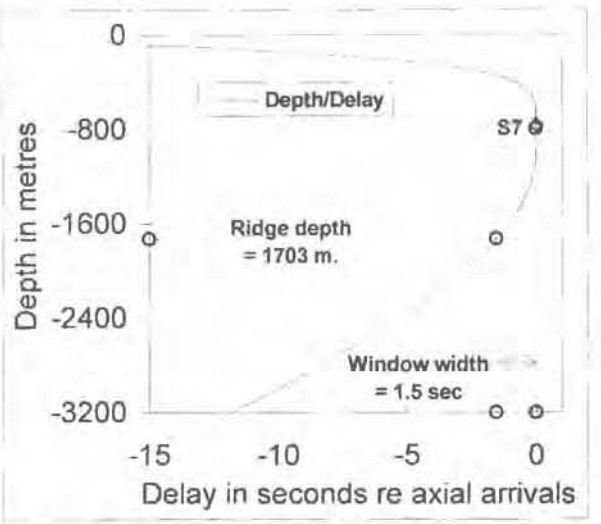

Figure 5-1 Delay profile, shot and conjugate depth.

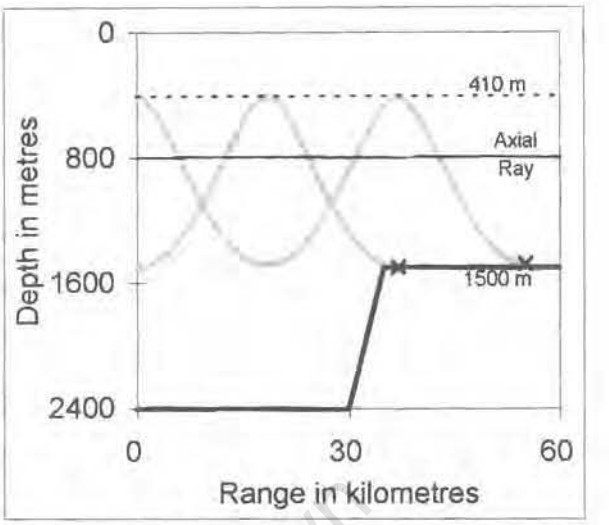

Figure 5-3 Axial and off-axis sources with obstruction

Up to now, the assumption has been that only refracted rays need be considered, that is, all rays encountering the sea-floor are assumed to be totally absorbed. This is a valid assumption for rays travelling long distances over a flat sea-floor, since a ray that reaches a reflecting surface will thereafter be reflected repeatedly and will be attenuated to negligible amplitude by reflection losses. Such conditions are discussed by Bryan, *et al.*, (1963). However, a narrow ridge or a steep seamount may re-direct a ray with only a few reflections so that reflected energy of significant amplitude arrives at the receiver. The way in which this happens will be investigated later in this chapter.

5.2. Source conjugate depth compared to ridge depth

Figure 5-2 shows the effect of a blocking ridge on an off-axis source. The ray transmitted horizontally from the source at 1500 metres has its lower turning point at 1500 metres and just collides with the obstruction at 1500 metres depth. The horizontal ray, starting from the conjugate depth of 410 metres, traces out an inverted path with upper and lower turning points at exactly the same depth. If the conjugate depth of the source is greater than the ridge depth, all rays from the source will be intercepted by the ridge. In terms of the time window, the trailing edge of the window meets the leading edge so that the window is closed. If the conjugate depth of the source is less than the depth of the ridge, the less steep rays will pass above the ridge. In the time window analogy, the trailing edge is closer to its point of origin (the axis of the sound channel) and so the window is open for some time.

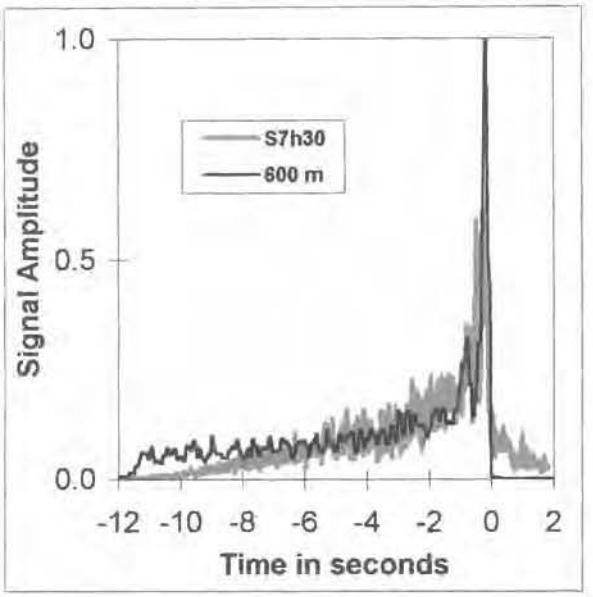

Figure 5-5 Normal mode (800 m axis) and recorded envelope.

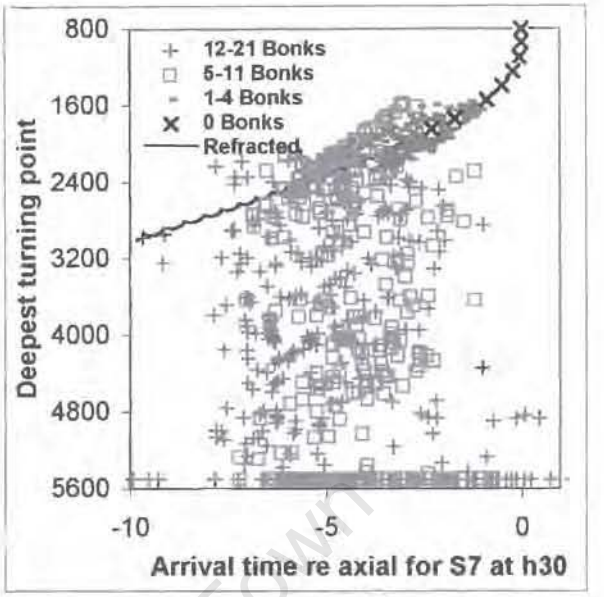

Figure 5-7 Time-front showing direct and reflected ray end points.

5.3. Comparing observed signal shape with the normal mode prediction

Figure 5-3 compares the envelope of the signal received from shot 7 at hydrophone 30, and the normal mode synthesised signal for a bottom depth of 3500 metres, the sound channel axis at 800 metres, and a source depth of 600 metres. The curves are normalised to their peak values. The peak shape and widths are in good agreement but the shape of the rest of the received signal is rather different, showing a gradual start and steady slope in comparison to the step at the leading edge and plateau of the synthesised signals. This mismatch in shape supports the idea that the early part of the signal consists of reflected rays. The S7h30 peak is in the direct ray window and must consist almost entirely of refracted rays while the long slope up to the peak must be the sum of reflected rays. The way in which reflected rays could reach the source is investigated below. The signal synthesised for a source depth of 600 metres provides the closest match to the observed signal despite the measured source depth being 765 metres. The reasons for this mismatch will become clear in the next chapter.

5.4. Ray trace model of reflected rays

A ray trace model (Bowlin, 1994) was used to investigate the behaviour of reflected rays. The model traces refracted and reflected rays, searches for eigenrays, and stores summary results. Typical graphs obtainable from the output data are shown in Figures 5-4 to 5-8. For simplicity, the sound speed profile at Ascension was taken as being representative of the

whole area. Figure 5-5 shows the entire path in profile. The bathymetry used for these plots is derived from the GEBCO Digital Atlas on CDROM. The contour interval of these charts for deep water is usually 500 to 1000 metres and the distance between adjacent points on contour lines can be as close as 1500 metres. The distance between the source and the receiver is 4.4 Mm.

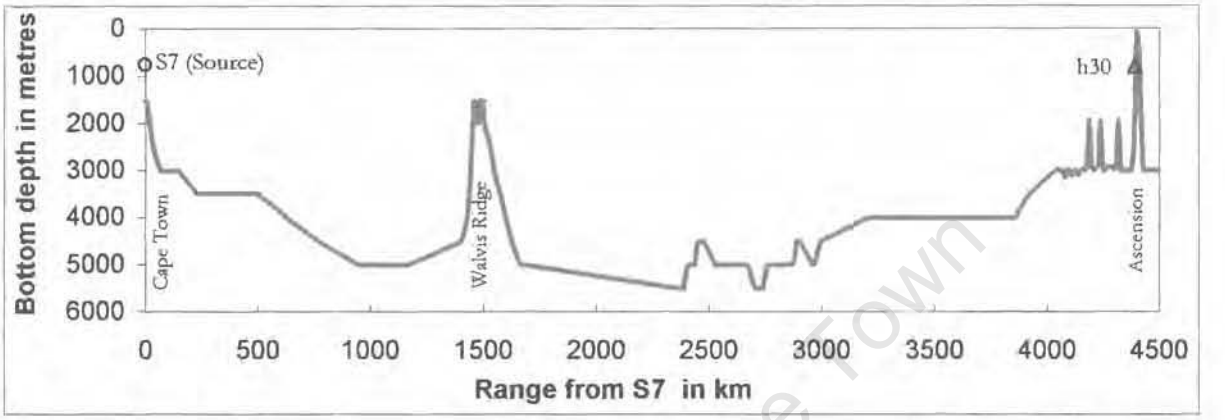

Figure 5-9 Bathymetry of the Cape Town to Ascension path for S7 to h30

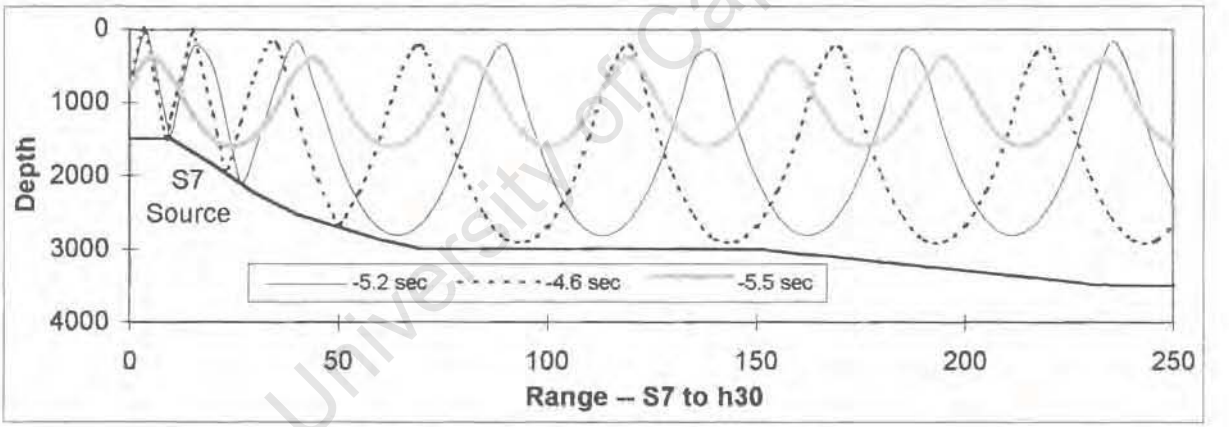

Figure 5-11 Eigenrays at the source

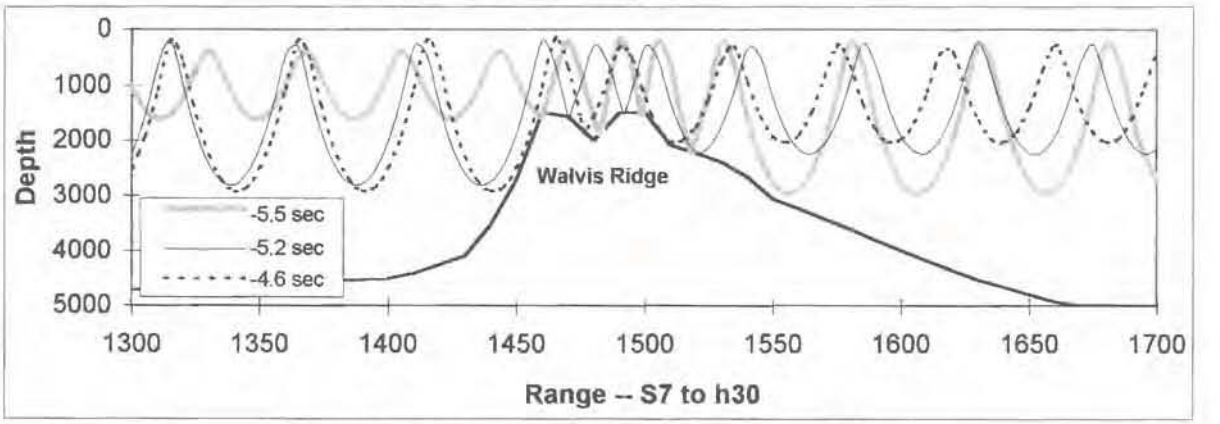

Figure 5-13 Eigenrays reflected at Walvis Ridge

5. Off-Axis Sources, Obstructions And Reflections

The transition of the rays from entirely reflected to mainly refracted for the S7h30 track is illustrated in the time front shown in Figure 5-4. It shows the maximum turning point depth versus arrival time for both the flat ocean floor (continuous line) and the sea floor with ridges (points). The solid black trace represents the locus of direct, refracted ray arrivals for a flat sea-floor, while the points are arrivals after the stated number of reflections (called "bonks' in the Bowlin ray tracing program) from undersea ridges and the sea surface. The window of direct rays starting at about 1.5 seconds before the axial arrival time shows up quite clearly. The results for the sea-floor with ridges (denoted by crosses) initially follow those of the flat floor (black line) for the slowest rays (only a sparse selection of these points is shown, so as not to obscure the line), but then deviate in both depth and arrival time. For the reflected rays, there is no simple relationship between arrival time and the maximum depth of the turning points. Figure 5-4 shows the end points of many rays that have been retarded or accelerated while Figures 5-6 to 5-8 show particular retarded or accelerated rays.

Reflected rays					
Delay Time	Maximum Depth	Launch Angle	Top Reflections	Bottom Reflections	Arrival Angle
-5.52	3000	6.08	0	7	-13.9
-5.24	2814	15.79	1	6	8.6
-4.6	2918	16.65	2	4	8.1
Refracted rays with the same delay					
Delay Time	Maximum Depth	Launch Angle	Top Reflections	Bottom Reflections	Arrival Angle
-5.52	2412	9.46	0	0	+/- 9.5
-5.24	2368	9.31	0	0	+/- 9.3
-4.6	2268	8.96	0	0	*/- 9

Table 5-1 Comparison of reflected and refracted rays

5.5. Investigation of reflected rays

Figures 5-6 to 5-8 show some of the reflected rays as well as profiles of the undersea areas where rays are reflected. The legends for these figures refer to the delay time, in seconds, compared to the arrival time of the axial ray. Table 5-1 lists the delay time for the ray as compared to the axial ray, the maximum depth (of the turning point or the reflection), the launch angle at the source, and the number of reflections. For comparison, the table is repeated for refracted rays with similar delays.

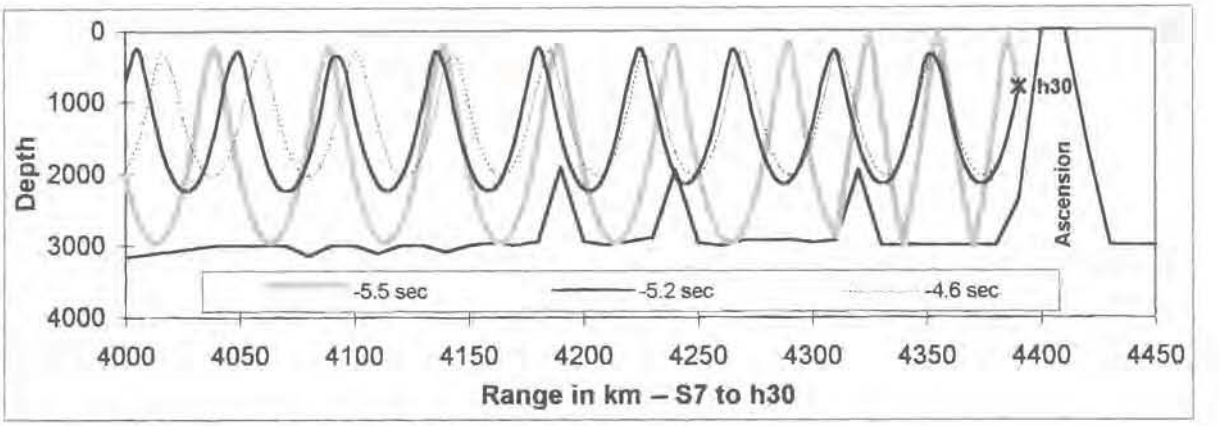

Figure 5-15 Eigenrays at the Ascension receiver

Figures 5-7 and 5-8 and Table 5-1, show that the depth of the ray turning points are considerably changed by being reflected off Walvis Ridge. Rays are converted both to steeper (the - 5.5 seconds ray) and less steep (both the - 5.24 and - 4.60 seconds rays) angles at Walvis Ridge. The - 4.6 seconds ray is also converted from a potentially very steep ray to a much less steep ray by reflections at the source. If a reflection coefficient of 0.7 at low angles of incidence were assumed, the final ray amplitude would still be 0.08 to 0.2 times the amplitude before reflection. Since there are many of these reflected rays and their amplitudes could add, the final amplitude may be comparable to the sum of the direct rays.

5.6. Comparison of arrival times of direct and reflected rays

In Figure 5-4 it can be seen that the first reflected rays occur at about 1.1 second, corresponding to a turning or reflection depth of about 1650 metres, which is about the same depth as the highest peaks of Walvis Ridge. The deepest ray to get through without reflection has a turning point at 1850 metres, corresponding to a delay time of 2.3 seconds.

In Figure 5-3, the amplitude of the received signal deviates from the theoretical at 1.5 seconds. This suggests that the energy of the reflected rays is mainly received before 1.5 seconds. The distribution of the scattered points in Figure 5-4 agrees with this – particularly those points that have been reflected 1 to 11 times and which should have the largest amplitudes. There is a paucity of points earlier than 6 seconds in Figure 5-4 that does not agree with the waveshape of Figure 5-3.

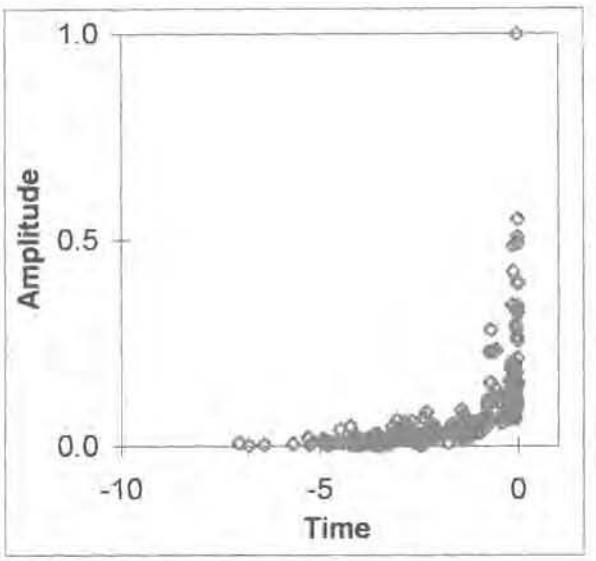

Figure 5-17 Amplitude of rays in time front

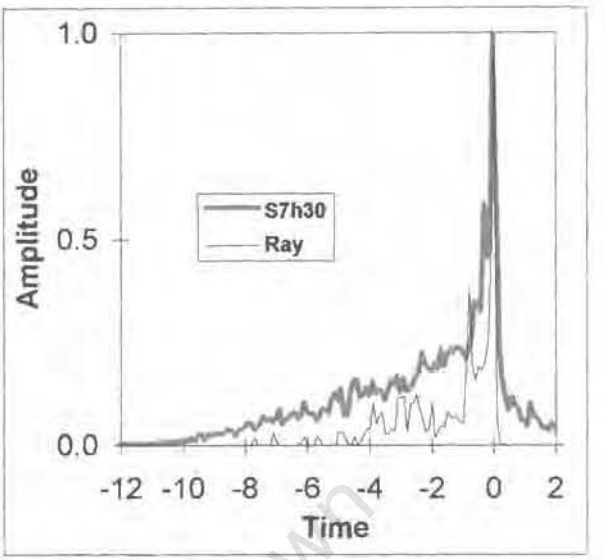

Figure 5-19 Ray trace synthesis compared to recorded signal

A particular ray arriving at the receiver is identifiable only by arrival time and arrival angle (if the receiver can detect angles). It can be seen from Table 5-1 that reflected rays could be mistaken for refracted rays although the paths and temperature sampling depths may be quite different. This is potentially a problem for ATOC receivers.

Referring back to Figure 5-3, it shows that the gradual increase in slope above noise level of the recorded signal could be caused by the summation of many reflected rays with the number of reflections (and hence the loss in reflected ray amplitude) greater for the faster rays. The decrease in amplitude of rays with decreased travel time (and an increased number of reflections) is illustrated in Figure 5-9. The amplitude of the reflected rays was calculated on the assumption that half the energy is lost on each bottom reflection.

5.7. Ray trace synthesis of arrival waveform

A subset of the rays making up the time front shown in Figure 5-9 is the eigenrays that contribute energy to the arrival waveform. These eigenrays can be compiled into an arrival waveform using equation 5-1. Finding the eigenrays is no easy task, since many eigenrays exist if multiple reflections are allowed and since the relationship between ray launch angle and arrival depth becomes non-linear (Dushaw, 1998 and Dushaw and Colosi, 1998). For the topographical model used here, it is likely that the multiple reflections encountered result in ray chaos, so the synthesised arrival waveform may not be a valid prediction.

5. Off-Axis Sources, Obstructions And Reflections

The equation for summing rays into an arrival waveform is:

$$S_t := \left[\sum_{n=1}^{N} \left(a_n \cdot S_{f_t} \cdot e^{j \cdot 2 \cdot \pi \cdot f_t \cdot \tau_n} \cdot e^{j \cdot s_n \cdot \frac{\pi}{2}} \right) \right] \quad \text{..... Equation 5-1}$$

where

S_t = signal in the frequency domain, written as a vector

t = element (sample) number in vector

n = ray number from 1 to N

a_n = amplitude of ray

S_f = source signal in the frequency domain, written as a vector

τ_n = travel delay of ray

s_n = number of reflections

The time domain signal is obtained as a time series by taking the inverse FFT of S_t. (Chapter 8 of Jensen et al., 1994, Grabb and Birdsall, 1995)

The Bowlin ray program tabulates (amongst others) amplitude, arrival time, and number of reflections for each eigenray. Searching for eigenrays with the topography for S7 to h30 with the Bowlin program gives a matrix of values that can be used in equation 5-1. This, after taking the moving maximum of the positive envelope, results in the synthesised arrival waveform in Figure 5-10. The synthesised signal is not a good match, as it exhibits a pronounced secondary peak and the amplitude is mostly too low. This mismatch may well be due, at least partially, to ray chaos.

Chapter 6. Depth Of The Local Sound Channel Axis

Chapter 5 showed that the modelled width of the time window (for direct rays) is far shorter than the recorded duration and that the early part of the recorded signals must therefore consist of reflected energy. The leading and trailing edges of the time window for shot 7 were calculated as an example. In this chapter, the width of the time window for each of the shots is calculated. The size of the peaks and the arrival times of some of the modelled arrival waveshapes are not in good agreement with the recorded waveshapes. This agreement can be improved by assuming a greater depth for the local sound channel axis. The sites where a greater local sound channel depth is assumed are close to the location of the filament of warm water described in chapter 2.

6.1. Leading and trailing edge times for refracted rays

The predicted time of arrival for the leading edge of the time window (relative to the trailing edge) can be calculated for each of the shots, using equation 3-2. The depth versus delay curve derived from equation 3-2 is shown in Figure 5-1. The sound speed profile at Walvis ridge is considered fixed so that the time of the leading edge is simply a function of the ridge depth for each shot path. The calculated predicted leading edge times are given in Table 6-1.

Shot Track	Ridge Depth	Leading Edge
S1h30	1730	-1.53
S2h23	2300	-4.59
S3h30	2500	-5.98
S4h30	2000	-2.80
S5h30	1512	-0.75
S6h30	1512	-0.75
S7h30	1730	-1.53
S8h30	1730	-1.53
	m.	sec.

Table 6-1 Calculated leading edge times.

The trailing edge of the recorded waveforms can be estimated from the differential arrival times, that is, the arrival time relative to the predicted axial arrival time. The calculation of the differential arrival times is shown in Table A-3 in the appendix. The resulting trailing edge times (relative to the predicted arrival time) are summarised in Table 6-2. The depth of sound speed axis assumed up to now for all calculations, including Table 6-2, is 800 metres.

Shot Track	Source Depth	*Trailing Edge
S1h30	706	0.82
S2h23	465	-1.65
S3h30	675	-2.76
S4h30	507	-1.93
S5h30	403	-0.72
S6h30	401	-0.12
S7h30	765	-0.04
S8h30	440	-0.64
	m.	sec.
*Time is measured relative to the calculated axial arrival time		

Table 6-2 Measured trailing edge times.

The errors in measuring the detonation time show up in the timing of the trailing edge in Table 6-2. Shots 5 and 6 occurred at very nearly the same

depth and position, and should therefore have the same travel times, but instead show a difference of 0.6 seconds. Similarly, shots 1, 7, and 8 started at nearly the same depth with a nearly common path but show a discrepancy of 1.5 seconds in travel time. Despite these errors, the trailing edge time errors for shots 2, 3, and 4 stand out by being two to three times larger. A likely explanation for the early termination of shots 2, 3, and 4 is that they are far above the axis of the sound channel and that this causes the early termination (as can be seen from the depth-delay relationship in Figure 5-1).

6.2. Waveform shape and distance off-axis

In Chapter 3, it was shown that the relative height of the peak indicates how far off-axis a source is. Figure 3-17 shows the synthesised arrival shapes of sources at various depths for a sound channel with its axis at 800 metres. For sources at, or deeper than 500 metres, there is a definite peak at the termination of the signal. This peak can be seen in shots 7 and 1 in Figure 2-9, but is missing in all the other shots, despite all of them being deeper than 400 metres and S3 being close to 700 metres in depth (Table 6-2). The absence of a peak indicates that the shots must be farther off-axis than assumed. The source depths are known fairly accurately from the calculation in Chapter 2, so it must be that the axis is deeper than assumed. Since the warm water filament near the sources may well have displaced the axis downwards, it is worth modelling the effect of the displacement on the shape and trailing edge time of the arrival waveshapes to see how well the model will fit with observations.

To simplify the depth calculation of the sources, we need to assume that near-axial rays oscillate about the axis, even though the axis may change in depth (the adiabatic approximation). A corollary of this is that energy may be more or less concentrated as the steepness of the sound speed gradient changes, but no energy is lost. Equations 3-2 and 3-3 can then be used in Table 6-3 to calculate the delays to be expected from shots located in sound channels with axes at different depths.

6.3. Matching trailing edges

In Table 6-3 a new set of local axis depths is chosen to make the trailing edge times (fourth column) match the observed trailing edge times in Table 6-2 more closely. The new trailing edge times are later referred to as probable delay times. The axis depth for shots 1, 7, and

8 must be the same since the sites were close together. Similarly, the axis depth for shots 5 and 6 must be the same.

Figure 6-1 illustrates the values in the first four columns in Table 6-3 by showing the upper part of the depth versus delay curves for different axial depths, the depths of the shots and the probable delay of the shot trailing edge compared to axial travel time.

Shot Track	Source Depth	Axis Depth	Trailing Edge*	Ridge Depth	Leading Edge*	Window Width	Blockage Effect
S1h30	706	900	-0.03	-1730	-1.53	1.50	Partial
S2h23	465	930	-1.68	-2300	-4.59	2.92	Partial
S3h30	675	1190	-2.79	-2500	-5.98	3.19	Partial
S4h30	507	985	-1.93	-2000	-2.80	0.87	Partial
S5h30	403	800	-0.78	-1512	-0.75	-0.03	Total
S6h30	401	800	-0.79	-1512	-0.75	-0.05	Total
S7h30	765	900	-0.01	-1730	-1.53	1.53	Partial
S8h30	440	900	-1.61	-1730	-1.53	-0.08	Total
	m.	m.	sec.	m.	sec.	sec.	
*Time is measured relative to the calculated axial arrival time.							

Table 6-3 Axial and source depths and window times.

6.4. Matching up waveform shapes

In the previous section, an estimate of axial depth was made, based on timing delays. In this section, an independent estimate of axial depth will be made, based on waveform shape. This can only be done for the shots with pronounced peaks, that is, for shots 1 and 7.

The effect of warm eddies on the sound speed profile is to depress the whole profile by up to some hundreds of metres (Figure 1 of Brundrit and Krige, 1994.). Referring back to Figure 2-4, shots 1, 7 and 8, and 5 and 6 are lying on the outskirts of a filament of warm seawater, while shots 2, 3, and 4 are behind an arm of the warm water. Some depression of the sound speed

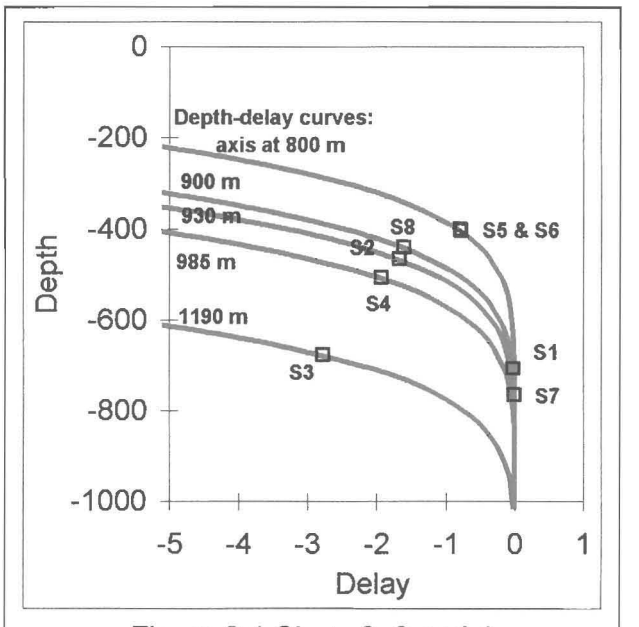

Figure 6-1 Shots 2, 3 and 4

channel for shots 2,3 and 4 and 1, 7 and 8 is probable.

Figure 3-17 shows the signals synthesised for sources at different depths relative to an axial depth of 800 metres. Synthesising normal mode waveforms for a displaced sound channel with the axis at 900 metres gives a new family of shapes shown in Figure 6-2. The synthesised signal shapes for different depths of the channel axis are matched to the recordings of shot 7 and shot 1 in Figures 6-3 and 6-4. The best match for S1 and S2 is for source depths of 750 and 700 metres respectively. This is close to the measured source depths and indicates that a local axis depth of 900 metres is near optimum for matching signal shape.

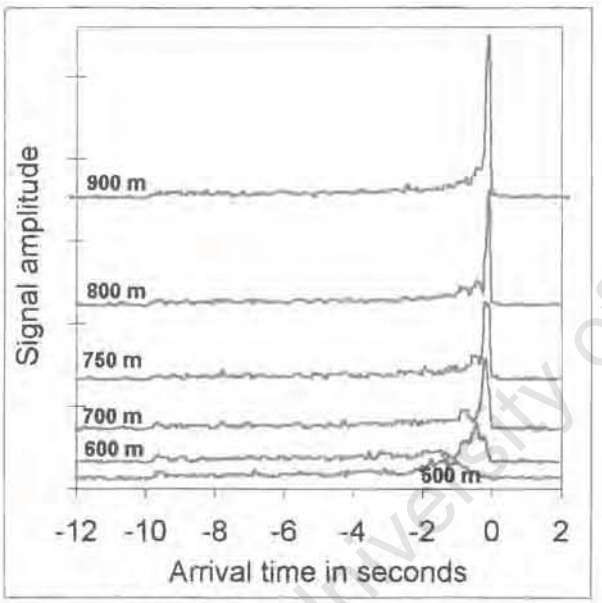

Figure 6-3 Normal mode prediction for off-axis sources.

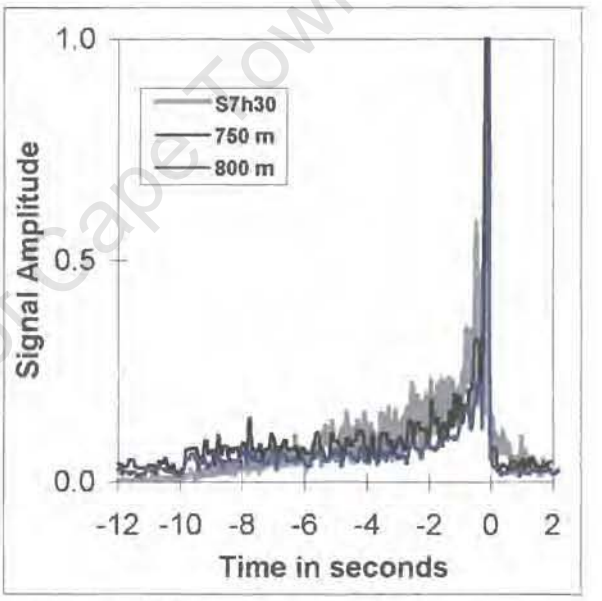

Figure 6-5 Matching shot 7 for shot depth

6.5. Agreement between modelling trailing edge time and signal shape

The results of matching trailing edges and shapes are in good agreement for shots 1, 7 and 8, given the limits on the accuracy of the shot timing and the insensitivity of the modelled shape to depth. Using an axis depth of 900 metres for shots 1, 7 and 8 in Table 6-3 and calculating trailing edge times gives a time window of 1.5 seconds which agrees with the recorded peak width of shot 7. For shot 8 the window is just closed which agrees with the shape of the recorded signal – no peak, but close to the start of the peak, as indicated by the increasing amplitude.

6. Depth Of The Local Sound Channel Axis

For shots 5 and 6, the window is just closed for an axis depth of 800 metres. The shapes of shots 5 and 6 show no sign of a peak at termination, suggesting that the axis of the sound channel might be deeper. However, a deeper sound channel would require a greater delay in the trailing edge. The average time delay for shots 5 and 6 fits approximately with an axial depth of about 800 metres.

The waveforms of shots 2, 3 and 4 in Figure 6-5 show that the peak of the final crescendo is missing in all three cases as would be expected for shots far off-axis. From Table 6-3, the window is open for a short period for all three shots. There is no obvious sign of the change in amplitude that would be expected for the transition from reflected to direct energy. Table 6-3 shows that the chosen depths of 920, 1190 and 985 metres for the axis of the sound channel result in approximately correct arrival times. Figure 2-3 shows that shot 4 is located near the edge, but beneath, a filament of warm surface water so that a downward displacement of the sound channel axis for shot 4 is probable. For shots 2 and 3, the proximity of warm water (and the tendency for the underwater structure to be displaced horizontally with increasing depth) makes the downward displacement of the sound channel a strong possibility.

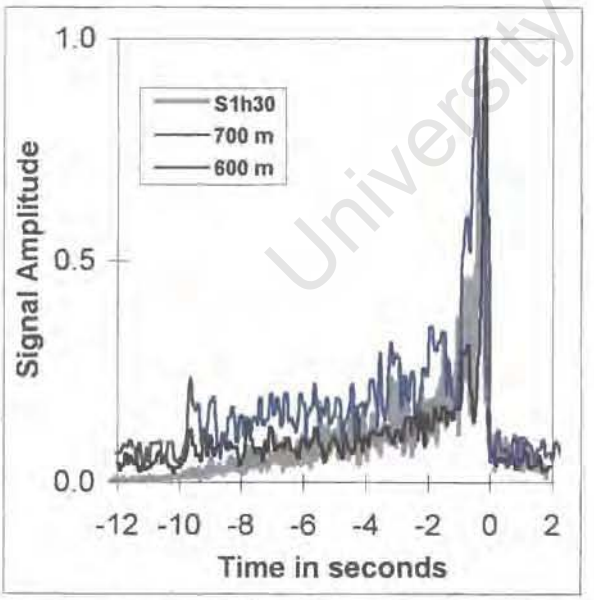

Figure 6-7 Normal mode prediction for off-axis sources.

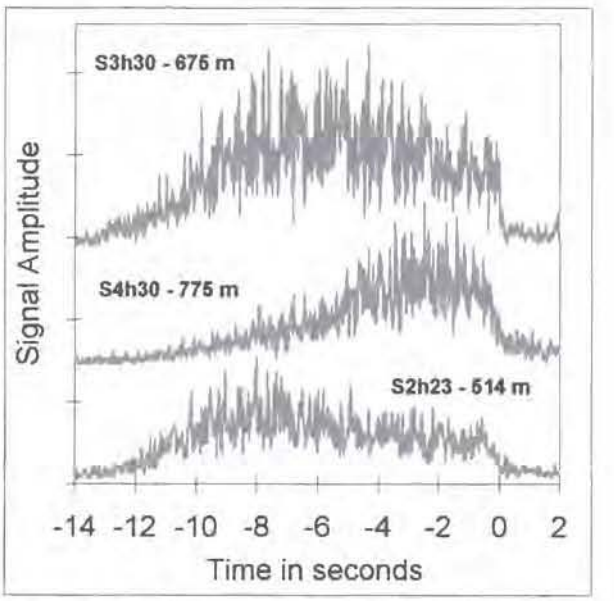

Figure 6-9 Recorded arrival waveforms for shots 2, 3 and 4

It is worth noting that due to the rapid increase in delay time for the shallower sources in the depth versus delay curve of Figure 6-1, the assumed axial depths cannot be too far in error. For instance, if the axial depth for shot S5 were assumed to be 985 metres, the delay time

would jump to over 5 seconds, which would be outside the acceptable limits of error in detonation time.

The model used above is very much of an approximation. The sound speed profile and particularly the depressed profile will not be as regular and predictable as shown. However, the examples do show that the depressed sound channel, in combination with an underwater ridge, could cut off the direct rays and that the numerical values fit approximately.

Chapter 7. Discussion And Conclusion

7.1. Principal objective

The principal objective of this thesis has been to investigate and analyse the data to gain an understanding of the results. The high quality of the digital recording at Ascension made it possible to analyse the recordings in detail, and to do spectral and cepstral analysis. The signal amplitude graphs shown in Figure 2-9 were the first step in the analysis – explaining how they came about occupies most of the rest of the thesis.

7.2. Models

The variation in shape and duration of the observed signals led to the use of models to predict these parameters. Ray theory provides a conversion from a spatial (depth) aperture for rays to a delay time window for arrival waveforms. The leading and trailing edge time of the window can be determined from obstruction and shot depths. This simple tool has been used throughout the thesis to predict arrival and termination times for a given the depth of bottom obstruction and the depth of sources relative to the axis of the sound speed channel. Normal mode theory has been used to predict the decrease in the SOFAR peak in arrival waveshapes resulting from sources progressively farther off-axis. A comparison between the model and those signals that have identifiable SOFAR peaks has been used to find the approximate source depth relative to the sound channel axis. Since the depth of the explosion is an essential parameter for these calculations, the shot depths not measured during the trial were calculated from the cepstrum of the recorded signals.

7.3. Correlation of signal attenuation and topographical obstructions

Mapping undersea obstructions and signal paths led to the first simple insight. Comparing signal peak amplitudes with the signal paths made it clear that two of the hydrophones were almost in the shadow of hydrophone 23 and that the data from those hydrophones was largely redundant.

The graphs of signal amplitude (Figure 2-9) show that although each shot was received almost simultaneously on each of the three widely spaced receivers (hydrophones 23, 29 and 30), the amplitudes of these three receptions are different. The differences must be due to different propagation conditions along the path. This realisation led to a test for the

correlation of signal path obstructions with the relative signal strength at the hydrophones. The signal paths were calculated as great circles on a spherical earth. The improved accuracy of a geodesic calculation is not justified since the difference in horizontal displacement between great circles and geodesics is smaller than the resolution of the undersea map. Both seamounts Bonaparte and Grattan obscure some of the signal paths. It has been shown that there is good correlation between signal strength and path obstruction. Thus, the obstruction of the paths by seamounts Bonaparte and Grattan explain the amplitude variation between hydrophones for a given shot. The large peaks present on hydrophone 30 (and to a lesser extent on hydrophone 29) but not on the other hydrophones for shots 1 and 7, are variations in shape rather than amplitude and there seems to be no good reason for this other than variability in propagation conditions.

7.4. Adding reflected energy to the model

The observed arrival waveforms last too long to fit within the time window predicted by modelling of the refracted energy alone. The energy arriving earlier than the first direct energy must consist of rays with deeper turning points (that is, faster rays) that have been reflected over Walvis ridge. The idea of the arrival waveform being composed of both reflected and refracted energy has been tested using shot 7 as an example. A ray trace model gives the same window width for the direct energy as the depth-delay graph. An arrival waveform synthesised from the ray trace model gives a similar peak to that of the observed waveform but the modelled reflected energy is not in good agreement with the observations, probably due to ray chaos. The modelled reflected energy does not start early enough and the amplitude is too small to match the recorded waveform exactly. This seems to be due to an inability to model multiple reflections accurately. However, the match is good enough, particularly in the absence of any other obvious explanation, to make the concept of a combination of reflected and refracted energy convincing.

7.5. Discriminating between direct and reflected energy

If the arrival waveforms consist of both reflected and direct energy, a change in amplitude could be expected during the transition in the type of energy. This change would be caused by the reflected energy being smaller in amplitude than the direct energy (Chapman and Ebbeson, 1983; Medwin and Spaulding, 1980.). This kind of change is not obvious in the recorded waveforms, which seem to blend smoothly right across the calculated leading edge time.

7. Discussion And Conclusion

The predicted amplitude of the direct signal at the foot of the peak in Figures 6-3 and 6-4 matches remarkably well in magnitude (though not in slope) with the recorded amplitude of the reflected energy. There does not appear to be a reduction of amplitude for the reflected energy at this point. For shots 5, 6 and 8, all the received energy is likely to be reflected. The peak amplitude of these signals is about 5 to 8 times less than that of shot 7. According to the normal mode model, shots 5 and 6 should be attenuated by a factor of four due to the source being off-axis at 400 metres, as illustrated in Figure 3-17. This only allows for a factor of 1 to 2 for attenuation by reflection. A much larger attenuation factor would be expected.

For shots 2, 3 and 4 (Figure 6-5) the widths of the transmission windows are calculated as being from about 1.6 to 2.8 seconds. There are no obvious changes in amplitude in Figure 6-5 to show a transition from reflected to direct energy.

The following factors could account for the apparent smooth transition between direct and reflected energy. The ray trace model showed that there is considerable overlap in the periods when direct and reflected rays are received. In addition, the reflection coefficient is a function of grazing angle with the reflection coefficient being close to one for small grazing angles, such as would be encountered in the transition. However, the overall reflection coefficients appear to be greater than expected and there does not seem to be any good reason for this.

7.6. Simulating arrival waveforms with scattered rays

None of the waveforms compiled from scattered rays showed a good resemblance to the recorded arrival waveforms. It seems probable that the model is subject to ray chaos. The model also does not simulate the diffusion of sound from rough surfaces and the bathymetry is only approximate. Spiesberger and Tappert, (1996), and Wolfson and Spiesberger, (1995), use ray trace and parabolic equation models for predicting the propagation of scattered energy in a situation where there are far fewer reflections. They also find evidence of ray chaos in their ray-trace model. It seems probable that there are, at present, no models available that can deal adequately with the multiple reflections encountered in this situation.

7. Discussion And Conclusion

7.7. Local displacement of the sound channel axis

After matching the leading edge of the model to the observed time as well as possible, there were still two other discrepancies:

- The trailing edge times of a number of the shots were earlier than predicted by a few seconds and
- The shapes of shot 7 and 1 did not fit with the normal mode model for a sound channel axis at 800 metres.

Adjusting the modelled depth of the local sound channel axis deeper than 800 metres, made the predicted trailing edge times earlier. A modelled local sound channel depth of 900 metres also gave good agreement between the observed and modelled waveshapes for shots 1 and 7. The sites where the sound channel was displaced downwards in the model are close to the area where the filament of warm water would be expected to displace the sound channel downwards.

The process by which the shapes and amplitude patterns recorded at Ascension arose, can now be said to be well understood. Since the processes can mostly be quantified and modelled, the principal objective of the thesis has been achieved.

7.8. Shortcomings in design and execution of ATOC-FACT

With the clarity of hindsight, and without criticising the participants for their excellent work, some shortcomings in the design and execution of the ATOC-FACT test have made the analysis of the test more difficult and the results less precise.

After the decision to use explosive sources, we underestimated the value of precise timing of the detonations and used a procedure that probably gave errors of about plus or minus a second. This uncertainty in timing (and the uncertainty of the position of the shot at the end of about 1 kilometre of cable) is some orders of magnitude greater than that for the recordings at Ascension. Also, thinking that the test was mainly about undersea topography, we considered the determination of the sound speed profiles in the immediate vicinity of the sources to be of lesser importance than it has since proven to be.

Due to equipment failures, the ATOC-FACT experiment did not obtain source detonation depths for all the sources and no XBT readings were taken in the detonation areas. Since the depth of the source relative to the axis of the sound channel is all-important in determin-

ing the arrival waveshapes, these depths had to be calculated or estimated from other evidence. The modulation of the shot sound at the bubble pulse frequency provides an alternative, less direct, means of verifying the shot depth. (To judge by the discrepancy in Table 2-1 between the bottom bounce and bubble pulse modulation methods of estimating explosion depth, the error in these estimate is up to 50 metres of depth.) Given these depths, an estimate of the depth of the sound channel axis can be made from the shape of the waveform and the trailing edge delay (Figure 6-1 and Tables 6-2 and 6-3). This is a roundabout method that lacks precision, but the only one available, given the lack of measured data.

7.9. Using underwater explosions for path verification

It seems that underwater explosives could be used more often for verifying that uncharted bathymetric features do not interfere with long-range paths intended for acoustic thermometry. The first step in evaluating paths is usually to model propagation with rays and some database of undersea topography. This gives an excellent general picture but the resolution of the database is usually not good enough to identify smaller features that are nevertheless large enough to block most of the signal on a particular path. As an example, seamount Grattan is not shown on most undersea maps but its existence could be inferred from the received amplitudes of the Ascension recordings. It was only when we started looking for an obstruction in a defined area, using different maps, that this small seamount (which, despite its size, rises to within 72 metres of the surface) was revealed. Expensive mistakes in siting transmitters and receivers could be avoided by doing relatively inexpensive explosive transmission tests. This thesis has shown how the effects of intervening topography can be identified from the SOFAR signal using explosive sources.

7.10. Suitability as an ATOC line

The motivation for the feasibility test on the Cape Town to Ascension line was to evaluate the suitability of the line for ATOC measurements. At the time when the results were first seen, the verdict was that signals could indeed be received, but there were so many unknown factors affecting the signals that a more detailed assessment was not possible. These uncertainties have now been cleared up and some factors have been quantified. A more detailed evaluation, in the light of present knowledge, follows.

7. Discussion And Conclusion

Only shots 1 and 7 were deep enough relative to the sound channel axis for some direct, refracted rays to reach the receivers. Shots 5 and 6 were deployed and detonated too close to the surface, due to strong wind and currents at that site. All the other shots suffered from some combination of shallow deployment and a displaced sound channel. In addition to this, shot 4 was so placed that all the hydrophones were obscured by either seamount Bonaparte or Grattan. The displacement of the sound channel axis in the immediate vicinity of a permanent source by a filament of warm water could result in a disruption of information for a period of weeks. (Duncombe Rae, 1991)

Although there are different ways of using the received signals, (for example, Heaney and Kuperman (1998) discuss an application of matched field processing, so called because the full complexity of the arrival *field* is matched to a model), acoustic thermometry is concerned only with the travel time of the energy and, usually, only with the travel time of the faster rays. The advantages of using the faster rays are that they are relatively well separated in arrival time, making identification easier and that they sample the shallower water where most of the temperature change occurs. They are also less subject to disturbances caused by internal waves (Colosi *et al.*, 1999). Conversely, the arrival density of near-axial, slower rays is so great over long distances that they cannot be resolved and they sample only near-axial water temperatures.

Up to now the largest scale, long term ATOC monitoring has been in the Northeast Pacific where the sea floor is relatively flat. In this area, the fastest rays have been positively identified and their arrival times have been tracked (Dushaw *et al.*, 1996; Worcester *et al.*, 1998.). The topography of the Northeast Pacific is, however, very favourable for ATOC measurements compared to other ocean areas. Most other oceans have ridges that cut through them, potentially intercepting the fastest rays.

Measuring travel time for rays just passing over a high narrow ridge is subject to a number of problems. If the ridge top is close to the axis, the earliest arrivals passing over the ridge are relatively slow near-axial rays and they are less likely to be resolvable. Figure 7-1 shows the time-front for the Ascension sound speed profile and illustrates the increasing density of later arrivals (4 rays during 200 milliseconds at 3 seconds delay). In a real sea, internal waves would make this pattern more irregular and specific ray arrivals would be more difficult to distinguish (Worcester, 1999). An undersea ridge would not truncate the time-

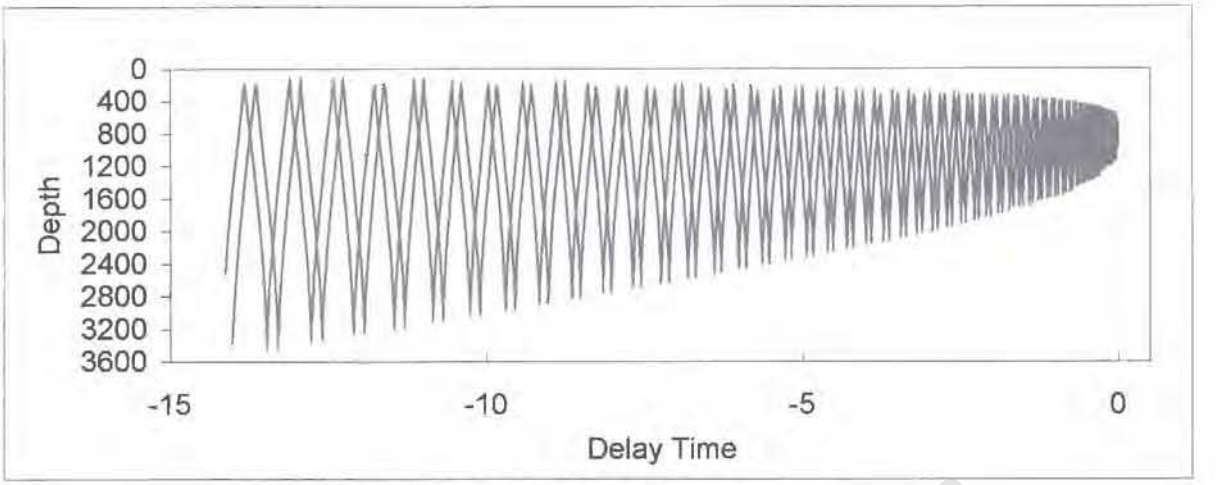

Figure 7-1 Time-front for Ascension

front cleanly, but would disturb the pattern by adding in less stable reflected rays, particularly in the area where the fastest direct rays are cut off by the ridge. This would make it more difficult to track the arrival time of specific rays.

A shallow (near axial) ridge is an extreme example of a bottom limited sound speed profile. All rays penetrating into water shallower than the conjugate of the ridge depth, where most temperature changes occur, are either absorbed or scattered and may become unstable due to the changing geometry of the reflection point.

Axial travel time is an alternative simple determination – a less informative measure and possibly a last resort if the faster energy travel times cannot be determined. However, the hydrophones at Ascension receive echoes from the shallower surroundings, resulting in an extended signal decay time. This can be seen in the comparison of the synthesised and recorded signals in Figures 6-3 and 6-4. The slow decay of the trailing edge of the signal results in some uncertainty in determining the axial travel time, making accurate determination of the axial travel time more difficult.

Clearly, the Cape Town to Ascension line does not compare well with the ATOC lines of the Northeast Pacific. A more realistic comparison is with other possible lines of similar length in the southern or southeast Atlantic. These would probably all suffer similar problems due to mid-ocean ridges and variability of the depth of the axis of the sound speed channel.

7. Discussion And Conclusion

7.11. A different approach

At this time it seems certain that Ascension will become a CTBT (Comprehensive Nuclear Test Ban Treaty) hydro-acoustic monitoring station, which means that the hydrophones there should be available for monitoring all low frequency undersea sounds including ATOC transmissions. This will provide a strong incentive to make the best possible use of the Ascension receiving facility. An alternative approach to ATOC measurements in this area, given a suitable transmitter, would be to use the Walvis ridge obstruction as a vantage point by siting an autonomous source on the ridge with receivers at Ascension, off Cape Town and off the coast of South America. Possible sites for such a transmitter could be the 500 metre deep peak on Walvis ridge at 26.2 degrees south, 6.3 degrees east (Figure 3-1), or seamount Wust (500 metre deep) at 33.8 degrees south, 3.5 degrees west on the continuation of Walvis ridge to the southwest.

Word-wide, most of the mid-ocean ridges rise above the 3000-metre contour with short sections and peaks rising above 2000 metres. In most of the temperate areas of the oceans, a bottom depth of 3000 metres or less will result in rays that do not sample the near-surface temperature (Appendix B: Ocean acoustic propagation atlas, in Munk *et al.*, 1995). This implies that ATOC lines should ideally be chosen not to cross these relatively shallow ridges. For the Atlantic, Indian and southern Pacific oceans, the north-to-south ridges are so shallow and unbroken that continent-to-continent transmissions are hardly possible. Siting the ATOC transmitters on the blocking ridges (preferably at an island where logistical support is simpler) becomes an attractive option.

Some of the islands that could be considered as sites for ATOC transmitters (Ascension, Kerguelen, Crozet and Diego Garcia) have been chosen as CTBT (Comprehensive Nuclear Test Ban Treaty) monitoring sites. Since these sites will continuously monitor low frequency noise in the ocean, ATOC transmitters will have to be sited a considerable distance away so as not to mask the nuclear explosion signatures being monitored.

There would seem to be a shortage of suitable islands for ATOC transmitters. The next most attractive options are either to develop autonomous transmitters or to deploy a transmitter from a vessel.

Appendix A. Calculations and Processing

A.1. Reading Mathcad equations

Many of the Mathcad conventions are what one would expect -- they are simply how one would normally write mathematical symbols and equations.

Here are some of the exceptions:

The multiplication sign is shown only as a dot, i. e., a*b is shown as: $a \cdot b$

There are different uses of the "equals" sign:

Assigning a value to a symbol or function: $c := 1500$

Evaluating an expression: $\frac{c}{1000} = 1.5$

Equivalence (non-functional equation): $c \equiv 1500$

The independent variable in a function must be stated explicitly:

Assign a value for time, t, in seconds: $t := 10$

The range, s, is a funtion of time and speed: $s(t, c) := c \cdot t$

$s(t, c) = 15000$

When a function is raised to a power, the exponent appears at the end of the function, i.e., sin(x) * sin(x) is shown as: $\sin(x)^2$

A.2. Spectra of received signals

Figure A-1 shows the spectra of each of the shots, as received on the hydrophone that gave the best reception. A five second portion of the best signal-to-noise signal was chosen and processed to give the spectrum. A running average of six frequency bins was used to reduce the noise in the display. Since the relative amplitudes do not really convey any information, the spectra have been normalised to give a more readable graph.

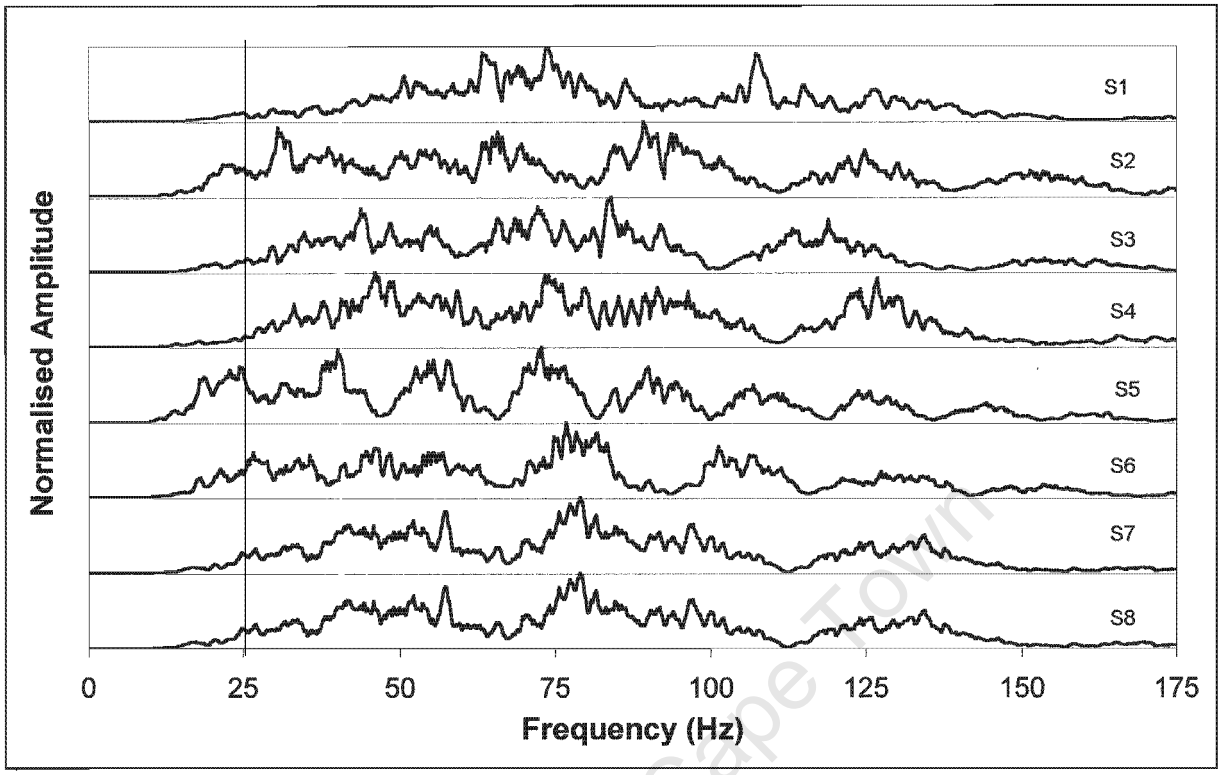

Figure A-1 Spectra of the eight shots.

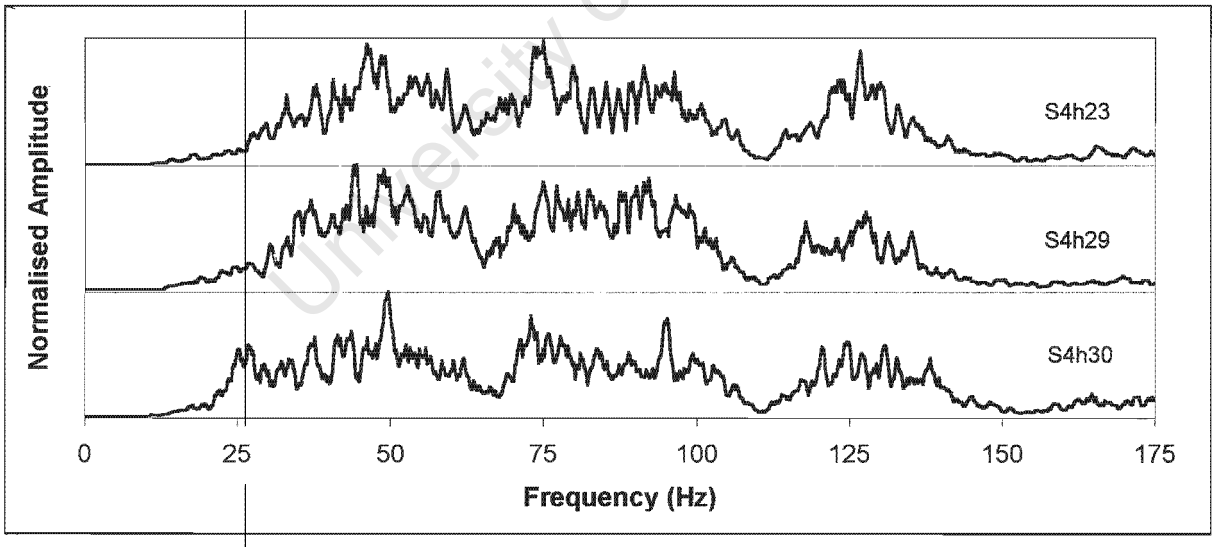

Figure A-2 Comparison of S4 spectra on three hydrophones. .

Figure A-2 shows a comparison of the spectra of shot 4 as received on three different hydrophones. The processing is similar to that for Figure A-1.

A.3. Source Level, Transmission Loss and SNR calculations

Although the transmission loss along the path and the noise level at the receivers can only be estimated approximately, it can be shown that the signal-to-noise ratio at the receivers is what would be expected, given the uncertainties. In Table A-1, the mass of the explosive is known and the peak pressure of the shot can be calculated from equation 2-2. The time constant (that is, the width of the peak) can also be calculated from the mass of the explosive (Urick, 1983). The source level follows from these as an equivalent peak level.

The transmission loss and noise level calculations are somewhat more subjective. In this case, the spreading loss is taken as geometrical for the first 5000 metres and cylindrical thereafter. This formula gives results that are similar to the amplitude determined from the raytrace model. For the absorption loss, a rounded-off figure of $1*10^{-3}$ dB per kilometre was used for the peak frequency (Jensen, *et al.*, 1994, p. 38, Wolfson and Spiesberger,1999, p. 1301.). The deep water noise level was assumed to be 80 dB re 1 microPascal/Hz at 75 Hz (Curtis and Howe, 1995). A bandwidth correction for 135 Hz then gives about 101 dB re 1 microPascal. The signal-to-noise ratio of the received signal is measured from the data for Figure 1-1.

The table below uses only the paths S1 to h30 and S7 to h30. These are the only shots that were sufficiently close to the sound channel axis and hydrophone h30 gives the best results due to the least obstructions.

The predicted signal-to-noise for S7 is within 0.1 dB of the measured signal-to-noise ratio. However, the attenuation and background noise figures are so uncertain that this agreement must be considered fortuitous. The excess of 3 dB in signal-to-noise ratio of S1 is rather small. Errors like these occur all too easily with non-repetitive signals, due to noise and fluctuation of propagation conditions.

Parameter	S1	S7	Units
Mass of charge	7.99	24.60	kg
Calculated Peak pressure	281	285	µPa
Calculated Time constant	159	213	µsec.
Time Constant in dB	-38	-37	DB
Energy flux density (SL)	243	248	dB
Calculated Transmission Loss	108	108	dB
Calculated Noise Level	101	101	dB re 1 µPa
Predicted signal to noise ratio	34.0	39.0	dB
Measured SNR	36.8	39.1	dB

Table A-1 Amplitude and SNR

A.4. Range and bearing calculations

The shape of the earth is usually approximated by either a sphere, or if more accuracy is required, by an ellipsoid. The accepted value for the radius of the sphere is 637100 metres. For the ellipsoid, the WGS 1984 specification is the most commonly used today. The WGS 1984 values are:

Radius of semi-major axis (A) 6378137 metres

Eccentricity (e)0.081819191

The shortest path between two points on a spherical surface is a great circle while the shortest distance between two points on an ellipsoidal surface is a geodesic. The calculation of geodesic distances is considerably more complicated than the calculation of great circle distances.

In this thesis, both great circle and geodesic calculations have been used. In some of the calculations, only relative results are of importance and here great circle calculations have been used. An example of this is in determining the bottom topography of the sound path between source and receiver. The maximum deviation of the geodesic path from that of the great circle is about 1000 metres while the deviation at seamount Grattan is about 200 metres. These offsets are smaller than the resolution of the undersea map (about 1500 metres) and do not to warrant the complication of geodesic calculations.

The geodesic distance was used for calculating travel time and the axial sound speed. The difference in range between the great circle and geodesic paths is not simply a constant percentage difference. Although it is a small effect, the lines extending farther south (S2,

S3) are disproportionately longer due to the larger radius of the earth in that region. This results in perceptibly longer differential axial travel times for the southern sources.

Horizontal refraction effects were not taken into account since they also do not have much effect on the relative results. The horizontal temperature gradients in this area are small (Munk *et al.*, 1988, Figure 7).

A.5. Equations for ranges and bearings

In the following file the path from shot 1 to hydrophone 23 is used as an example for calculating the great circle distance on a sphere and the geodesic distance on an ellipsoid. The basic equations used in a numerical integration routine for calculating the geodesic are also shown.

Filename: Range.mcd ORIGIN ≡ 1

For the source, shot 1: -latitude: $\phi 1 := (-34.488307)\cdot deg$

-longitude: $\lambda 1 := 17.648085 \cdot deg$

For the receiver, h23: -latitude: $\phi 2 := (-8.069861)\cdot deg$

-longitude: $\lambda 2 := -14.4193 \cdot deg$

Distances on a Spherical Earth Correct distance is 4393676

For the spherical model the distance between two points is:

$r := 6371000$

$\Delta\lambda := \lambda 2 - \lambda 1$

$S := r\cdot acos(sin(\phi 1)\cdot sin(\phi 2) + cos(\phi 1)\cdot cos(\phi 2)\cdot cos(\Delta\lambda))$

$S = 4397906$ Calculated great circle distance

$$\alpha_{21} := \pi - asin\left(sin\left(\phi 1 + \frac{\pi}{2}\right)\cdot\frac{sin(-\Delta\lambda)}{sin\left(\frac{S}{r}\right)}\right) \qquad \alpha_{21} = 136.59\cdot deg$$

Distances on Ellipsoidal Earth

The WGS-84 ellipsoid is defined by :

- semi-major axis: $a := 6378137$

- eccentricity $e := 0.081819191$

Appendix: Calculations and Processing

Geodesics: Gauss Mid-latitude formula:

Reference: Alfred Leick, GPS Satellite Surveying, Second Edition, p. 456-457, John Wiley and sons, 1995.

$\phi := \frac{\phi 1 + \phi 2}{2}$ $\eta := \sqrt{\frac{e^2}{1-e^2}\cdot\cos(\phi)^2}$ $V := \sqrt{1+\eta^2}$

$N := \frac{a}{\sqrt{1-e^2\cdot\sin(\phi)^2}}$ Radius of curvature in the prime vertical: $N = 6380950.598$

$M := \frac{a\cdot(1-e^2)}{\sqrt{(1-e^2\cdot\sin(\phi)^2)^3}}$ Radius of curvature in the prime vertical: $M = 6343827.313$

$\Delta\lambda := \lambda 2 - \lambda 1$ $\Delta\phi := \phi 2 - \phi 1$ $t := \tan(\phi)$

$Ssin\alpha := N\cdot\Delta\lambda\cdot\cos(\phi)\cdot\left(1 - \frac{1}{24}\cdot\Delta\lambda^2\cdot\sin(\phi)^2 + \frac{1+\eta^2-9\cdot\eta^2\cdot t^2}{24\cdot V^4}\cdot\Delta\phi^2\right)$

$Scos\alpha := M\cdot\Delta\phi\cdot\cos\left(\frac{\Delta\lambda}{2}\right)\cdot\left[1 + \frac{1-2\cdot\eta^2}{24}\cdot\Delta\lambda^2\cdot\cos(\phi)^2 + \frac{\eta^2\cdot(1-t^2)}{8\cdot V^4}\cdot\Delta\phi^2\right]$ $\phi = -21.28\cdot deg$

$\Delta\alpha := \Delta\lambda\cdot\sin(\phi)\cdot\left(1 + \frac{1+\eta^2}{12}\cdot\Delta\lambda^2\cdot\cos(\phi)^2 + \frac{3+8\cdot\eta^2}{24\cdot V^4}\cdot\Delta\phi^2\right)$ Convergence of meridians

$\alpha := \operatorname{atan}\left(\frac{Ssin\alpha}{Scos\alpha}\right)$ $\Delta\alpha = 12.21\cdot deg$

The distance from point 1 to point 2 is

$S := \sqrt{Ssin\alpha^2 + Scos\alpha^2}$ $S = 4394747$ Correct distance is 4393676

The azimuth from point 1 to point 2 is

$\alpha_{12} := \alpha - \frac{\Delta\alpha}{2}$ $\alpha_{12} = -55.80\cdot deg$

while the azimuth from point 2 to point 1 is:

$\alpha_{21} := \alpha + \frac{\Delta\alpha}{2} + \pi$ $\alpha_{21} = 136.42\cdot deg$

$\alpha_{21} - \frac{\Delta\alpha}{2} = 130.31\cdot deg$

Appendix: Calculations and Processing

Formulae for numerical integration :

Reference: G. Bomford, Geodesy, fourth edition, Clarendon Press, 1980, p. 648 - 64

$$N := \frac{a}{\sqrt{1 - e^2 \cdot \sin(\phi)^2}} \qquad M := \frac{a \cdot (1 - e^2)}{\sqrt{(1 - e^2 \cdot \sin(\phi)^2)^3}}$$

$$\frac{\delta\phi}{\delta S} = \frac{\cos(\alpha)}{M} \qquad \frac{\delta\lambda}{\delta S} = \frac{\sin(\alpha)}{N \cdot \cos(\phi)} \qquad \frac{\delta\phi}{\delta S} = \frac{\sin(\alpha) \cdot \tan(\phi)}{N}$$

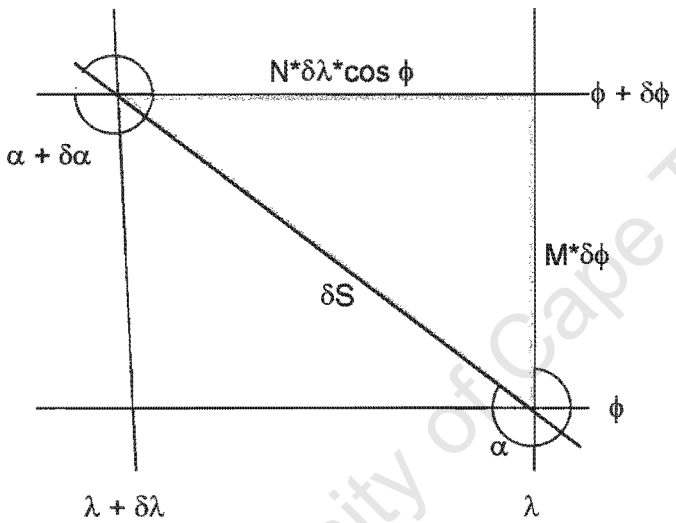

Figure A-3 Relationships for numerical integration

A.6. Geodesic calculations

Table A-2 shows the results from different calculations for the geodesic from shot 1 to hydrophone 23. The integration method is relatively simple, but 1000 steps from source to receiver and the other way round, gives a difference of 560 metres, indicating that the error is unacceptably large. Increasing the number of steps to 10000 reduces the difference to 46 metres. Increasing the number of steps by a further factor of 10 is probably impractical, so the Gaussian mid-latitude formula (shown in the calculation above) was used together with an optimisation routine to move the intermediate points for minimum range. This technique works because the Gaussian formula is accurate at shorter ranges but fails at longer ranges. Table A-2 shows that the method converges to a final answer with far fewer steps than the integration process. The calculated geodesic distances are given in Table A-3.

Method	Range
By integration, backwards, 1k steps:	4393946
By integration, forward, 1k steps:	4393386
Average of previous two distances	4393668
By integration, backwards, 10k steps:	4393655
By integration, forward, 10k steps:	4393701
Average of previous two distances	4393678
Gaussian mid-Latitude formula, 4 steps	4393682
Gaussian mid- Latitude formula, 10 steps	4393676.56
Gaussian mid- Latitude formula, 15 steps	4393676.42
Gaussian mid- Latitude formula, 20 steps	4393676.42

Table A-2 Geodesic distance of S1 to h23

A.7. Time measurements

The calculation for the trailing edge measurements is shown in Table A-3. The time to trailing edge was found from matching graphic displays of the time series.

	S1	S2	S3	S4	S5	S6	S7	S8
	Detonation Time (Least significant figures in seconds) T1							
	1994.0	3390.0	2730.0	1680.0	1920.0	2430.0	3360.0	360.0
	Recording start time (seconds) T2							
	4940.1	6285.1	5635.2	4590.0	4830.0	5335.0	6309.9	3305.1
	Time to trailing edge (seconds) T3							
h22	30.6	34.0	28.3	29.5	24.5	27.5	25.2	29.0
h23	23.4	27.2	21.5	22.5	17.0	21.2	18.0	21.4
h24	26.0	29.0	23.4	24.5	19.3	22.3	20.6	24.0
h29	22.7	26.0	20.0	22.0	16.0	19.0	17.3	20.5
h30	19.8	24.0	18.2	19.5	13.5	16.0	14.5	17.8
	Total travel time (seconds) = (T2 + T3 - T1)							
h22	2976.7	2929.1	2933.5	2939.5	2934.5	2932.5	2975.1	2974.1
h23	2969.5	2922.3	2926.7	2932.5	2927.0	2926.2	2967.9	2966.5
h24	2972.1	2924.1	2928.6	2934.5	2929.3	2927.3	2970.5	2969.1
h29	2968.8	2921.1	2925.2	2932.0	2926.0	2924.0	2967.2	2965.6
h30	2965.9	2919.1	2923.4	2929.5	2923.5	2921.0	2964.4	2962.9
	Range (Geodesic distance)							
h22	4,404.1	4,337.7	4,345.6	4,354.0	4,343.7	4,339.1	4,403.2	4,401.8
h23	4,393.7	4,327.4	4,335.3	4,343.6	4,333.3	4,328.7	4,392.7	4,391.3
h24	4,396.9	4,330.5	4,338.4	4,346.8	4,336.5	4,331.9	4,395.9	4,394.5
h29	4,391.8	4,326.8	4,334.2	4,342.0	4,331.3	4,326.7	4,390.9	4,389.5
h30	4,388.3	4,323.2	4,330.7	4,338.6	4,327.8	4,323.2	4,387.4	4,386.0
	Travel time compared to predicted axial travel time.							
h22	0.97	-1.83	-2.77	-2.38	-0.47	0.63	0.01	-0.09
h23	0.82	**-1.65**	-2.57	-2.35	-0.91	1.39	-0.14	-0.64
h24	1.26	-1.96	-2.80	-2.50	-0.78	0.33	0.29	-0.20
h29	1.39	-2.47	-3.36	-1.79	-0.54	0.56	0.43	-0.27
h30	**0.82**	-2.02	**-2.76**	**-1.93**	**-0.72**	**-0.12**	**-0.04**	**-0.64**

Table A-3 Times and distances

A.8. Calculating source depth from bottom echo arrival time

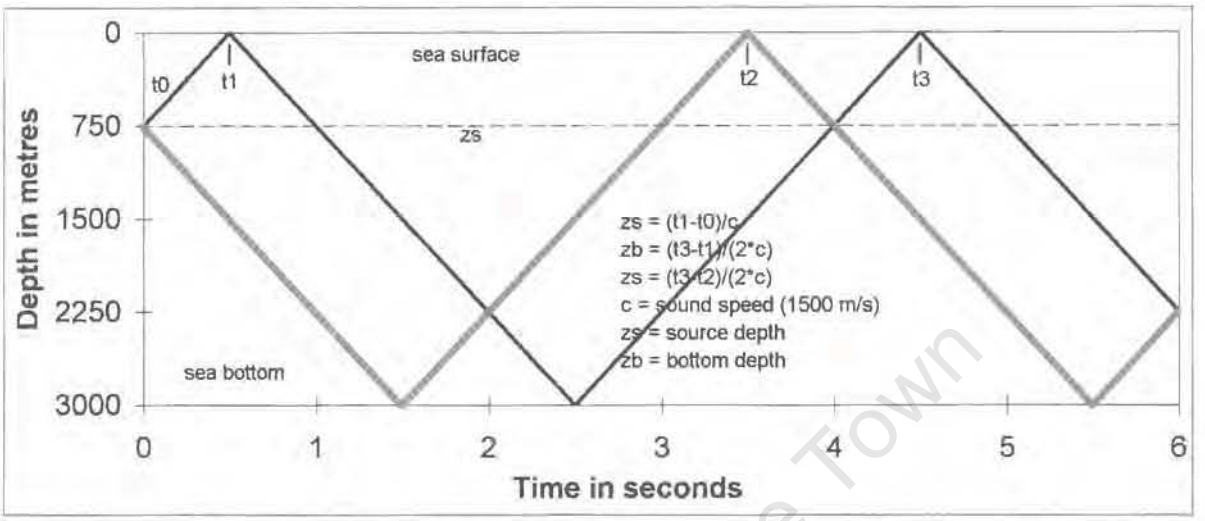

Figure A-4 Source depth as function of arrival time delays

The time relations and equations are shown in Figure A-4. The recording was made with a hydrophone about 10 metres below the surface. This small offset is not taken into account in the equations. The ignition time, t0, was not recorded, so the source depth was calculated from the difference between t3 and t2. The time differences (t3-t2, t3-t1) used for the source and bottom depth calculations of Table 1-1 are shown in Figure 2-6.

A.9. Bubble pulse frequencies

The time record, spectrum, and cepstrum of shot S3 are shown in the file below. The probable depth of the explosion is calculated from the frequency of the first bubble pulse using Equation 1-1. The second bubble pulse frequency is also indicated. This calculation is shown as an example of similar calculations for all the shots and the hydrophones with better signal-to-noise ratios. The first two bubble frequencies are not always readily discernible from a series of frequencies found in the cepstrum. This confusion of frequencies may be due to the bubble being non-spherical, unlike the assumption in the theory for deriving the frequencies. For producing spherical bubbles, the charge should ideally be spherical. Unfortunately, the charges used were cylindrical with length to diameter ratios of not less than three to1.

Appendix: Calculations and Processing

Filename Cepstrum3.mcd

The buit-in Mathcad function,cepstrum(x), is the inverse fft of the log of the magnitude of the fft of x, i.e. cepstrum(x) = $\text{icfft}\left(\overrightarrow{\log(|\,Sf\,|)}\right)$, where Sf = cfft(x). The cepstrum is usually taken to be the inverse fft of the log of the square of the fft of x, but the Mathcad definition of the function has the advantage of retaining the sign of the function, i.e. the negative peak are displayed as such, while squaring the function results in negative peaks becoming positive. The Mathcad function is used in the calculation below.

Find the spectrum modulation frequency ~ Bubble pulse frequency by taking the cepstrum of the signals.

ORIGIN := 1 fs = sampling frequency

fs := 1000 m := 7.99 Specify the sampling frequency (fs) and mass of shot (m).

S3h5 := READPRN("c:\user\records\dglitch\S3h5df") Read data file

S3 := submatrix(S3h5, 10500, 20500, 1, 1) Select the part of the signal with the best signal.

u := 1 .. rows(S3h5)

t := 1 .. rows(S3)

S3f := icfft(S3) i := 1 .. rows(S3f)

$f_i := \frac{i}{rows(S3f)} \cdot fs$ Determine the frequency bins for the spectrum

$ma := movavg\left(\overrightarrow{|\,S3f\,|}, 20\right)$ Take the moving average over 20 samples of the spectrum

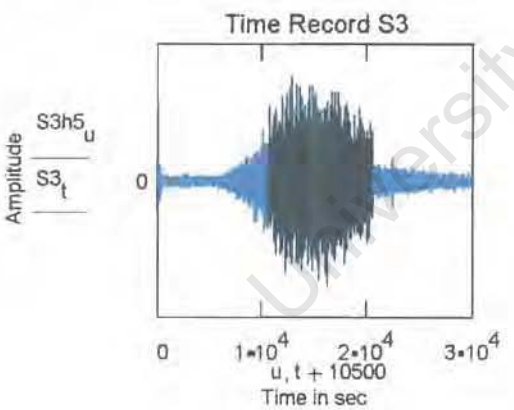

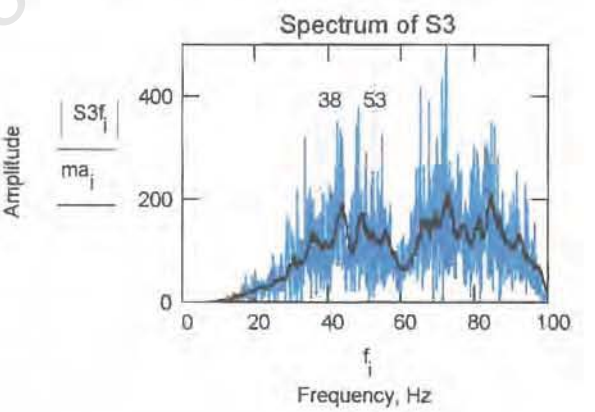

Appendix: Calculations and Processing

cep := cepstrum(S3) Take the cepstrum of the signal

t := 1.. 100

pb1 := 26.5

$fb1 := \frac{1000}{pb1}$

fb1 = 37.7

$z := \left(2.11 \cdot m^{\frac{1}{3}} \cdot fb1\right)^{\frac{6}{5}} - 10$

z = 428.8

pb2 := 19 $fb2 := \frac{1000}{pb2}$ fb2 = 52.632

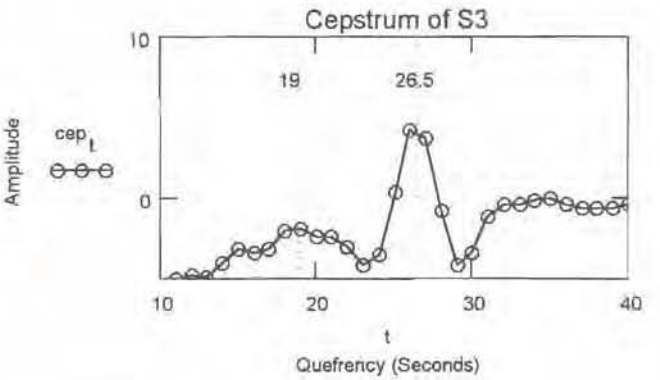

The first and second bubble pulses are at 37.7 and 52.6 Hz respectively.

A.10. Display format for arrival waveforms

The time series recorded for every shot at each hydrophone lasts 120 seconds with 1000 samples per second. Less than 20 seconds of the time record contains shot information. One of the first steps in processing was to truncate the record to 40 seconds. Further reduction of the amount of data consisted of first taking the moving maximum and moving minimum of each signal and then sub-sampling by a factor of 100. No averaging has been used on the envelope, since the averaging would reduce the peak amplitudes of the best signals. Although the envelope appears to be noisy, this is the character of the source energy and averaging is not justified. The moving maximum technique results in a graph that is very similar to that of a chart recorder. There is still an element of subjectivity in this processing since the running window time for the maximum has to be chosen. However, this time is fairly well dictated by the length of display. The Mathcad file below shows the processing of one of the arrival waveforms.

Appendix: Calculations and Processing

Filename EnvS1h5.mcd
Process the deglitched and filtered data to obtain a sub-sampled envelope of the arrival waveform for display in Excel, i.e. reduce the total number of samples from 40000 to 800 while preserving the maximum and minimum values of the original.

$ORIGIN \equiv 1 \quad t := 1 .. 40000 \qquad Time_t := \frac{t}{1000}$

Functions to take the running max and min of the matrix 'z' over 'w' samples and a function tc subsample the matrix 'V' by 'n' samples, starting at 'offset' samples:

```
movmax(z, w) :=
    break if (w < 1) + (w > length(z))
    z if w = 1
    if (w > 1)·(w ≤ length(z))
        hw ← floor(w / 2)
        I ← ORIGIN
        for i ∈ I .. I + hw - 1
            az_i ← max(submatrix(z, I, w, 1, 1))
        for i ∈ I + hw .. last(z) - hw
            az_i ← max(submatrix(z, i - hw, i + hw, 1, 1))
        for i ∈ last(z) - hw + 1 .. last(z)
            az_i ← max(submatrix(z, last(z) - hw + 1, last(z), 1, 1))
        az
```

Appendix: Calculations and Processing

$$\text{movmin}(z,w) := \left|\begin{array}{l} \text{break if } (w<1)+(w>\text{length}(z)) \\ z \text{ if } w=1 \\ \text{if } (w>1)\cdot(w\le\text{length}(z)) \\ \quad \left|\begin{array}{l} hw \leftarrow \text{floor}\left(\frac{w}{2}\right) \\ I \leftarrow \text{ORIGIN} \\ \text{for } i \in I..I+hw-1 \\ \quad az_i \leftarrow \min(\text{submatrix}(z,I,w,1,1)) \\ \text{for } i \in I+hw..\text{last}(z)-hw \\ \quad az_i \leftarrow \min(\text{submatrix}(z,i-hw,i+hw,1,1)) \\ \text{for } i \in \text{last}(z)-hw+1..\text{last}(z) \\ \quad az_i \leftarrow \min(\text{submatrix}(z,\text{last}(z)-hw+1,\text{last}(z),1,1)) \\ az \end{array}\right. \end{array}\right.$$

$$\text{subsample}(V,n,\text{offset}) := \left|\begin{array}{l} \text{break if } (n<1)+(n>\text{length}(V)) \\ V \text{ if } n=1 \\ \text{for } z \in 1..\text{floor}\left(\frac{\text{last}(V)-\text{offset}}{n}\right) \\ \quad Z_z \leftarrow V_{(\text{offset}+z\cdot n)} \\ Z \end{array}\right.$$

h5v := READPRN("c:\user\Records\Dglitch\S7h5df")

Take the moving maximum, moving minimum and subsample to reduce the vector length by a factor of n.

Mxh5 := movmax(h5v, 100)

Mnh5 := movmin(h5v, 100)

Subsample the moving max and moving min and time vectors. Combine the new max and min vectors each with time vector to form two matrices with time in first column and max or min in second column.

$Mxsh5^{<1>}$:= subsample(Time, 100, 0)

$Mxsh5^{<2>}$:= subsample(Mxh5, 100, 0)

$Mnsh5^{\langle 1 \rangle} := subsample(Time, 100, 50)$

$Mnsh5^{\langle 2 \rangle} := subsample(Mnh5, 100, 50)$

Combine the matrices (time series) for the max and min and sort to produce a time series of maxima and minima ordered in time.

$S7h30 := csort(stack(Mxsh5, Mnsh5), 1)$

$rows(S7h30) = 799$

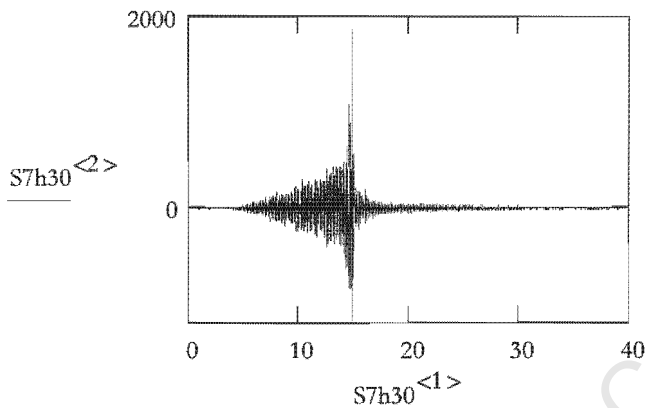

A.11. Removing radar glitches and filtering

The large amplitude, short duration spikes caused by radar interference with signal records transmitted by radio can be seen in Figure 2-8. Closer inspection of these spikes reveals that individual spikes usually consist of a single point of large amplitude amongst a series of low amplitude points. These "glitches" can be removed by assigning a mean value between preceding and succeeding values to the anomalous point.

Doing this requires a set of normal values to be defined and a threshold beyond which the point is deemed a glitch. The normal background was defined as a running median of 21 values and the threshold was defined as a set ratio of the point to the running median value. The best set point was found by trial and error for each recording.

The de-glitching procedure is effective in removing the more obvious large amplitude, short duration errors in the data. However, some noise and errors will still be present. For example, some of signal recordings contain a low frequency voltage offset (as if the amplifier at the receiver had a very long settling time). Very low and high frequency signals in the

recording are unlikely to emanate from the shot over 4000 kilometres away since they would not propagate over such long ranges. To minimise these out of band components, the signals were passed through third order Butterworth high- and low-pass filters set to 15 and 150 Hz, respectively.

A.12. Normal mode – Calculating eigenvalues and eigenvectors

The normal mode equations apply only to range-invariant conditions. The calculation consists of two steps: firstly, to calculate the relevant eigenvalues and eigenvectors and secondly, to apply Equation 2-4 to the point of interest.

Finding the wavenumber is really finding the solution to the sound propagation equation. This is discussed in Computational Ocean Acoustics, section 5.7.1 and appendix A.12, and by Porter (1984). A program demonstrating the implementation of the normal mode equations in Matlab is given by Porter on the website "Ocean Acoustics Library – http://oalib.njit.edu". This Matlab file is shown below:


```
% ******************************************************
% Modes
% ******************************************************
% *** set up Munk SSP ***
zs  = 1000.0;                % source depth
f   = 50; omega = 2 * pi * f% frequency in Hertz
eps = 0.00737; c0  = 1500;
d   = 5000;          % bottom depth
nz  = 501;           % number of finite-difference points
h   = d / nz; h2  = h * h;% mesh spacing
z   = linspace( 0, d, nz );% grid coordinates
x = 2 * ( z - 1300 ) / 1300;
c = c0 * ( 1 + eps * ( x - 1 + exp( -x ) ) );
plot( z, c ); view( 90, 90 );
xlabel( 'Depth (m)' ); ylabel( 'Sound Speed (m/s)' )
pause
% ******************************************************
% set up finite difference matrix
% ******************************************************
v = omega * omega ./ ( c .* c );
D = sparse( 1:nz, 1:nz  , -2*ones( 1, nz   ) / h2 + v, nz, nz, nz   );
E = sparse( 2:nz, 1:nz-1,    ones( 1, nz-1 ) / h2,     nz, nz, nz-1 );
A = D + E + E';
% ******************************************************
% Find eigenvalues and eigenvectors
% ******************************************************
```

```
m = 50              % number of modes to use
k2 = eig( A );
k2 = flipud( sort( k2 ) );
k2 = k2( 1:m );
k = sqrt( k2 );
% inverse iteration for eigenfunctions
for ii = 1:m
  psi(:,ii) = ( A - k2( ii ) * speye( size( A ) ) ) \ ones( nz, 1 );
%  psi(:,ii) = ( A - k2( ii ) * speye( size( A ) ) ) \ psi(:,ii);% extra iteration
  psi(:,ii) = psi(:,ii) / norm( psi(:,ii) );% normalize
end
% ******************************************************
% plot the modes
% ******************************************************
pcolor( 1:m, z, psi ); shading interp; colormap(gray); colorbar; view( 0, -90 );
title('Mode shapes for the Munk profile')
xlabel( 'Mode' ); ylabel( 'Depth (m)' )
pause
plot( z, psi( :, 1:25:m ) ); view( 90, 90 );
xlabel( 'Depth (m)' ); ylabel( 'Mode shape' )
pause
% --- weigh modes by mode excitation
isd = zs / d * (nz-1);          % index of source depth
a = psi( isd, : );
psi = psi * diag( a, 0 );% scale modes by a
% --- show which modes are excited
pcolor( 1:m, z, psi ); shading interp; colormap(gray); colorbar;
title('Mode intensities for the Munk profile')
xlabel( 'Mode' ); ylabel( 'Depth (m)' )
view( 0, -90 );      % flip plot so that z-axis is pointing down
pause
% ******************************************************
% form pressure field
% ******************************************************
nr = 201;
r = linspace( 1000.0, 100000.0, nr ); % nr ranges to 100 km
phase = diag( 1.0 ./ sqrt( k ) ) * exp( i * k * r ) * diag( 1.0 ./ sqrt( r ) );
p = psi * phase;
tl = 20.0 * log10( abs( p ) );
pcolor( r, z(1:10:nz), tl( 1:10:nz,:) ); caxis( [ -100 -60 ] ); shading interp; colormap( gray );
colorbar; view( 0, -90 );
xlabel( 'Range (m)' ); ylabel( 'Depth (m)' );
title( 'Normal mode track intensity' )
```

The last figure in the file above is similar to Figures 3-15 and 3-16.

The calculation in the file above is sufficient for calculating intensity or attenuation. The calculation of arrival waveforms is more complicated. The arrival waveform consists of the

complex sum of the source waveforms where each waveform is carried by one mode. Furthermore, the source waveform must have a finite bandwidth. Instead of doing the above calculation for a single frequency, the source bandwidth must be sampled at a number of frequencies and the modes for each of these frequencies must be included in the complex sum. The way in which this is done is summarised in Equation 2-4.

Calculating the eigenvalue and eigenvectors is time consuming. In addition, the amount of data to be stored can become large. In the Matlab file shown below the calculation is done for 1201 values of frequency, 1000 water depths, and 100 modes. Storing this would require space for 120 million values, which is inconvenient, both in terms of the amount of data to be stored and the time taken to write this to disk. The file below calculates the values for one frequency, stores only a selected set of values (at the depths most likely to be used), and then continues to the next value. Since the whole process runs for about 30 hours on a Pentium II PC, interruptions are quite likely and the program allows calculations to be resumed from the last complete frequency calculated.


```
% Filename kucalc.m
% Calculate the k and psi values for FACT SSP and sea-floor at
10000 m.
% New Munk equation 21/9/98
% Calculates all 1601 values of k & u for f from 20 to 120.
% The spacing in frequency is 16 per Hz from 20 to 120 Hz.
% Run-time approx. 30 hr. Interrupted runs can be resumed using
FLast.

format long
B=578;                                  % Munk parameters
zs=-800;
epsi = 0.00289; ca  = 1482;    % Munk parameters
d   = -10000;                          % bottom depth
nz  = 1000;                          % number of finite-difference
points
h   = d / (nz);
h2  = h * h;                            % mesh spacing
z = linspace( 0, d, (nz));      % grid coordinates
x = 2*(z-zs)/B;
c=ca./sqrt(1-2*epsi*(exp(x)-x-1));
%Finite difference matrix
fmin=20;  %should be 20
fmax=120;  %should be 120 Next 95+1/16 to 120
fn=(fmax - fmin)*16 + 1;                        %Number of frequencies
f=linspace(fmin, fmax, fn);
Flast = 1027;       %Last frequency calculated in previous run
omega = 2*pi*f;
%plot( z, c ); view( 90, -90 );
```

```
%xlabel( 'Depth (m)','Fontsize',16 );
%ylabel( 'Sound Speed (m/s)','Fontsize',16 ),
%grid, set(gca, 'FontSize', 14, 'FontName','Arial','Fontweight',
'Bold');
load c:\user\prn1\z16k.prn ;              %Load existing files, if
required
load c:\user\prn1\z16u80.prn ;            %
%load c:\user\prn1\z16u75.prn ;            %
load c:\user\prn1\z16u70.prn ;            %
%load c:\user\prn1\z16u65.prn ;            %
load c:\user\prn1\z16u60.prn ;            %
%load c:\user\prn1\z16u55.prn ;            %
load c:\user\prn1\z16u50.prn ;            %
%load c:\user\prn1\z16u45.prn ;            %
load c:\user\prn1\z16u40.prn ;            %
%load c:\user\prn1\z16u35.prn ;            %
load c:\user\prn1\z16u30.prn ;            %
%load c:\user\prn1\z16u25.prn ;            %
load c:\user\prn1\z16u20.prn ;            %

%Loop calculation for different frequencies,
%containing inner loop for calculating mode parameters
%for different modes. Selected results are saved
%at the end of the frequency loop.
%The axes of psi refer to (depth, modes).
for  fi =Flast+1:fn  m = 100; %Set number of modes to be calculated
   v = omega(fi) .* omega(fi) ./ ( c .* c );  % Dot multiplication
   D = sparse( 1:nz, 1:nz  , -2*ones( 1, nz   ) / h2 + v, nz, nz,
nz   );
   E = sparse( 2:nz, 1:nz-1,    ones( 1, nz-1 ) / h2,     nz, nz,
nz-1 );
   A = D + E + E';
   %Find eigenvalues and eigenvectors
   k21 = eig( A );
   k22 = flipud( sort( k21 ) );
   k2m = k22( 1:m);
   z16k(1:m, fi) = sqrt(k22(1:m));
   %Inverse iteration for eigenfunctions:
   for ii = 1:m
      psi(:,ii) = ( A - k2m( ii ) * speye( size( A ) ) ) \ ones(
nz, 1 );
      psi(:,ii) = ( A - k2m( ii ) * speye( size( A ) ) ) \
psi(:,ii);
      psi(:, ii) = psi(:, ii) / norm(psi(:, ii));
      z16u80(ii,fi) = psi(80,ii);
      %u75(ii,fi) = psi(75,ii);
      z16u70(ii,fi) = psi(70,ii);
      %u65(ii,fi) = psi(65,ii);
      z16u60(ii,fi) = psi(60,ii);
      %u55(ii,fi) = psi(55,ii);
      z16u50(ii,fi) = psi(50,ii);
      %u45(ii,fi) = psi(45,ii);
      z16u40(ii,fi) = psi(40,ii);
      %u35(ii,fi) = psi(35,ii);
      z16u30(ii,fi) = psi(30,ii);
```

```
      %u25(ii,fi) = psi(25,ii);
      z16u20(ii,fi) = psi(20,ii);
   end
   fi
   save c:\user\prn1\z16k.prn z16k -ascii -double
save c:\user\prn1\z16u80.prn z16u80 -ascii -double
%save c:\user\prn1\z16u75.prn u75 -ascii -double
save c:\user\prn1\z16u70.prn z16u70 -ascii -double
%save c:\user\prn1\z16u65.prn u65 -ascii -double
save c:\user\prn1\z16u60.prn z16u60 -ascii -double
%save c:\user\prn1\z16u55.prn u55 -ascii -double
save c:\user\prn1\z16u50.prn z16u50 -ascii -double
%save c:\user\prn1\z16u45.prn u45 -ascii -double
save c:\user\prn1\z16u40.prn z16u40 -ascii -double
%save c:\user\prn1\z16u35.prn u35 -ascii -double
save c:\user\prn1\z16u30.prn z16u30 -ascii -double
%save c:\user\prn1\z16u25.prn u25 -ascii -double
save c:\user\prn1\z16u20.prn z16u20 -ascii -double
end
```

A.13. Source waveform

Synthesising the arrival waveform requires a source waveform. The waveform of an explosive source is rather unpredictable since it depends on factors that are difficult to quantify exactly, such as the exact composition and shape of the explosive (including the booster charge, if any), the ignition process, the characteristics of the container and the depth of the explosion. The source waveform is broadband while the propagation process preferentially strips high and low frequencies from the shot energy. The low frequencies are mainly attenuated due to the propagation channel not being sufficiently deep to support very long wavelengths, while the high frequencies are more subject to viscosity and chemical absorption losses. The source waveform for synthesising arrival waveforms in equation 3-4 (normal mode synthesis) and equation 5-1 (ray trace synthesis) was derived from the waveform recorded at the source (Figure 2-6) by taking the first 70 milliseconds of the waveform and filtering out high and low frequency components.

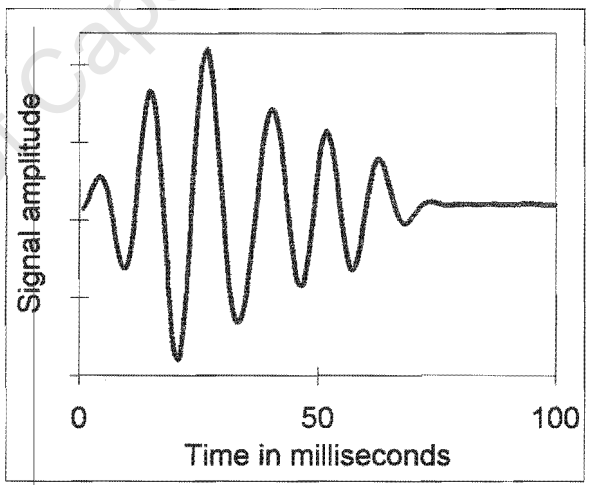

Figure A-5 Source waveform derived from recording at source of shot 1.

Appendix: Calculations and Processing

A.14. Synthesising normal mode arrival waveforms

Filename demo-nm.mcd
Synthesise arrival waveforms using the normal mode equations. Use the waveform from the source recording as the start. Use a 16 second window to accommodate the dispersion in the signal over 4.3 Megametres. The sampling frequency is 16 samples per Hz so as to get 16 seconds time record out of the transform.
k and psi values are pre-calculated for 20 to 120 Hz -- 1601 values.

ORIGIN≡ 1

$R := 4.29946 \cdot 10^6$ $\frac{R}{1482} = 2901.120$ Range in metres and axial travel time in seconds

Read the source signal in the time domain and convert to the frequency spectrum. This file comes from S1s-v99.mcd.

s := READPRN("c:\user\signal\S1s-v99.PRN")

last(s) = 16001 i := 1 .. last(s) max(s) = 1

$f_i := \frac{i}{16}$ Specify the bins in the frequency domain.

S := cfft(s) last(S) = 16001 $t_i := \frac{i}{last(s)} \cdot 16$

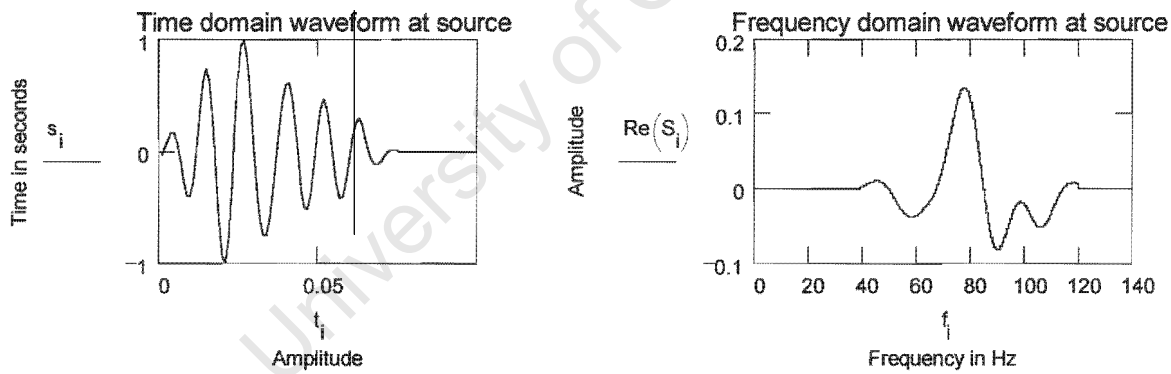

Read the pre-computed k-values in (16 * 100 +1) columns which cover the source frequency band from 20 to 120 Hz at 1/16 Hz values and combine these values of k with the appropriate values of [f]. The rows represent the k-values of modes from 1 to 84.
The values of k and psi were computed for a bottom depth of 3500 metres. Computation was done in file kucalc7.m dated 98/02/25. Create zero value matrices to pad the matrix of k-values in place of the frequencies below 20 and above 120 Hz.

kr := READPRN("c:\user\Prn1\v7k.prn") rows(kr) = 84 cols(kr) = 1601

r := 1 .. 84 c := 1 .. 320

$k0_{r,c} := 0$ rows(k0) = 84 cols(k0) = 320 ORIGIN = 1

k := augment(k0 , kr) rows(k) = 84 cols(k) = 1921

m := 1 .. rows(k) n := 1 .. cols(k) $f_n := \frac{n}{16}$

Appendix: Calculations and Processing

Read and associate psi values for depth of 800 m. Each file contains a 84 by 1601 matrix of psi values representing the psi value for 84 modes and 1601 frequencies.

u80 := READPRN("c:\user\Prn1\v7u80.prn")

rows(u80) = 84 cols(u80) = 1601

r := 1.. 84 c := 1.. 320

$k0_{r,c} := 0$ rows(k0) = 84 cols(k0) = 320

ψ80 := augment(k0, u80)

rows(ψ80) = 84 cols(ψ80) = 1921

m := 1.. rows(k) $f_{1280} = 80$

Source waveform, k & psi values

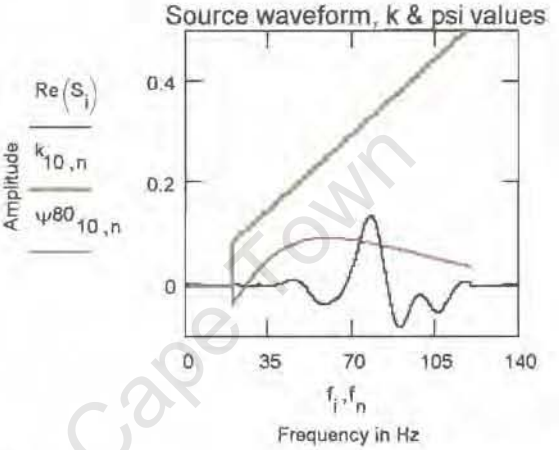

Write the general equation as a sum of modes, neglecting the 1/R factor::

$$sum_n := e^{i\frac{\pi}{4}} \cdot \sum_{m=1}^{80} \left(\psi80_{m,n} \cdot \psi80_{m,n}\right) \cdot \sqrt{\frac{2\cdot\pi}{k_{m,n}}} \cdot e^{i \cdot k_{m,n} \cdot R}$$

rows(sum) = 1921

cols(sum) = 1

$SE_n := S_n \cdot sum_n$ rows(SE) = 1921 cols(SE) = 1

r := 1.. 16001 − rows(SE)

Restore the frequency domain vector to its full length of 16k by padding with the zeros lost during multiplication.

$Pad_r := 0$

SE16k := stack(SE, Pad) rows(SE16k) = 16001

sig8 := recenter(icfft(SE16k))

max(|sig8|) = 0.101941

max8 := max(|sig8|)

r := 1.. rows(sig8) − 1

$sig8_r := \frac{|sig8_r|}{max8}$

rows(sig8) = 16001

$Time_i := t_i - 13.2$

Waveforms at receiver

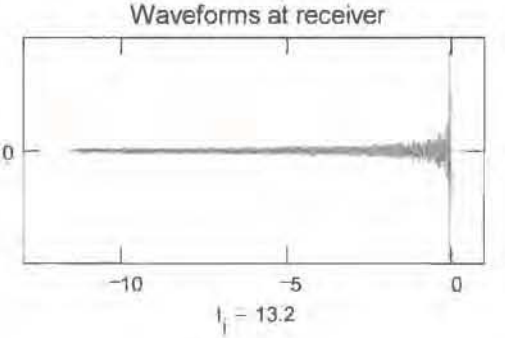

$NM^{\langle 1 \rangle}$:= Time $NM^{\langle 2 \rangle}$:= sig8

WRITEPRN("c:\User\Records\Envelope\demo-nm.prn") := NM

A.15. Ray trace code in Matlab

The Matlab file below was posted on the website http://oalib.njit.edu by Michael B. Porter as a demonstration of a simple ray tracing program and has been used in a modified form in this thesis to produce Figures 3-2 and 3-5.

```
% ******************************************************
% Rays
% Michael B. Porter
% ******************************************************

% The equations we're solving are:
% r'    = c rho
% z'    = c zeta
% rho'  = -c_r / c2
% zeta' = -c_z / c2
send = 100000;% arclength for rays
ntheta   = 31;% number of rays
theta = pi / 180 * linspace( -14.0, 14.0, ntheta );
zs = 1000.0;  % source depth
c0 = 1501.4;  % sound speed at source depth
for ith = 1:ntheta% loop over take-off angle
   % ray initial condition:
   x0 = [ 0.0   zs   cos( theta( ith ) ) / c0   sin( theta( ith ) ) / c0 ];
   % now solve the DE to trace the ray
   [ s, x ] = ode45( 'rayf', 0.0, send, x0 );
   plot( x( : , 1 ), x( : , 2 ) );
   hold on;   % hold the old rays on screen when plotting new rays
end
hold off;
% label the plot
xlabel( 'Range (m)' )
ylabel( 'Depth (m)' )
view( 0, -90 );% flip plot so that z-axis is pointing down
The sub-routine for solving the differential equation is given in the file
"Rayf.m" below:
function xdot = f( s, x )
% Munk sound speed profile
eps = 0.003;
c0  = 1482;
z   = x( 2 );
xt  = 2 * ( z - 800 ) / 576;
c   = c0 * ( 1 + eps * ( xt - 1 + exp( -xt ) ) );
c2  = c^2;
% we also need derivatives of sound speed
dxtdz = 2 / 576;
cz= c0 * eps * dxtdz * ( 1 - exp( -xt ) );
cr = 0;
% here's the RHS
xdot = zeros( 4, 1 );
xdot( 1 ) = c * x( 3 );
xdot( 2 ) = c * x( 4 );
xdot( 3 ) = -cr / c2;
xdot( 4 ) = -cz / c2;
```

Appendix: Calculations and Processing

A.16. Synthesising and comparing arrival waveforms

File name demo-rt.mcd.
1. Synthesise ray trace waveforms for 3k5 m depth seafloor..
2. Import normal mode waveform from Shn80.prn
3. Compare these waveforms.

Ray Trace synthesis:
Read the source signal in the time domain and convert to the frequency spectrum.
This file comes from S1s-v99.mcd

ORIGIN ≡ 1

S1a := READPRN("c:\user\signal\S1s-v99.PRN")

t1 := 1 .. rows(S1a) rows(S1a) = 16001

max(S1a) = 1

$$S1 := \frac{submatrix(S1a, 1, 16000, 1, 1)}{max(S1a)}$$

t := 1 .. 100 rows(S1) = 16000

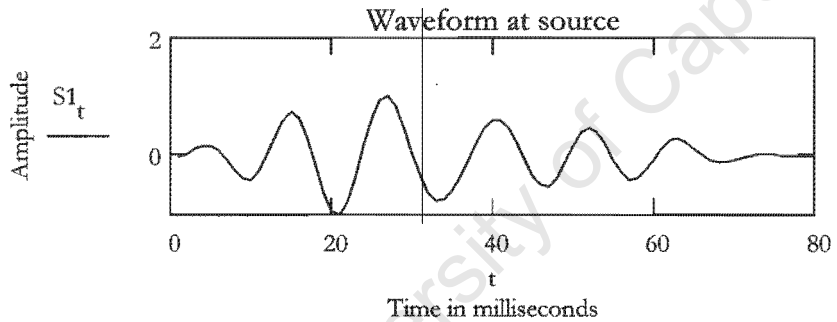

fs := 1000 Sampling frequency

S := S1 n := rows(S) rows(S) = 16000

k := 1 .. last(S) last(S) = 16000

Sf := cfft(S) $f_k := \frac{k}{n} \cdot fs$

Appendix: Calculations and Processing

$s := icfft((Sf))$

$binwidth := \frac{fs}{n}$

$binwidth = 0.0625$

$t_k := \frac{k}{n} \cdot \frac{1}{binwidth}$

$length(s) = 16000$

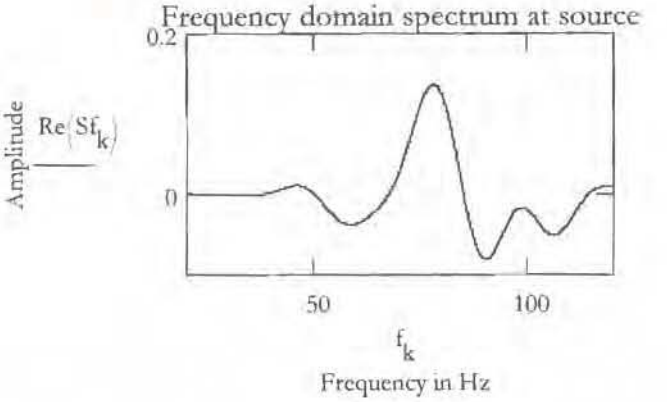

Ray trace data table from eigen3k5.xls

$M := READPRN("C:\User\RayWHOI\eig3k5p.prn")$ $rows(M) = 190$ $cols(M) = 4$

Columns are Launch angle, Time, Amplitude & No of turning points

$n := 1 .. rows(M)$

$\tau := M^{<2>} - max(M^{<2>}) - 4$ $min(M^{<2>}) = 2889.21$

$max(M^{<2>}) = 2901.12$

$a_n := (M^{<3>})_n$

$s := M^{<4>}$

$n := 1 .. rows(M)$

$ta := \frac{4300000}{1482}$

$ta = 2901.484$

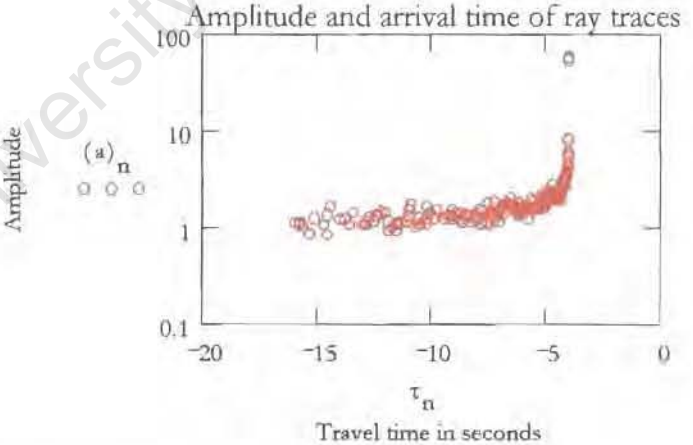

Equation for synthesising ray trace arrival waveforms:

$$RT_k := \left[\sum_{n=1}^{rows(M)} \left(a_n \cdot Sf_k \cdot e^{j \cdot 2 \cdot \pi \cdot f_k \cdot \tau_n} \cdot e^{j \cdot s_n \cdot \frac{\pi}{2}} \right) \right]$$

Appendix: Calculations and Processing

Take the inverse Fourier transform to get into the time domain.

$RTt := (icfft(RT))$ $\quad rows(RTt) = 16000$

$maxS := \overrightarrow{max(|RTt|)}$ $\quad maxS = 43.55$

$RTtn_k := \frac{|RTt_k|}{maxS}$ $\quad max(RTtn) = 1$ Normalise the signal amplitude.

$NM := READPRN("C:\USER\RECORDS\ENVELOPE\demo-nm.prn")$

$NM^{<2>} := \overrightarrow{|NM^{<2>}|}$ $\quad rows(NM) = 16001$

$max(NM^{<2>}) = 1$ $\quad cols(NM) = 2$

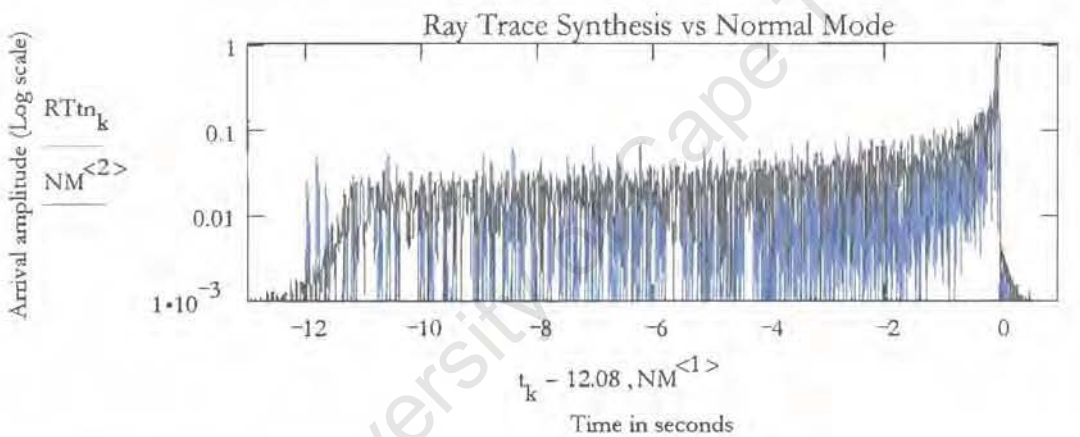

$rows(RTtn) = 16000$ $\quad rows(NM) = 16001$ $\quad t_1 = 0.001$

$(NM^{<1>})_1 = -13.199$

Shift the RT vector to synchronise by padding at the start

$p := 1..1120$

$Pad_p := 0$

$RT1 := stack(Pad, RTtn)$

$t := 1..rows(RT)$ $\quad T_t := \frac{t - 13140}{1000}$ $\quad T_1 = -13.139$

Take the moving max and subsample to reduce "noise" and vector size

Appendix: Calculations and Processing

```
movmax(z, w) := | break if (w < 1) + (w > length(z))
                | z if w = 1
                | if (w > 1)·(w ≤ length(z))
                |   hw ← floor(w / 2)
                |   I ← ORIGIN
                |   for i ∈ I .. I + hw − 1
                |     az_i ← max(submatrix(z, I, w, 1, 1))
                |   for i ∈ I + hw .. last(z) − hw
                |     az_i ← max(submatrix(z, i − hw, i + hw, 1, 1))
                |   for i ∈ last(z) − hw + 1 .. last(z)
                |     az_i ← max(submatrix(z, last(z) − hw + 1, last(z), 1, 1))
                |   az
```

```
subsample(V, n, offset) := [ | break if (n < 1) + (n > length(V))
                             | V if n = 1
                             | for z ∈ 1 .. floor((last(V) − offset) / n)
                             |   Z_z ← V_(offset + z·n)
                             | Z ]
```

$V := RT1$ $\quad rows(V) = 17120$ $\quad rows(T) = 16000$

$Vm := \overrightarrow{|V|}$ $\quad rows(Vm) = 17120$ $\quad cols(Vm) = 1$

$Vmm := movmax(Vm, 20)$

Subsample to reduce the vector length by a factor of n.

$RT := subsample(Vmm, 20, 0)$

$T := subsample((T), 20, 0)$

$rows(RT) = 856$ $\quad rows(T) = 800$

Reduce the number of data points for the normal mode synthesised signal:

$Vmm := movmax(NM^{<2>}, 20)$

$NM := subsample(Vmm, 20, 0)$ $\quad rows(NM) = 800$

Appendix: Calculations and Processing

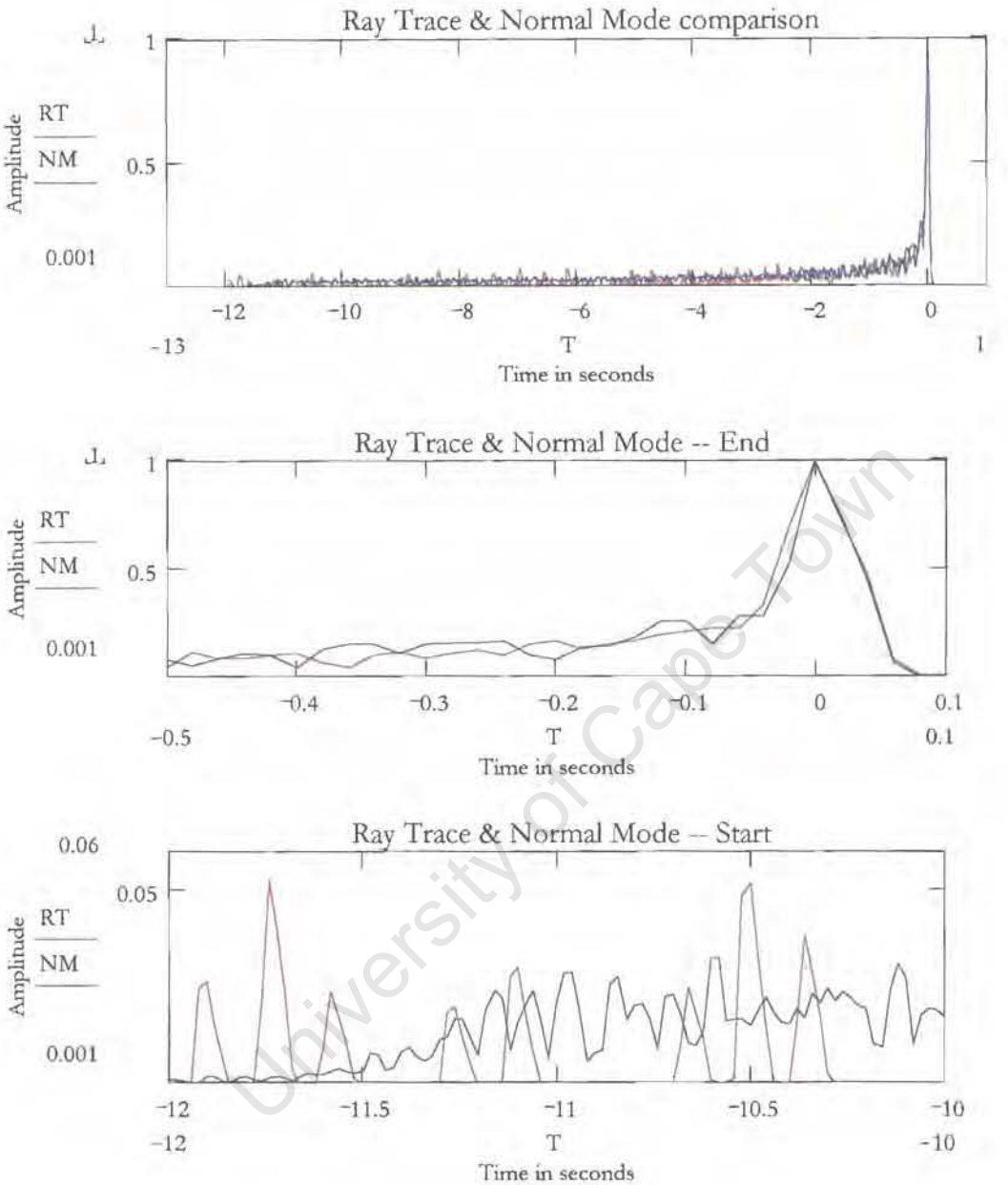

The three figures above show that the ray trace and normal mode synthesised arrival waveforms are fairly similar. The peak at the termination of the signal matches closely while the earlier arrivals are somewhat dissimilar. The ray trace synthesis for the earlier arrivals shows a recurring triplet of peaks that does not occur in the normal mode synthesis. This triplet is a consequence of the ray arrival pattern for an on-axis source. In the later part of the signal, the arrival density becomes greater and the triplets are no longer distinguishable.

The normal mode synthesis should produce the same waveform, provided a sufficiently large number of accurately computed modes are computed. The disparity in waveforms for the early arrivals indicates that the number of modes or the accuracy of the calculation is not great enough.

In normal mode synthesis the final peak is carried almost entirely by the first mode, while the early arrivals are the algebraic sums of a large number of modes. In the ray trace synthesis, the early arrivals are formed from the arrival of a single ray (or two rays arriving simultaneously, in the case of the middle peak of the triplet) while the final peak is the sum of a large number of closely spaced ray arrivals. Some underwater sound propagation models make use of these properties to reduce the amount of computation required by switching between normal mode and ray trace synthesis for calculating different parts of the arrival waveform.

A.17. Detecting shot path and contour line intersections for track profiles

The contour lines for a specific area can be obtained from the GEBCO CD-ROM. They come as text files containing the coordinates of the points at that depth. This list of points is then written in rows. Each row contains the 'x' and 'y' coordinates for one point. Successive rows contain adjacent points. The starting point of a closed contour is repeated in the last row as the end point.

The (x, y) coordinates are transformed to range and bearing coordinates with respect to a specific point – for example, hydrophone 30. This gives a series of rows, each containing the range and bearing of the point on that line relative to hydrophone 30. Now, to test whether, for example, the track of shot 1 to hydrophone 30 intersects the contour line, the bearing of shot 1 relative to hydrophone 30 is compared to the column of point bearings.

An intersection of the track path and the contour line is equivalent to the track line passing between two points on the contour lines. It follows that, somewhere down the column, the point bearing will switch from greater than, to smaller than, the bearing of the shot (or from smaller to greater). This switch can be tested for in a spreadsheet or in a matrix. The intersections detected in this way can then be used to compile the track profiles (Figures 4-4 to 4-8).

A.18. Compiling azimuth views

The (x, y) coordinates of the points are again written as range and bearing coordinates with respect to the point for which the azimuth view is being compiled. If there is a closed contour line within the maximum and minimum angles of interest, the maximum and minimum values of bearing angle define the width of the obstruction at that depth.

There is no particular difficulty in this procedure – the problem with both this procedure and the one in the previous section lies in selecting or filtering the correct points amongst some ten thousand incorrect ones.

References

References

Arons, A. B., (May 1948)
Secondary Pressure Pulses Due to Gas Globe Oscillation in Underwater Explosions. II. Selection of Adiabatic Parameters in the Theory of Oscillations
J. Acoust. Soc. Am., Vol. **20** No 3, p 277-282.

Baggeroer, A., and W. Munk, (September 1989)
The Heard Island feasibility test
Phys. Today **45** p 22-30

Bold, Gary E.J and Theodore G. Birdsall, (August 1986)
A top-down philosophy for accurate numerical ray tracing
J. Acoust. Soc. Am., Vol. **80** (2), p. 656-660.

Bowlin, Jim, (1994)
Ray Version 1.47, April 25, 1994, Copyright (C) 1992-1994,
Available from Ocean Acoustics Library — http://oalib.njit.edu
Woods Hole Oceanographic Institution

Brundrit, G. B., and L. Krige (October 1994)
Heard Island signals through the Agulhas retroflection region
J. Acoust. Soc. Am., Vol. **96** (4), p. 2464-2468,

Bryan, G. M.; M. Truchan, and J. I. Ewing, (March 1963)
Long Range SOFAR Studies in the South Atlantic Ocean
J. Acoust. Soc. Am., Vol. **35** No 3, p 273-278.

Chapman, N. Ross, and Gordon R. Ebbeson (June 1983)
Acoustic shadowing by an isolated seamount
J. Acoust. Soc. Am., Vol. **73** (6), p. 1979-1984.

References

Collins, John A.; James E. Broda, G. M. Purdy, Joel Gaspin, Tom Griffin, Carl Peletski, Len Lipton and Bryan Baudler, (June 1998)
Source signature measurements of underwater explosives at very high ambient pressures
J. Acoust. Soc. Am., Vol. **103** (6), p 825-828.

Colosi, John A.; Edward K. Scheer, Stanley M. Flatte, Bruce D. Cornuelle, Matthew A. Dzieciuch, Walter H. Munk, Peter F. Worcester, Bruce M. Howe, James A. Mercer, Robert C. Spindel, Kurt Metzger, Theodore G. Birdsall and Arthur B. Baggeroer, (June 1999)
Comparison of measured and predicted acoustic fluctuations for a 3250-km propagation experiment in the eastern North Pacific Ocean
J. Acoust. Soc. Am., Vol. **105** (6), p 3202-3218

Comprehensive Nuclear Test Ban Treaty - Hydro-acoustic Monitoring Research
http://www.ctbt.rnd.doe.gov/ctbt/

Curtis, Keith and Bruce Howe, (March 1995)
ATOC Ambient Noise Measurements
ATOC Occasional Notes Number 28

Duncombe Rae, C. M., (1991)
Agulhas retroflection rings in the South Atlantic Ocean: An overview
S. Afr. J. mar. Sci. II: p. 327-344

Dushaw, Brian D., and John A. Colosi, (1998)
Ray Tracing for Ocean Acoustic Tomography
Technical Memorandum APL-UW TM 3-98
Available from Ocean Acoustics Library — http://oalib.njit.edu

Dushaw, Brian, (October 1998)
Ray Tracing Issues for ATOC.
ATOC Occasional Notes, No 37

References

Dushaw, Brian; Bruce Howe, James A. Mercer, Robert C. Spindel and Kurt Metzger, (November 1996.)
Acoustic receptions at SOSUS arrays "k" and "l" of transmissions from Pioneer Seamount and Pacific basin acoustic thermometry
ATOC Occasional Notes, N0. 35

Ewing, M. and J. L. Worzel, (October 1948)
Long-range sound transmission
Geolog. Soc. Amer. Memo. **27**, October 1948

Garzoli, Silvia; Arnold Gordon and Christopher Duncombe Rae, (July 1995)
Benguela current sources and transports
The U. S. contribution to the world ocean circulation experiment, U. S. WOCE Implementation Report No. 7

GEBCO digital atlas on CD-ROM
Website at http://biudc.nbi.ac.uk/bodc/gebco/orders.html

Goertner, Jean A. (1980)
Computer model predictions of ocean basin reverberation for large underwater explosions
in "Bottom-interacting ocean acoustics" (NATO Conference Series)
edited by William A. Kuperman and Finn B. Jensen
Press, 1980 Plenum

Grabb, Mark, and Ted Birdsall, (July 1995)
Comparison of ray and normal mode constructed acoustic waveforms
ATOC Occasional Notes No. 31

Guthrie, K. M. (September 1974)
Wave theory of SOFAR signal shape
J. Acoust. Soc. Am., Vol. **56** (3), p 827-836

References

Heaney, K. D.; W. A. Kuperman and B. E. McDonald (November 1991)
Perth-Bermuda sound propagation (1960): Adiabatic mode interpretation
J. Acoust. Soc. Am., Vol. **90** (5), p. 2586-2594

Jensen, Finn B.; William A. Kuperman, Michael B. Porter and Henrik Schmidt, (1994)
Computational Ocean Acoustics
AIP Press, New York.

Medwin, Herman, and Robert P. Spaulding (1980)
The seamount as a diffracting body
in "Bottom-interacting Ocean Acoustics" edited by William A. Kuperman and Finn B. Jensen
Plenum Press

Mitchell, Stephen K.; Nancy R. Bedford and Marvin S. Weinstein, (October 1976)
Determination of source depth from the spectra of small explosions observed at long ranges
J. Acoust. Soc. Am., Vol. **60** No 4, p 825-828.

Munk, W. H. and A. M. G. Forbes, (1989)
Global ocean warming: An acoustic measure
J. Phys. Oceanogr. **18**, p 1876-1898

Munk, W. H.; W. C. O'Reilly and J. L. Reid (1988)
Australia-Bermuda sound transmission experiment (1960) revisited
Journal of Physical Oceanography, Vol. **18**, p. 1876-1898.

Munk, Walter and Arthur Baggeroer, (October 1994)
The Heard Island papers: A contribution to global acoustics
J. Acoust. Soc. Am., Vol. 96, No. 4, p. 2327 - 2329.)

Munk, Walter and Carl Wunsch, (1978)
Ocean acoustic tomography: a scheme for large scale monitoring
Deep Sea Research Vol. 26A, p 123-161

References

Munk, Walter H. (February 1974)
Sound channel in an exponentially stratified ocean, with application to SOFAR
J. Acoust. Soc. Am., Vol. **55** (2), p 220-226

Munk, Walter H.; Robert C. Spindel, Arthur Baggeroer, Theodore G. Birdsall, (October 1994)
The Heard Island Feasibility Test,
J. Acoust. Soc. Am., Vol. 96, No. 4, p. 2330 - 2342

Munk, Walter; Peter Worcester and Carl Wunsch (1995)
Ocean Acoustic Tomography
Cambridge University Press

Palmer D. R., T. M. Georges, J. J. Wilson, L. D. Weiner, J. A. Paisley, R. Mathiesen, R. R. Pleshek, R. R. Mabe (October 1994)
Reception at Ascension of the Heard Island Feasibility Test transmissions
J. Acoust. Soc. Am., Vol. **96** (4), p 2432-2440

Palmer, David, (March 1994)
ATOC-FACT Arrival-Time Differences
ATOC Occasional Notes Number 17

Porter, Michael, and Edward L. Reiss, (July 1984)
A numerical method for ocean-acoustic normal modes
J. Acoust. Soc. Am., Vol. **76** (1), p. 244-252

Porter, Michael B., (1994)
Matlab demonstration programs
Available from Ocean Acoustics Library –- http://oalib.njit.edu

Porter, Robert P. (January 1973)
Dispersion of axial SOFAR propagation in the western Mediterranean
J. Acoust. Soc. Am., Vol. **53** (1), p 181-191

References

Reports on Polar Research 135/94, "The expeditions ANTARKTIS X/6-9 of the Research Vessel 'POLARSTERN' in 1992/3.")

Spiesberger, John L., and Frederick D. Tappert, (January 1996)
Kaneohe acoustic thermometer further validated with rays over 3700 km and the demise of the idea of axially trapped energy
J. Acoust. Soc. Am., Vol. **99** (1), p. 173-184

Tappert, F.D., and Xin Tang, (January 1996)
Ray chaos and eigenrays
J. Acoust. Soc. Am., Vol. **99** (1), pp 185-196

Urick, Robert J., (1983)
Principles of underwater sound, 3rd edition
McGraw-Hill Book Company

Wolfson, Michael A. and John L. Spiesberger, (September 1999)
Full-wave simulation of the forward scattering of sound in a structured ocean: A comparison with observations.
J. Acoust. Soc. Am., Vol. **106** (3), p. 1293-1306

M.A. Wolfson and F. D. Tappert (January 2000)
Study of horizontal multipaths and ray chaos due to ocean mesoscale structure
J. Acoust. Soc. Am., Vol. **107** (1), p. 154-162

Worcester, Peter F.; Bruce D. Cornuelle, Matthew A. Dzieciuch, Walter H. Munk, Bruce M. Howe, James A. Mercer, Robert C. Spindel, John A. Colosi, Kurt Metzger, Theodore G. Birdsall and Arthur B. Baggeroer, (June 1998)
A test of basin-scale acoustic thermometry using a large-aperture vertical array in the eastern North Pacific Ocean
J. Acoust. Soc. Am., Vol. **105** (6), p. 3185-3201.